Synthesis and characterization of graphene and hexagonal BN crystals on Cu by chemical vapor deposition using solid precursors

固体前駆体を用いた化学気相合成法によるグラフェン及び六方晶 BN 結晶の Cu 上への合成と評価

Kamal Prasad Sharma

A thesis submitted to the Graduate School of Engineering for the award of the Doctoral Degree of Engineering

Department of Frontier Materials
Nagoya Institute of Technology
Japan

Supervisor: Prof. Dr. Masaki Tanemura

March 2018

Dedicated to my beloved Parents, brothers, teachers, friends and wife!

Declaration

I confirm that the work presented in this thesis is my own. Where I have consulted the work of others, it has been clearly stated.

Abstract

Among hundreds of layered material investigated till now, graphene (a semimetal) and hexagonal boron nitride (h-BN, an insulator) attracted significant attention due to their promising properties in a wider range of applications. Best synthesis technique is highly desirable for the synthesis of nanomaterials at least with their pristine quality performance. The synthesis of graphene and h-BN by chemical vapor deposition (CVD) has been explored as a most scalable method than other synthesis techniques. However, the issues of crystalline quality in CVD synthesized films should be addressed through the synthesis route of single crystals. In this thesis, this issue is tackled so as to control over the catalytic substrate (Cu) and precursors used.

Chapter 1 is the introduction part about the recent progress of graphene and h-BN, including their synthesis methods, unique properties and potential applications. The motivation and purpose of the thesis are also included in this chapter.

Chapter 2 discusses the materials and methods adopted for the synthesis and characterization of graphene and h-BN. Their growth mechanism in CVD process and the most popular transfer techniques are summarized. This chapter also emphasizes the CVD system and transfer process along with the detailed characterization process used in the present work.

Chapter 3 deals with the influence of the polycrystalline structure of Cu foil on anisotropic etching for as-synthesized graphene using polystyrene (PS) as a solid precursor in a low-pressure CVD system. The etching process can be an ideal reverse

phenomenon to recognize graphene growth behavior as well as opening new opportunities to control the graphene structure. Microscopic analysis showed that both the growth and post-grown etching of graphene crystals were significantly affected by the crystallographic nature of Cu grains. The hexagonal hole formation with anisotropic etching was observed to be independent of the stripes and wrinkles in the synthesized graphene. In addition, the variation in etched pattern of the graphene depending on the base Cu grain orientations was observed, attributing to the difference in nucleation and growth processes.

Chapter 4 discusses the annealing process to create an oxide layer and subsequent recrystallization of Cu foil for the growth of large graphene domains using PS as a solid precursor by the atmospheric pressure CVD technique. The electroless polished Cu foils were annealed in Ar and successively in H_2 atmosphere to obtain smoother surfaces with reduced graphene nucleation sites. The transformation of Cu grain structures at various annealing steps was confirmed, where the gas atmosphere and annealing duration had significant influence. Graphene domains with the size larger than 560 μm were obtained on the processed Cu surface. It was revealed that the oxidation and recrystallization process of Cu foil surface significantly influenced the nucleation density, which enabled the growth of larger graphene domains in the developed CVD process.

Chapter 5 explores the synthesis of morphology controlled h-BN crystals by atmospheric pressure CVD using ammonia borane (AB) as a solid precursor. The shape of crystals could be modulated from hexagonal to triangular by controlling the pyrolysis temperature and the supply rate of AB. These phenomena were attributed to a different

growth mechanism, namely, the crystal growth limited by either the edge attachment or diffusion of AB, dependent on the concentration of BN radicals in the growth region.

Chapter 6 deals with the edge controlled growth of h-BN crystals by atmospheric pressure CVD. By controlling the supply of borazine gas generated by the decomposition of AB, the edge controlled growth of an h-BN single crystal larger than 25 μm in edge length was achieved on as-purchased Cu foils. It was also demonstrated that the variation in temperature during the growth and cooling processes induced the formation of wrinkles larger than 20 nm due to the thermal straining of the Cu surface and a negative expansion coefficient of h-BN.

Chapter 7 summarizes this work and explores future prospects.

Acknowledgement

There are numerous people I would like to thank for their input and support throughout this Ph. D. Though the words are not enough to express my feelings resided in core level of the heart, I want to convey gratitude to them all with my humble acknowledgment.

First and foremost, I would like to offer my sincerest appreciation to my supervisor, Professor Masaki Tanemura, for his patient guidance, advice, persistent support, and supervision throughout my studies. Prof. Tanemura not only provided me a platform to flourish my enthusiasm for nanotechnology but also eagerly transformed his scientific vision and nurtured me to grow as a responsible and dedicated researcher.

I am massively indebted to Associate Professor Golap Kalita for the spark of research carried out during last three years, with flawless guidance and hand in hand supports to write the manuscript drafts and their publications.

I would also like to thank Professor Tetsuo Soga for his valuable time in reviewing my thesis. His comments and suggestions were the main sources for the essential correction with improvement in this form.

Sincere thanks to Dr. Subash Sharma being a mentor to initial CVD experiments and material characterization procedures, Dr. Zurita Zulkifili for making me familiar with XRD, RF sputter and ion-beam machines, Dr. Mohamad Saufi Bin Rosmi for TEM training and Dr. Munisamy Subramanian for fruitful comments on my thesis. I would especially like to thank my colleagues Dr. Mohd Zamri Mohd Yusop, Dr. Yazid Yaakob, Dr. Sachin Maruti Shinde, Dr. Amutha Thangaraja, Dr. Ritesh Vishwakarma, Dr. Remi Papon, Mrs. Mona Araby Ibrahim, Mr. Rakesh Dayaram Mahyavanshi, Mr. Balaram Paudel Jaishi, and Mrs. Aliza Khaniya Sharma for their kind cooperation and

valuable encouragement. I would especially like to thank Mr. Sugiura, Mr. Watanabe, Mr. Ogawa, Mr. Ogura, Mr. Matsuno and all the lab-mates for their appreciable assistance.

I acknowledge my indebtedness to Hirose International Scholarship Foundation for providing me the scholarship. Academic tours and meeting organized by the foundation were the unforgettable moments at which I could accustom myself with Japanese cultures and believes.

I am eternally grateful to my Father Daya Raj Sharma, Mother Devi Kumari Sharma, brothers Binod K. Timilsana and Hari P. Sharma for making me believe in myself with constant love and support.

Last but not the least, I appreciate the support and patience of my wife Aliza K. Sharma. Your love and care withstand me in every difficult situation.

Table of Contents

Chapter 1

Introduction

1.0 Background

The era of solid state electronics started few decades ago when Bell scientist John Bardeen and Walter Barttain, realized the world first successful solid state amplifier – a transistor. The vacuum tube triodes preceded the transistor nearly 50 years and by utilizing them early computers were made. However greater number of such triodes, space occupied and power consumed by them forced scientist to think about the electron controlling technique in solid material such as metal and semiconductor rather than electrons in vacuum. Based on the foundation of vacuum tubes, Bardeen and Barttain were succeeded to understand the nature of electrons at the interface of metal and semiconductor, hence the transistor was discovered. The spark that ignited by the transistor spread towards wide research in the field of electronics and hence for more than 30 years by the concept of integrated circuits, the number of transistors per unit area doubling every 1.5 years [1]. For the last five decades, Si based chips production companies maintained the pace of Moore's law prediction. In a recent Intel chip generation, the size of transistor shrunk down to 10 nm with 100.8 millions transistors per square mm. The transistor scaling up process very soon going to approach its limits as further reducing the size, the quantum tunneling starts and the heat generated in nano

circuits and their thermal noise becomes uncontrollable. In order to keep boosting the demands of future technology a wide range applicable novel materials is highly desirable in nano electronics.

Carbon based nanomaterials anticipated as a sought materials for the future electronics as tremendous research carried out after the discovery of hollow carbon sphere named C_{60} buckyballs or fullerene (0D) in 1985 [2, 3] and one dimensional (1D) carbon nanotubes (CNTs) in 1991 [4, 5]. However, two-dimensional (2D) counter part, graphene was theoretically studied and urged by Peierls and Landau in 1930's that thermodynamically unstable and could not exist in nature [6, 7]. Arthur C. Clarke, science fiction writer quotes, "Anything that is theoretically possible will be achieved in practice, no matter what the technical difficulties are, if it is desired greatly enough"[8] to emphasize the efforts essential for practical achievement.

In 1901, Charles F. Mott attempted to control carrier concentration to study the electric field effect as a Ph. D. project supervised by J. J. Thomson [9], who discovered electron by utilizing vacuum tube. Almost century later, Andre Geim, realized the essentiality of single atomic layered metal rather than the metal used by Mott to achieve at least 10 times higher induced carrier concentration than 10^{14} for field effect property on metal [10, 11]. This idea was the turning point at which the theoretically impossible work head on towards astonishing direction, and hence graphene for the first time found to be thermodynamically stable in ambient condition [12]. The discovery of graphene in 2004 led by the simple adhesive tape pilling technique from pyrolytic graphitic sheet not only solve the issue of field effect property in metal but open up the door for more than hundred of 2D materials with various electronic properties [12, 13]. Graphene, hexagonal boron nitride (h-BN), and transition metal dichalcogenides (MoS_2, WS_2,

$MoSe_2$ WSe_2) realized as a conductor, insulator and semiconductors, respectively [14-17]. Stacking of different 2D materials among them selves as well as with other in different fashion offers variety of electronic property according to engineering skill of an individual and useful for wider application as future materials [18].

1.1 Graphene

The word graphene is derived from the word graphite and the suffix -ene is used for polycyclic aromatic hydrocarbons like (naphthalene, anthracene, coronene, benzene, etc.), and graphite for the stacked layers of graphene [19]. Hence, a single carbon layer of the three dimensional (3D) graphitic structure, that is graphene can be considered co-

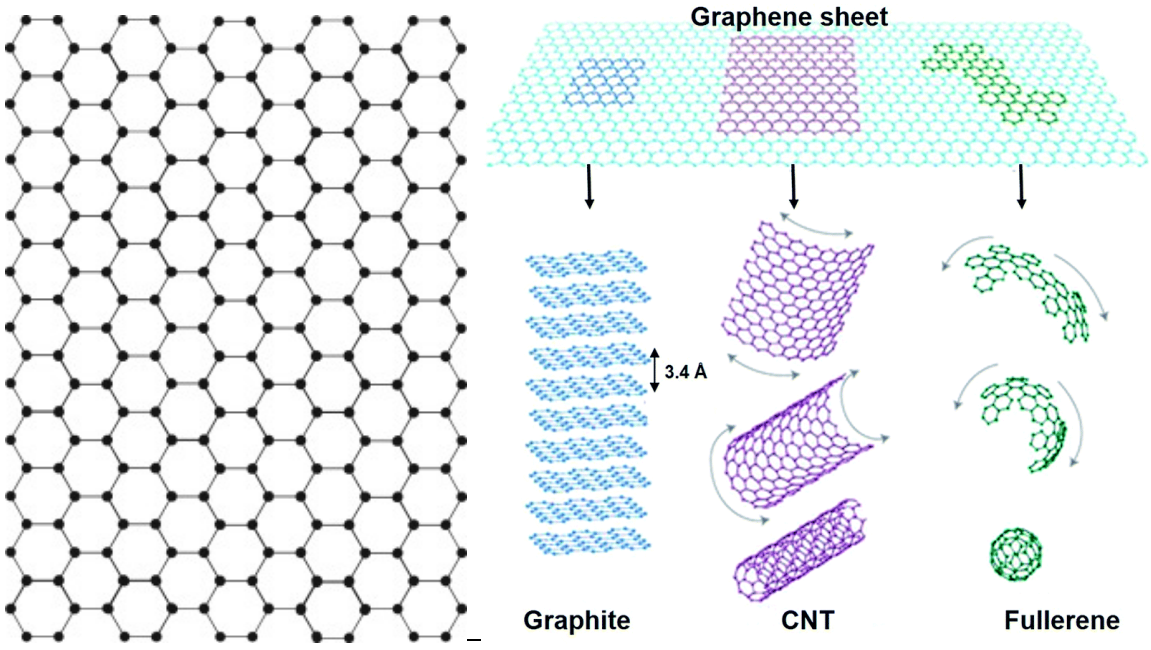

Figure 1.1. (a) Graphene honeycomb structure. (b) Graphene as a 2D building material of all other dimensions. It can be staked up into 3D graphite, rolled up in a plane into 1D nanotubes, wrapped up into 0D fullerene [21].

nstituent material of carbon allotropes fullerenes (0D), carbon nanotubes (1D) and graphite (3D) [20]. Typically, 2D graphene rolled up in a plane into 1D, wrapped up into 0D and staked up into 3D structures as shown in **Figure 1.1 (b)**, and hence considered as a mother of all graphitic forms [21].

Graphene is a 2D crystal with a honeycomb structure of sp^2 hybridized C atoms [**Figure 1.1 (a)**]. For sp^2 hybridization, four valance electrons of C atom in 2s and 2p states excited together in the presence of an external perturbation (another atom) and one s-orbital and three p-orbitals (p_x, p_y, p_z) being formed. One s-orbital and two p-orbitals contribute for the sp^2 hybridization resulting in planer assembly of graphene honeycomb structure with characteristic angle of 120^o between the hybridized orbitals (covalent σ-bonds). The remaining p-orbital perpendicular to hybridized network contributes for the week van der Waals interaction between graphene layers with so formed π-bond [**Figure 1.2 (b)**] [22]. In 1947, P. R. Wallace used graphene as a simple theoretical model for the description of 3D material and studied the band structure of graphite [23]. As the interlayer distance between graphite layer is 3.37Å [**Figure 1.1 (b)**], which is very high in comparison with 1.42Å [**Figure 1.2 (a)**], the distance between carbon atoms within the same plane [23, 24]. Wallace successfully identified graphene as a zero band gap semiconductor (semi-metal) and with extraordinarily high mean free path within graphene sheet [22, 25]. The linear energy distribution around the Dirac point [**Figure 1.2 (c)**] due to 2D honeycomb structure of graphene (lattice constant 2.46Å) makes this material different than other semiconductor in property and hence paves the avenues range of application [21, 26].

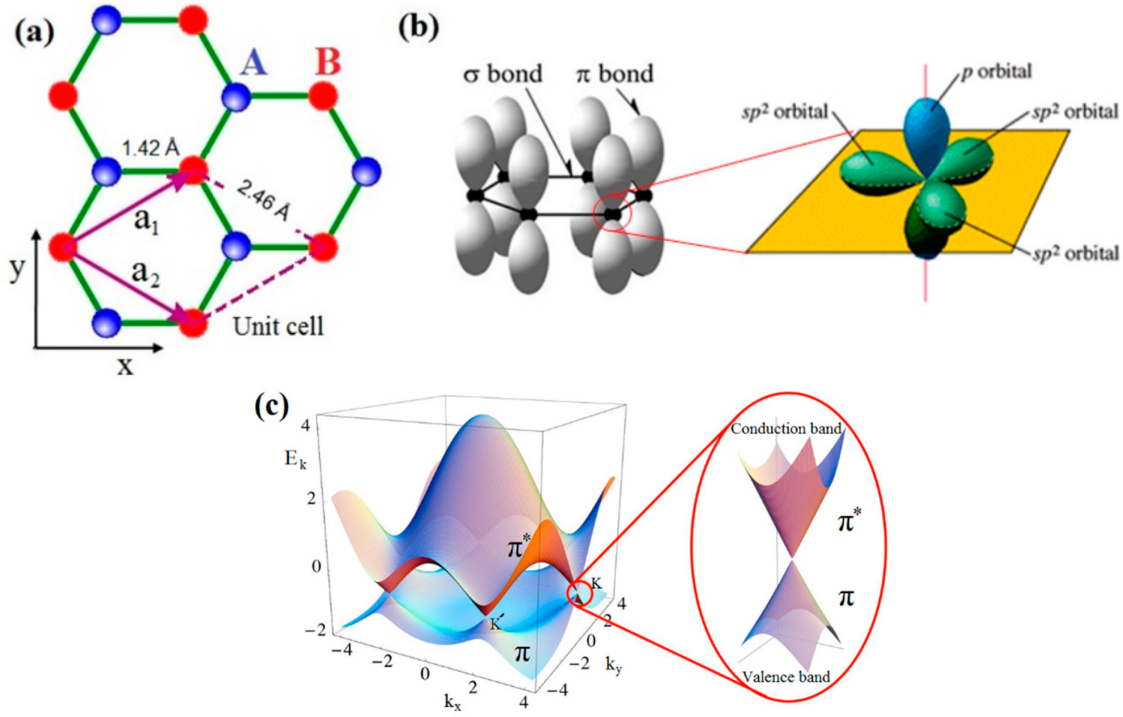

Figure 1.2. (a) Bravais lattice of graphene with lattice constant 2.46Å. (b) π-bond σ-bonds configuration in a honeycomb. (c) Electronic dispersion in honeycomb lattice with zoom in of energy band close to Dirac point [22].

1.1.1 Properties

The un-hybridized p orbital (p_z) comprised with only one electron to form π-bond and hence such a highly delocalized electron contributes for the tremendous conductivity in graphene. The zero band gap in graphene ensures that it is mass less Dirac fermions [17] and gives rise to unrivalled carrier mobility for the electrical conduction [27]. Specifically the reported mobility of suspended graphene is more than 200,000cm^2/V.s [28, 29] and strongly depends upon the temperature and carrier concentration. By applying the gate voltage to the graphene, the conductivity σ is found to be linear with the gate voltage V_g both for holes and electrons as shown in **Figure 1.3**

(a) [26]. For the ultra high mobility, the extrinsic disorder is eliminated due to electron phonon interaction at room temperature is very weak [30]. Additional to, the ballistic conduction, graphene also exhibits chiral quantum hall effect at room temperature [31, 32], an ambipolar electric field effect as shown in **Figure 1.3 (b)** with charge carriers concentration up to 10^{13} cm^{-2} continuously tuned between electrons to holes [12], and other interesting behavior like the breakdown of adiabatic Born-Oppenheimer approximation [33, 34], Casmir effects [35], Klein tunneling effect [36] and so on.

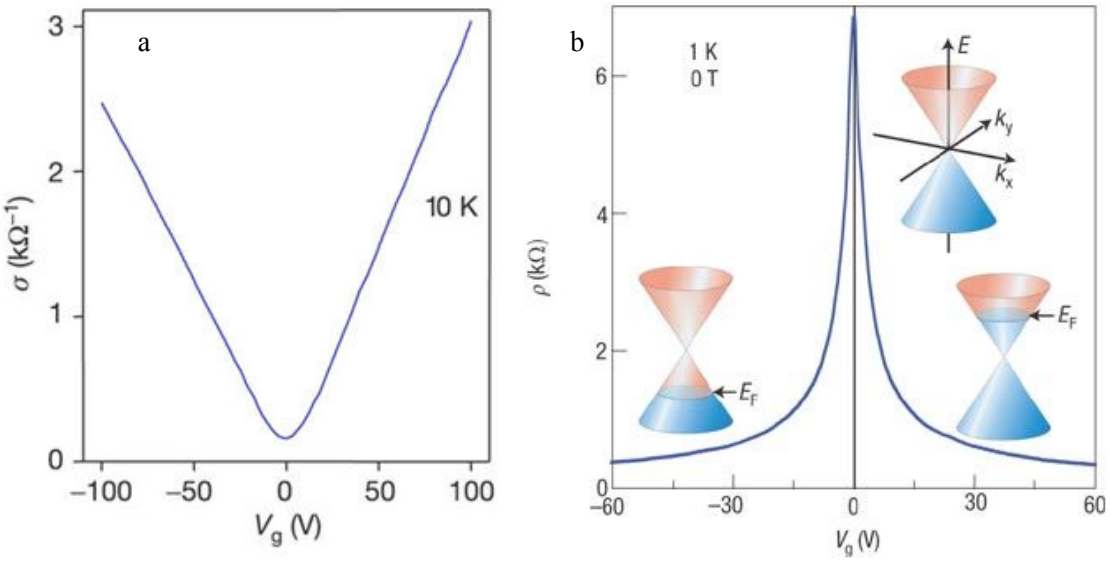

Figure 1.3. (a) Graphene conductivity as a function of gate voltage V_g at 10K [26] and (b) ambipolar electric field effect in single layer graphene with insets showing shifted Fermi energy (E_F) in conical energy spectrum of graphene with applied gate voltage V_g [21].

The thermal conductance of graphene is isotropic and conductivity is even higher than copper [37]. Experimentally calculated thermal conductivity of graphene is

in the range of 3000-5000 W/m.K and is strongly depends on the flake size and width of graphene sheet (the larger segment, more heat it could transfer) [38, 39].

Graphene has unexpected optical transparency, even atomic thick material absorbs $\pi\alpha \approx 2.3\%$ of visible light (where α is the fine structure constant close to 1/137) independent to frequency [40]. Each additional layer of graphene absorbs more 2.3% visible light and hence optical absorption of graphene found to be increase linearly with increasing number of layers (See **Figure 1.4**).

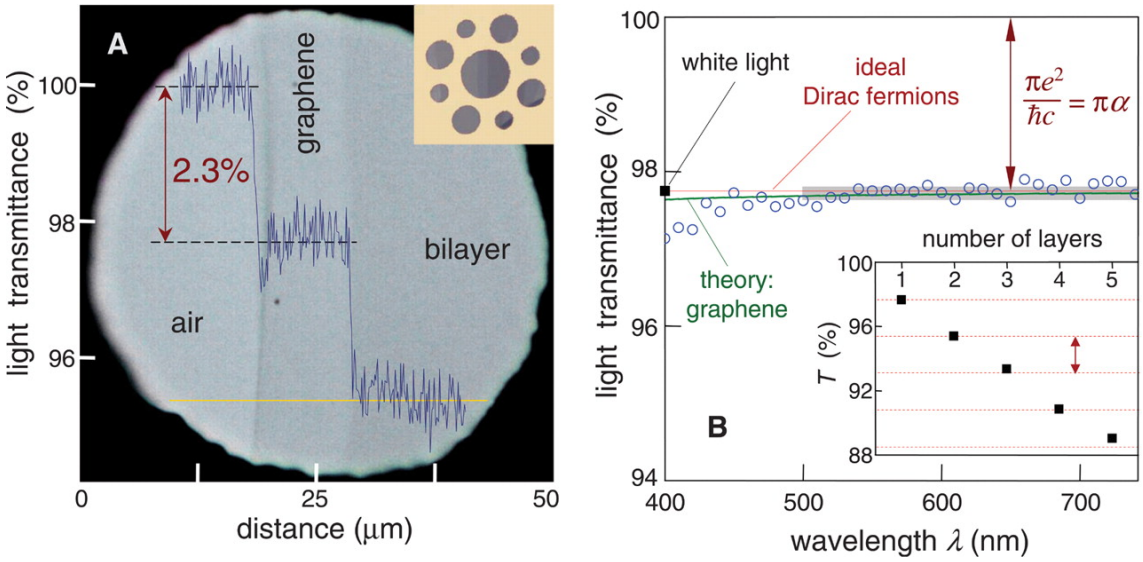

Figure 1.4. One atom thick graphene crystal in ambient condition with scan profile shows the intensity of visible light transmitted along yellow line (left side) and transmittance spectrum of single layer graphene (open blue circle) with inset of transmittance of visible light as a function of number of layers (right side) [40].

The most fascinating property that makes graphene unique material is its extreme strength [41]. Lee et al. reported the elastic property of graphene and

demonstrated the tensile strength and fracture strength of 1 TPa and 130 GPa respectively, which are higher than the reported values for other strong materials [42]. The covalent bonds that bind carbon atoms in a plane are extremely strong, possessing energy of 7.4 eV per atom. Which is much higher than the energy between graphene layers or carbon-metal with roughly 100 meV per atom. Graphene is one of the hardest: 10 times harder than diamond and strongest: 300 times stronger than steel known materials [42].

Graphene possesses chemical inertness [43] due to its strong sp^2 hybridized honeycomb structure and comprise of single carbon atoms. Monolayer graphene is even impermeable to almost all other gases, including helium [44].

1.1.2 Application

The aforementioned hugely interesting and diverse properties exhibited by graphene open up its application in areas spanning throughout all disciplines of science. The remarkable charge carrier mobility of graphene at room temperature over silicon or III-V semiconducting materials [12, 45] approved it as a future successor of those materials in nanometer sized electronics [46] The charge carriers with few nanometers of mean free path [12, 47] can travel thousands of interatomic distances in graphene lattice without scattering. Graphene based field-effect transistors (FET) specially focusing on analogue and radio frequency (RF) application has been reported as a future high performance devices [48, 49].

The superb thermal conductivity of graphene is beneficial for the use of graphene as thermal management material in the field of optoelectronics, photonics and

bioengineering [39]. Graphene is advantageous to the nano devices and interconnects which offers a heat sinking and low temperature rise during device operation. Furthermore due to higher in plane and low out plane thermal conduction in graphene, highly tunable thermal conductivity achievable on graphene composite and 3D architectures of graphene and CNT [50].

Surprisingly higher transparency and conductivity have made graphene a suitable material for transparent conductive electrodes [51-54]. Not the least, graphene utility further extends to transparent conductors, photovoltaic devices, light emitting devices, photo detectors, touch panels, ultrafast lasers and terahertz devices [55]. Furthermore, Bae et al. demonstrated graphene-based strain sensors integrated into epoxy gloves, able to read out the bending of the fingers [56] This paves the way for new applications in human interface technology by utilizing the high mechanical flexibility combined with optical transparency of graphene.

The most exciting and potential application of graphene is a cheapest alternative material for the rare and expensive indium tin oxide (ITO), widely used in liquid crystal display (LCD), flat panels displays and micro displays [57, 58]. The beauty added with transparency, conductivity and flexibility in graphene further enabled those displays with flexible outlook over the restriction of brittle ITO [**Figure 1.5**] [59]. The outstanding mechanical property along with high aspect ratio and low density of graphene is useful in the field of composite materials and enhancement of mechanical property of other materials [60-63]. Graphene can be used as an anode (graphene oxide) and cathode (reduced graphene sheet) material for Li-ion batteries due to lower specific capacity than commercial graphite [64]. Electrochemical capacitors (super capacitors or ultra capacitors) can be charged and discharged within a second due to unique

combination of high surface area and excellent electric conductivity of graphene [64-66].

Figure 1.5. Photograph of mobile with graphene in comparison with ITO as a touch screen phone (left), showing excellent flexibility of panel used [58] (middle figure), and Possible application in in bendable or foldable mobile device (right) [59].

Impermeability of graphene along with high surface area and excellent electrical conductivity makes graphene as a promising material for anticorrosion application [67]. Briefly, Impermeability of pristine graphene behaves as an excellent barrier to water, oxygen, and other corrosive materials. Graphene coating makes permitting of water more tortuous. Functionalized graphene if used as a protective coating then due to excellent electrical conductivity of graphene, an alternative path for the electrons generated on the surface provides so that they never reach to the cathodic site [68]. Nevertheless, graphene can be use in biomolecular analysis (an attempt of DNA sequencing with graphene pores [69]), biomedical application (proposed for artificial skin and orthopaedic implants [70]) and space exploration (meet some critical need for the aerospace arena [71]).

1.1.3 Synthesis Technique

Table 1.1. Summery of graphene synthesis technique with their specific features.

Technique	Brief Description	Product details	Advantage	Disadvantage
Micro Mechanical exfoliation	Graphene layers exfoliate by using sticky tape	Mono to few layered flakes size: (μm-cm)	Best for Fundamental research, High quality, simple and cheap.	Varied number of layers, small scale production, inconsistent
Liquid phase exfoliation (LPE)	Specialized solvent is utilized for the exfoliation of graphite by ultra sonication	Mono to few layer graphene flakes dispersed in liquid Size: up to μm	Easy and time efficient method, cheap and scalable, produced highly concentrated graphene oxide suspension	Uncontrollable size and layer number, significant defects, extraction from liquid essential
Reduction of graphene oxide (GO)	Chemically reduced the GO exfoliated solvent into graphene	Mono to few layer graphene suspension Size: up to μm	Versatile technique for large area production, can be stored in water	Hazardous chemical involved, only final product is stable in hydrophilic polymers
Thermal decomposition of SiC	High tempera-ture employed to evaporate Si form SiC wafer	Mono to few layer graphene films Size: up to cm	Epitaxial growth, low number of defects, control in thickness of film	Small scale producing, expensive, unscalable
Chemical vapor Deposition	Gaseous carbon source dehydrogenated into graphene on the metal surface at high temperature	Mono, bi and few layer graphene Size: cm to m	Scalable method, wide range of metals utilized as a substrate, large area up to few inch uniform film, various technique approaching monolayer film	Effort essential for the control of nucleation, High temperature, energy and time inefficient,

Most of the above mentioned characteristics and application explored for the graphene are based on the mechanically exfoliated few micron-sized samples from HOPG. Graphene samples were directly achieved form graphite and hence are very high

quality. However, those samples are limited to few microns in size [71] and even with the expertise level, to control the flake size and layer number is very difficult. In order to make graphene more reliable in all means, further investigation is highly desirable. The table 1.1 briefly summarizes mainstream synthesis technique practiced since the discovery of graphene in 2004.

Micromechanical exfoliation technique has been used for decades and prior to the discovery of graphene Lu et al. suggested that, "more extensive rubbing of the graphite surface against other flat surfaces might be a way to get multiple or even single atomic layers of graphite plates" [72]. Since the discovery of graphene [12], potentially utilized as an ideal technique for the principle investigation of graphene and new device concept. This technique is now optimized to yield high quality layers, with size limited by the single crystal grains in the starting graphite, of the order of millimeters [71]. The original idea of this technique is to apply sufficient mechanical force by using adhesive tape and overcome the van der Waals interaction existed between the interlayers of bulk material (graphite) without altering the in-plane covalent bonding. Multiple exfoliations are carried out from bulk graphite and then into adhesive tape itself so that few layer to monolayer graphene achieved [12]. Finally the adhesive tape pressed over desired substrate (SiO_2) leaving the graphene flakes onto substrate [**Figure 1.6 (a)**].

Graphene can also be exfoliated in liquid environments exploiting ultrasounds to extract individual layers by liquid phase exfoliation (LPE) technique [**Figure 1.6 (b)**]. The LPE process generally involves three steps: (a) wet chemical dispersion of graphite in a solvent; (b) ultra sonication induced exfoliation of bulk graphite into thin layer graphene flakes; (c) purification of graphene flakes by ultracentrifugation [73]. Liquids

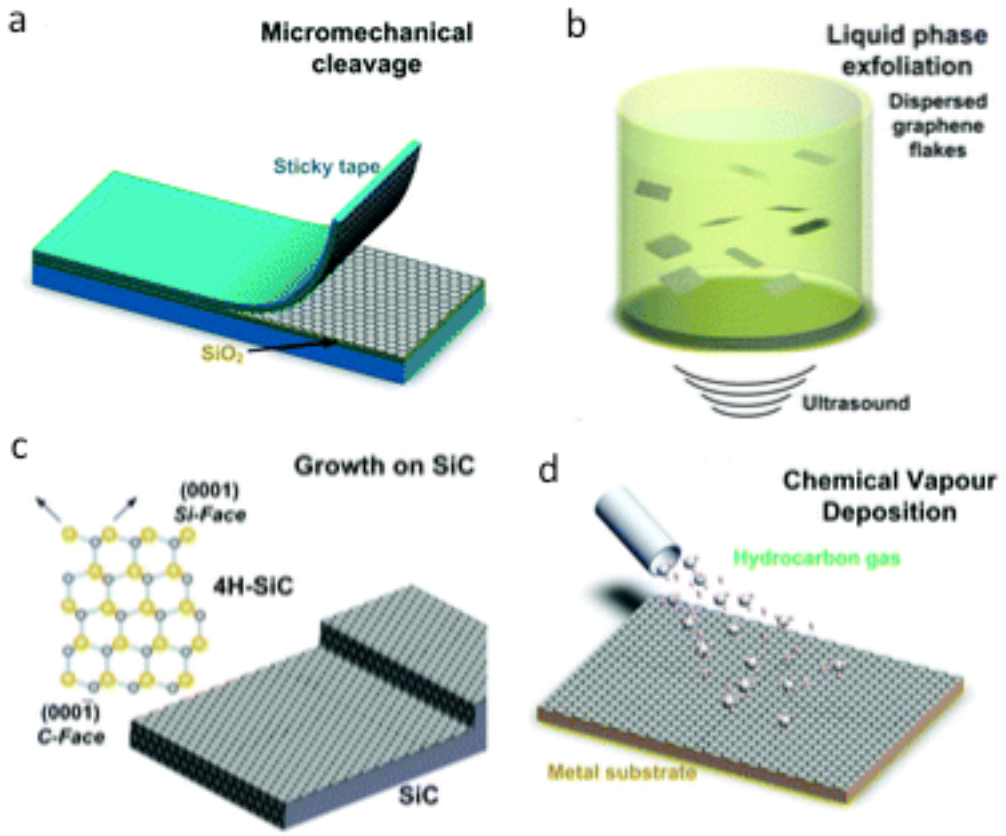

Figure 1.6. Schematic illustration of the main graphene synthesis techniques. (a) Micromechanical cleavage using a sticky tape onto SiO_2. (b) Liquid phase exfoliation showing bulk graphite dispersed into graphene flakes by ultra sonication in solvents. (c) Epitaxial growth of graphene on the surface of the crystalline SiC. Gold and grey spheres represent Si and C atoms, respectively. At elevated Temperatures, Si atoms evaporate (arrows), leaving a carbon-rich surface that forms graphene sheets. (d) Chemical vapor deposition of graphene from hydrocarbon precursors onto catalytic metal substrates [73].

including N- methyl pyrrolidone (NMP), dimethyl formamide (DMF), benzyl benzoate, γ- butyrolactone (GBL), acetone, chloroform and isopropanol, etc. [74, 75] with surface tension ~40 mN·m-1 are found to be the ideal solvents for dispersing graphene flakes to

minimize the liquid-graphene interfacial tension [73, 74]. The un-exfoliated graphitic materials can be removed from the exfoliated graphene flakes by ultracentrifugation in a uniform or density gradient medium [76]. This technique can produce monolayer graphene flakes [77] with lateral size ranging from a few nanometres to a few micrometres [78, 79]. LPE technique is scalable and cost saving and is compatible for the applications in composite materials [80], conductive inks [81], and ink-jet printing of thin film transistors [81].

Besides the exfoliation of pristine graphene, LPE technique utilized for the production of graphite oxides (GO), which is finally reduced in to graphene [73]. The most popular methods developed by Brodie [82], Staudenmaier [83] and Hummers [84] are used for the graphene production in this route. For the oxidation of Graphite, strong chemicals potassium chlorate ($KClO_3$) and fuming nitric acid (HNO_3) (Brodie's method), concentrated sulphuric acid (H_2SO_4) with successively added $KClO_3$ (Staudenmaier's method), and mixture of H_2SO_4, sodium nitrate ($NaNO_3$) and potassium permanganate ($KMnO_4$) (Hummers method) are used. These aggressive chemical processes disrupt the sp^2-bonded network and introduce different functional groups (hydroxyl or epoxide or etc.) into the basal plane and at the edge, which is essential for the GO production and subsequent liquid dispersion [73]. GO is an insulating material (R_s ~ 1012 Ω $\square^{-1}$(Ohm per square)) [85] possessed of photo luminance (PL) property [73] and is used for light emitting devices [86] and bio-imaging application [87]. However, by using a reducing agent and washing process, GO sheet can be reduced into graphene sheet [88] which further restores the electrical conductivity by healing of sp^2 network [89] as shown in **Figure 1.7**. This process is an efficient and cost effective method for the large scale graphene production. Structural

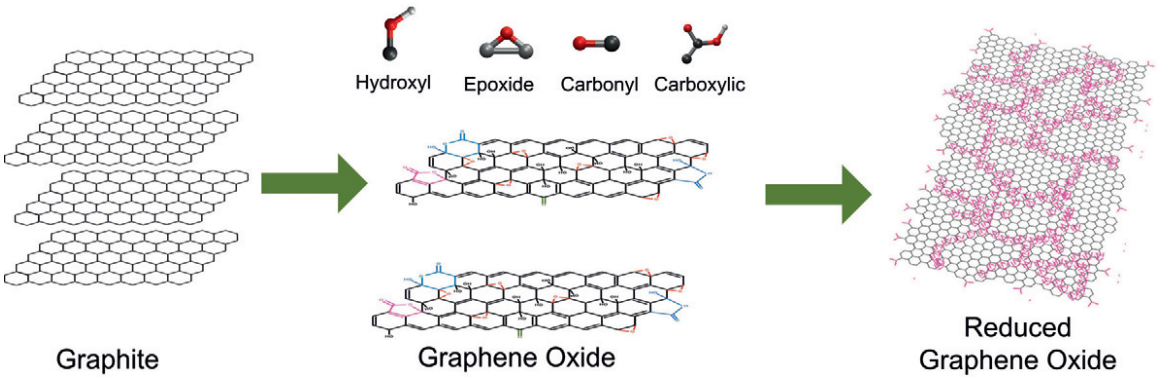

Figure 1.7. Graphite can be oxidized into GO by different procedure in the presence of strong acids, and introduced different functional groups. Partial recovery of electronic property can be reached by following a reduction treatment [73].

defects remained on the graphene sheet during reduction process [90] and hazardous chemicals used during the process should be overcome in future to make this process more beneficial.

Growth of graphene on SiC referred as an epitaxial growth and is done by annealing of SiC substrate at high temperature (>1000 ^{o}C) in ultra high vacuum [45, 91]. Despite the large (~25%) lattice mismatch between graphene (2.46 Å) and SiC (3.073 Å), epitaxial growth of graphene possible on SiC and carbon rearrange itself in hexagonal lattice as Si evaporates form the SiC substrate [91, 92] [**Figure 1.6 (c)**]. In this technique, both the C-terminated (000-1) and Si-terminated (0001) surfaces are utilized as templates [93, 94] however, the lateral size of the graphene domains formed on the C-face is almost three times than that on Si- face [95, 96]. This process produced over ~(50-100) μm to ~cm size of single to few layer graphene on Si- to C-faces [91, 97-99]. The benefit of the graphene grown by this route is that it is compatible with the

established SiC-technology in power electronics. Drawback of this technique is to control on the layer thickness homogeneity and hence prevents its potential use in applications, [73, 100], Furthermore, for the large scale production, expensive SiC wafer cost should be addressed by possible alternative means (utilizing thin SiC grown on either Si or sapphire as a substrate) [101, 102].

Chemical vapor deposition (CVD) of graphene has been demonstrated as the most promising method to grow large area, uniform graphene film with high yield and scalable in controllable approach based on industrial CNT production route. In this process, certain metals (Cu, Ni, Ir, Ru, Co, Pt, Pd, Re, etc. [53, 102-112] are utilized as a substrate for the growth of graphene through the thermal decomposition of carbonaceous source (CH_4 or liquid or solid hydrocarbons) [53, 113-118] at high temperature in the presence of other gases (Ar, H_2, mixture of Ar and H_2, N_2) as shown in **Figure 1.6 (d)**. Most of the earlier observation of graphene on metals, for example, exposing Ni to methane (1966) [119], thermal decomposition of acetylene and ethylene on Pt (100) (1965) [120], and carbon vapor exposed on Ir (1984) [121] are focused on investigation of catalytic and thermionic activity of metal surfaces [122] and hence removed so grown layers from metal [123]. Raina et al. explored CVD technique producing graphene (single- to 12-layered graphene with single and bilayer region larger than 20μm) film on Ni film with CH_4 as precursor [53]. Kim et al. further explored this technique and synthesized uniform graphene film by adopting rapid cooling approach to control over varying layer of graphene absorbed on Ni film [104]. They transferred so synthesized film onto arbitrary substrate, and showed the macroscopic use of conducting and transparent electrodes in flexible, stretchable, foldable electronics. Li et al. utilized polycrystalline Cu foil and explored the low

carbon solubility [103] and mild catalytic activity [124] in Cu are the key factor to grow dominant monolayer graphene film larger than centimeter scale [113]. Since then, CVD method scaled up for the larger area production [125-128] with uniformity in monolayer [113, 129, 130], higher crystalline [131, 132] and even producible in roll-to-roll fashion (R2R) [51, 125, 127, 128]. Nonetheless Cu catalyst based CVD method intensively explored for growth of single graphene crystals with various shapes [133-138], improved growth rate [139-144] and domain size [131,139,140] by controlling the nucleation density of polycrystalline Cu substrate. It is worth noticeable that the precursors, substrates, catalysts, temperature, and atmospheres are among the key factors in determining the final graphene products in the CVD growth [145] and are discussed in details in chapter 2. Despites the aforementioned merits, CVD technique still needed to overcome certain issues such as high operating temperature (~1000 ^{o}C), polycrystalline nature of synthesized graphene film, and safety problems rose due to flammable gases (H_2, CH_4).

1.2 Hexagonal Boron Nitride (h-BN)

Boron nitride (BN) is an III-IV group synthetic compound, attracted much attention due to commercial success and applications of wide band gap semiconductors and III- nitrides such as GaN, AlN and SiC. BN is isoelectronic and isostructural to carbon with equal composition of B and N and is produced in both amorphous and crystalline form. Hexagonal boron nitride (h-BN), sphalerite boron nitride (β-BN), and wurtzite boron nitride (ɣ-BN) are three major allotropes of crystalline BN [146]. Of particular, interest in this thesis is 2D form of h-BN.

h-BN (layered BN) is an analogous to the graphite and consisted of stacking planes of sp^2 hybridized alternating B and N atoms in honeycomb lattice with strong in plane bonding and weak van der Waals plane to plane bonding. After the discovery of 0D fullerene, 1D (nanotube) and 2D (graphene) structure of carbon, their BN counterparts have been explored [146-150]. Just after 4 years of carbon nanotube discovery, h-BN nanotubes were successfully synthesized in 1995 [147]. In 1998, Stephan and Golberg synthesized 0D octahedral BN fullerene in cage-like and rectangle-like morphologies respectively [148,149]. Most curiously, atomic layer of h-BN is investigated to be stable and exist is ambient condition [151] and free standing h-BN pilled off BN crystal by extending micromechanical cleavage technique of graphene [150]. Similar to graphene, atomic sheet of h-BN can be rolled, wrapped and staked up

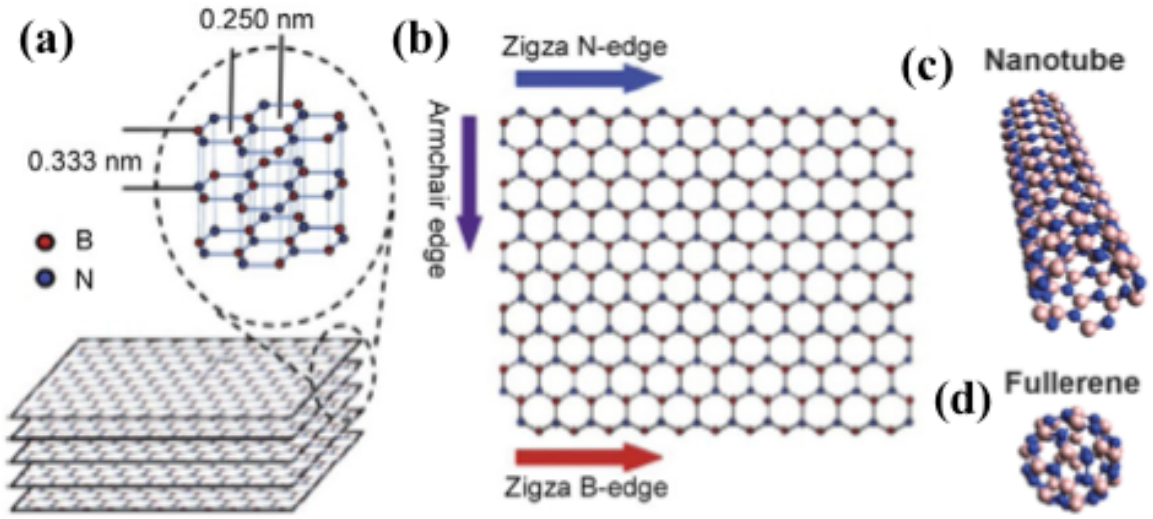

Figure 1.8. Schematic diagram showing (a) few layer h-BN, (b) single sheet of h-BN with armchair and zigzag edges [152]. (c) h-BN nano tube and (d) h-BN fullerene [146].

Despite the structural analog of graphene, B-N bonds in h-BN show a combined interaction of both ionic and covalent bonding assigned to disparity in electronegativity between B (2.04) and N (3.04) atoms unlike C-C bond [153, 154]. B-N bond in h-BN is more energetically favorable than B-B or N-N bonds as the computed energy cost increased from 5.5 eV to 7.1 eV while replacing adjacent B and N atoms [155]. Adjacent layers of h-BN are staked in AA' ways (the adjacent hexagon rings are superposed with B and N atoms alternatively located along the c axis) different from graphene' AB Bernal stacking (each layer is shifted by half a hexagon with C atoms always sitting in the centre of the hexagons). The reason for this AA' stacking in h-BN is to satisfy the electrostatic or polar-polar interactions (referred to as "lip-lip" interactions) in individual h-BN layers [156, 157]. This AA' configuration resulted in a stronger interlayer interaction and poorer exfoliation or functionalization in h-BN compared to graphene [156]. Despite the intrinsic nature of AA' stacking in h-BN, the closest neighbor layers may also slide forming AB stacking structure [157-159].

1.2.1 Properties

Bulk h-BN has been eagerly investigated for long time due to its low density, high thermal conductivity, electrical insulation, superb oxidation resistance, excellent inertness (i.e., passivity to reactions with acids, alkalis, and melts), and low friction coefficient. Based on these properties, bulky h-BN is utilized in wide range of application such as makeups (mascara, lipstick, and makeup pencils) in cosmetic industries, dry lubricant agent in spaceships and satellites, furnace and ladle linings, coatings, etc. in high-temperature refractory applications, and as a neutron detector in a laboratory scale research [160, 161]. After the discovery of h-BN most of the

aforementioned application further explored and extended for h-BN as well on the basis of following properties.

Ionic and covalent nature of in-plane B-N bonds and lip lop interaction of neighboring h-BN layer makes it a unique material. Both experimentally and theoretically investigated h-BN as a wide band gap (both direct and indirect) semiconductor with energy ranging from 3.6 to 7.1 eV [162, 163]. Watanabe et. al conclusively identified the h-BN as a direct band of 5.9 eV by using highly purified h-BN crystal [164, 165]. The optical band gap of monolayer h-BN is found to be about 6.07 eV, being consistent with the theoretical calculations (6.0 eV) [166]. The insulating h-BN (an isostructural to graphene) is atomically flat, least lattice mismatch (1.3%) with no charge impurities and dangling bonds with graphene unlike silica substrate as shown in **Figure 1.9** [167, 168]. Extraordinarily high (three order in magnitude) charge transport has exhibited while replacing SiO_2/Si by h-BN [15].

h-BN has a highly anisotropic thermal conductivity, ranging from 300 to 2000 W m-1 K-1 [169-171]. The experimental values for 11- and 5- layers h-BN were reported to be 360 W/mK (390 W/mK for bulk h-BN) and 250 W/mK respectively [172]. The reduced value in 5 layers h-BN is due to the higher polymeric residue contamination. Furthermore, theoretically it is expected that the highly improved thermal conductivity can be obtained in monolayer h-BN due to reduction in phonon–phonon scattering [173]. Thermal conductivity of h-BN is comparatively very low than graphene (see section 1.1.1 for graphene) despite their similar crystal structures, lattice constants, unit cell masses, and phonon dispersions. The softer phonon mode of h-BN and mass difference between B and N may case for this observed disparity [169].

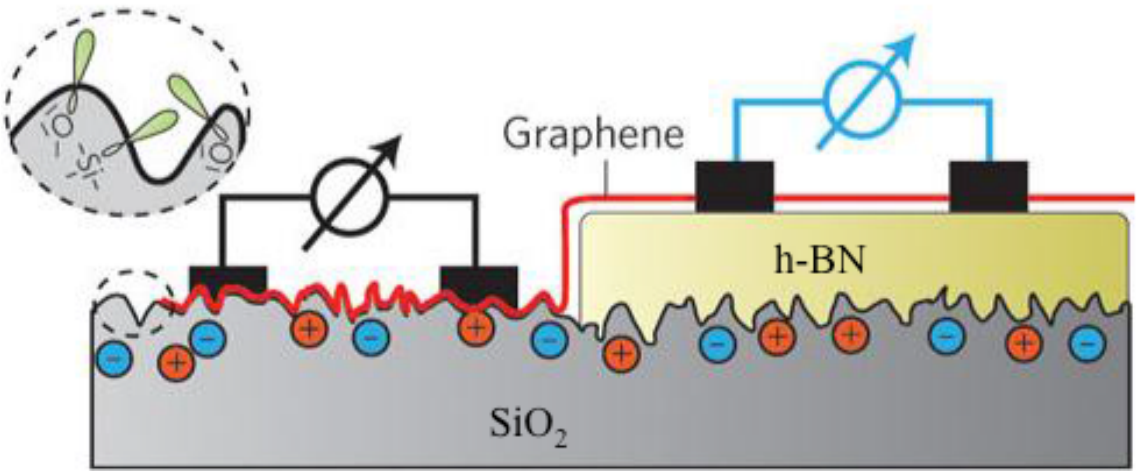

Figure 1.9. Schematic diagram showing a graphene sheet (red) supported by SiO_2 substrate (left) and by multilayer h-BN (right). The corrugations, dangling bonds (inside dashedcircle), and charge inhomogeneities that are inherent to SiO_2 surfaces are absent in h-BN [167].

h-BN exhibit a sharp absorption peak in the deep ultraviolet range (200–220 nm) however a high transparency of 99% with wavelengths in the range of 250–900 nm, because of hardly any optical absorption [174,175].

Experimental nano indentation technique (AFM probe induced) reveled the elastic modulus of 1-2 nm thick h-BN lies in the range of 184 to 510 N/m, which is in good agreement to theoretical value [174, 176]. This observed value is comparable to steel but very less than that for graphene. Theoretically, it is further investigated that the impurities and dislocations in h-BN result in lowering of mechanical strength. The mechanical strength further calculated by bending approach of h-BN (thicknesses of 25–300 nm and lateral sizes of 1.2–3 mm). The bending modulus of the h-BN increases

with the decrease in sheet thickness and approaches the theoretical value of h-BN single crystals in the sheets of less than 50 nm thickness [177]. Recently, Kong et al. also showed an elastic modulus of 18 000 N/m for multilayer h-BN measured by the AFM nano indentation technique [178], which corresponds to a Young's modulus of as large as 1.16±0.1 TPa.

Alike bulk h-BN, both few-layered and monolayer h-BN has been found to be oxidation resistant up to 850 °C, and 700 °C respectively in an air atmosphere [179], far beyond the oxidation temperature of graphene. h-BN is inert to both strong acidic and strong basic solutions [180] and hence difficult to functionalize [181] unlike graphene.

The anti oxidative and chemical inertness property of h-BN makes it applicable in protective coatings as well as in gas sensing purposes [182]. The inert nature and lack of dangling bonds in h-BN makes it as an excellent antifriction coating material [183].

1.2.2 Application

The aforementioned properties in section 1.2.1 exhibited by h-BN makes it as a promising material for wide ranges of applications, which will be discussed in this section.

Hone et al. constructed graphene-FETs with h-BN as the substrate with carrier mobility of 60000 cm^2 /V s (three times larger than that with SiO_2) [15]. On further extending this concept h-BN/graphene/h-BN-FET for radio-frequency applications also demonstrated [184]. The device performances of materials based on the conventional

substrates such as SiO_2, SiC, and Al_2O_3, where there can be coupling, scattering from charged surface states, impurities as well as the surface roughness. h-BN has been demonstrated as a dielectric layer for the fabrication of graphene-based field effect transistors (FETs) [15, 184], and explored as a tunneling barrier between graphene layers [185]. Similarly, h-BN supported flexible transistor explored which sought h-BN as a applicable materials for frontier nano-electronics [186, 187].

Being an insulator with high thermal conductivity, h-BN is reliable as a suitable alternative to conventional heat transfer materials. The application of h-BN ranges from nano filler to polymeric composite to prepare thermally conductive nano-oils [188,189] and to make highly thermally conductive composites [190,191].

The direct wide band gap as well as the UV luminescence property of h-BN makes it a promising candidate for application in ultraviolet lasing [164], photon emission [192] and DUV detectors [193].

The large elastic modulus and high strength of low-density h-BN is useful to improve the mechanical performance of polymer- or ceramic- derived composites**.** Different fraction quantity of h-BN is added with polymers poly (methylmethacrylate) (PMMA), polyvinyl acetate (PVA), and polybenzimidazole and ceramics such as polycarbonate to improve the strength of composites [190, 194, 195].

1.2.3 Synthesis technique

Boron nitride is a synthetic compound, synthesized in 1842 by the reaction of

boric oxide and potassium cyanide for the first time [196]. Nowadays, h-BN powders are synthesized in commercial scale by heating boric acid/boric oxide and an ammonia/melamine/urea mixture at 900 °C. Finally the synthesized compound is annealed at 1500 °C in N_2 atmosphere to increase the crystallinity of the powders [197, 198]. After the discovery of graphene in 2004, h-BN synthesized in all the possible ways; CVD process is most promising one, and will be discussed in this section. Besides the mainstream synthesis technique (discussed in this section), there are many h-BN synthesis approaches such as unzipping of h-BN nanotube, blender shearing, Ball milling, etc. [152, 146].

Micromechanical exfoliation technique is adopted to exfoliate high quality of h-BN atomic layers similar to the graphene as discussed earlier in section 1.1.3 [14, 150]. Pacile et al isolated h-BN using adhesive tape by repeatedly peel off BN layers from powdered h-BN until the single layer achieved [199]. By adopting this technique, an uneven h-BN flake of 10 μm had been obtained with the thinnest region of about 3.5 nm and the thickest region of roughly 80 nm. On the basis of such a exfoliated h-BN flakes, the structural arrangement, chemical nature, edge construction, and defect dynamics in the few years followed were studied. Accordingly, high temperature and pressure processed large h-BN single crystals [164,165] were employed for exfoliation, and the resultant size of the few-layer h-BN samples could be larger than 100 μm [see **Figure 2.5 (c)**][200]. Such an exfoliated samples were used to explore the wide spread properties and application of h-BN [15, 167, 179, 186, 199-203].

Han et al. accomplished liquid based exfoliation of h-BN in 2008 [204], which is in principle identical with the liquid based exfoliation of graphene; to disperse and break the van der Waals interaction between the layers, by sonication. This organic

solvent based exfoliation technique further extended by Zhi et al. [190] in surfactant solution based sonication for the large-scale fabrication of h-BN nano sheets. Coleman et al. exfoliated a number of layered materials in several common solvents without the use of diverse surfactant and organic solvents [205]. The amount of nanosheet exfoliation and retention in the solvents was found to be dependent on the solvents' surface tension (best exfoliation was seen for 40 mJ/m^2). Mixed solvent such as water and ethanol, IPA in ammonia solution has been explored as beneficial for exfoliation process [206, 207].

CVD of h-BN has been demonstrated as the most promising method to grow large area, uniform h-BN film with high yield and scalable in controllable approach, similar to graphene. CVD synthesis of h-BN can be date back to 1968 and few micron thick h-BN films synthesized on different substrates in following two decade [180, 208-211]. In 1995, single layer h-BN synthesized on Ni in ultra high vacuum reported for the first time [212]. Various substrates (Cu, Ni, Pt, Ir, Rh, Ru, Pd, Ag, Au, Fu etc.) [175, 213-229] have been explored for the h-BN synthesis by using single (borazine, ammonia borane, β-trichloroborazine, etc.) or mixed (diborane and ammonia) precursors in the presence of various gaseous (Ar, H_2, mixture of Ar and H_2, N_2) environments. Due to toxic and unstable nature of borazine in ambient condition, ammonia borane (AB) is widely used as precursor, which gives borazine on heating. Song et al. sublimed AB to grow large-scale h-BN on Cu with 2-5 layers for the first time by using APCVD [174]. Since then CVD process is intensively investigated for the growth of high crystalline h-BN film. Various approaches focused on either modification of substrate or pyrolysis technique of precursor. Polycrystalline Cu, Ni, Pt and Fe foils have been investigated for the growth of large crystals of h-BN and hence

the better quality of h-BN film [213, 215, 222, 223, 230-232]. The weak chemisorption and the polycrystalline nature of the Cu and Pt foils, triangular h-BN islands found to be grown in random orientations [213, 222, 232]. Due to polycrystalline nature of substrate and binary elements in h-BN, CVD method even sought to be challenging approach for h-BN than to graphene. Optimization of CVD parameters strongly influences the synthesized film quality. CVD parameters and undelaying mechanism of h-BN growth is discussed further in chapter 3, 5 and 6.

1.3 Motivations and Purposes of the Thesis

Over the last decade, layered materials down to the atomic level thickness and their stacking in different ways witnessed for the manipulation of grater ranges of property. Based on ones imagination and critical thinking capacity many artificial materials could be engineered in reliable ways. This is the milestone situation in nanomaterials in which both material and condensed matter scientists chase one another for discovery of novel material and their investigation for frontier application. Best synthesis technique is highly desirable for the synthesis of nanomaterials at least with their pristine quality performance. Micromechanical cleavage technique entertained for the investigation of materials performance capacity complementary to the theoretical approach.

CVD process established to be scalable way for the synthesis of various nanomaterials including graphene, h-BN and TMDCs. The moderate quality of CVD synthesized material and device performances than theoretically expected values demands detail exploration of CVD technique. Polycrystalline nature of synthesized

materials, which degrade the materials performance property, should be addressed at first. Synthesizing large single crystals could solve this issue. For the case, complete understanding of CVD component such as growth substrate and constituent materials used for the growth purpose is most essential.

In this thesis, CVD parameters are optimized for the synthesis of large domains of graphene and h-BN. For this achievement, detailed understanding of Cu catalytic role before and after the materials growth and step-wise pyrolysis of precursor molecules are found to be most important. The optimized CVD parameters are almost identical for both graphene and h-BN synthesis, which will be most significant for the single step graphene and h-BN hetero-structures synthesis.

1.4 Organization of the Thesis

The controlled CVD synthesis of graphene and h-BN crystals on Cu by using solid precursors is emphasized in detail in the following chapters.

Chapter 1 is the introduction part about the recent progress of graphene and h-BN growth. Important properties, current and future application of materials is also summarized in this chapter. Finally, motivation and purpose of the work is also included.

Chapter 2 organizes more literature review ways and brief introduction to the material and methods adopted in this thesis. However, the details of CVD mechanism and important CVD parameters are discussed. Specific transfer and synthesis process

kept in respective chapters. The characterization procedure is ideally summarized in this chapter.

Chapter 3 deals with the variation in nucleation density, orientation and size of graphene crystals grown on Cu foil owing to crystallographic orientation of Cu. Post growth etching of such graphene crystals was significantly affected by the crystallographic orientation of Cu grains.

Chapter 4 investigates the crystallographic transformation of Cu grains on annealing at different duration in H_2 atmosphere after pre-annealing in Ar atmosphere. Isolated graphene domains with size larger than 560 μm were obtained on the processed Cu substrate by using polystyrene (PS) as solid precursor.

Chapter 5 demonstrates the transformation of hexagonal shape to triangular by controlling heating temperature of AB. With a low supply of BN building blocks, crystal growth was the edge attachment limited, producing triangles, whereas, under higher concentration of BN building blocks, crystal growth was limited by diffusion producing hexagons.

Chapter 6 demonstrates the AB pyrolysis technique determining the different morphologies of triangular crystals within the range of 65 to 80^{o}C. The stepwise AB decomposition process found to be essential for the perfect h-BN crystal growth. The quantitative investigation of h-BN wrinkles is also discussed.

Chapter 7 summarizes the results to establish the concluding remarks and recommendation for future prospects.

Chapter 2

Materials and Methods

2.0 Background

This chapter will summarize the main experimental materials and methods used for the synthesis of both graphene and h-BN, together with their transfer and characterization technique employed in this thesis. This chapter is divided into three main sections: (a) details of CVD systems along with important CVD components; (b) transfer technique onto arbitrary substrates and TEM micro grids; (c) brief introduction to the instruments utilized for the characterization of synthesized materials.

2.1 Chemical Vapor Deposition (CVD)

Chemical Vapor Deposition (CVD) is a solid film synthesis technique by utilizing the gases form of precursor materials (atoms or molecules or a combination of both). Deposition occurs when the precursor is absorbed and coalesced on the substrate through the process as described in **Figure 2.1**. Briefly, the process includes: (1) forced convection of gaseous reactant and their diffusion into substrate through boundary layers form the main stream flow; (2) dissociative chemisorptions of reactant on to the substrate; (3) chemical reactions take place either by bulk absorption or surface mediated process; (4) desorption of by-products (absorbed species) form the surface; (5) transport of by-products towards main

stream flow by diffusion [233, 234].

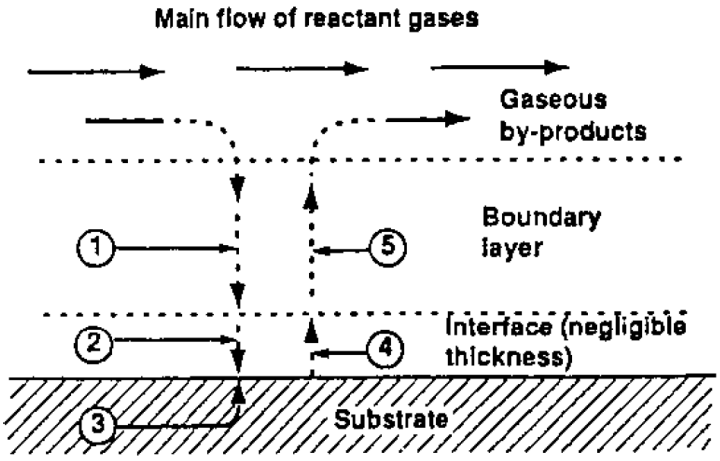

Figure 2.1. Schematic diagram showing sequences of event in CVD process [233, 234].

CVD technique is most popular for the scalable synthesis of graphene and h-BN as discussed in sections 1.1.3 and 1.2.3. Wide ranges of substrates for example Ni, Pt, Ir, Rh, Ru, Pd, Ag, Au, Fu etc. including Cu have been explored for the growth of both graphene and h-BN [53, 103-112, 175, 213-229]. Among them, Cu and Ni are most intensively studied and widely used. Graphene and h-BN reported to be strongly chemisorbed on Ni contrary to which weakly on Cu [235-239]. This is due to strong hybridization of Ni d_z^2 orbital with B-, C-, and N- p_z orbitals however; completely filled d-orbitals of Cu resulting in very less hybridization energy [235, 236]. That favors the surface migration of adatoms on Cu and minimum bulk diffusion unlike in Ni, and hence uniformly deposited graphene as shown in **Figure 2.2 (a)** [240]. It should be worth notable that, the h-BN growth process is quite complex than graphene due to different electro negativities of B and N with Cu. B found to be bulk adsorbed alike C in Ni however N follows surface migration process alike C in Cu. For perfectly balanced B and N fluxes resulted in h-BN growth on Cu surface as shown in

Figure 2.2 (b) [241]. To achieve the perfect balanced B and N fluxes for h-BN growth and to avoid the minimum possible bulk absorption of C on Cu, CVD parameters should be optimized. This thesis focused on the graphene and h-BN growth on Cu with least varying CVD parameters.

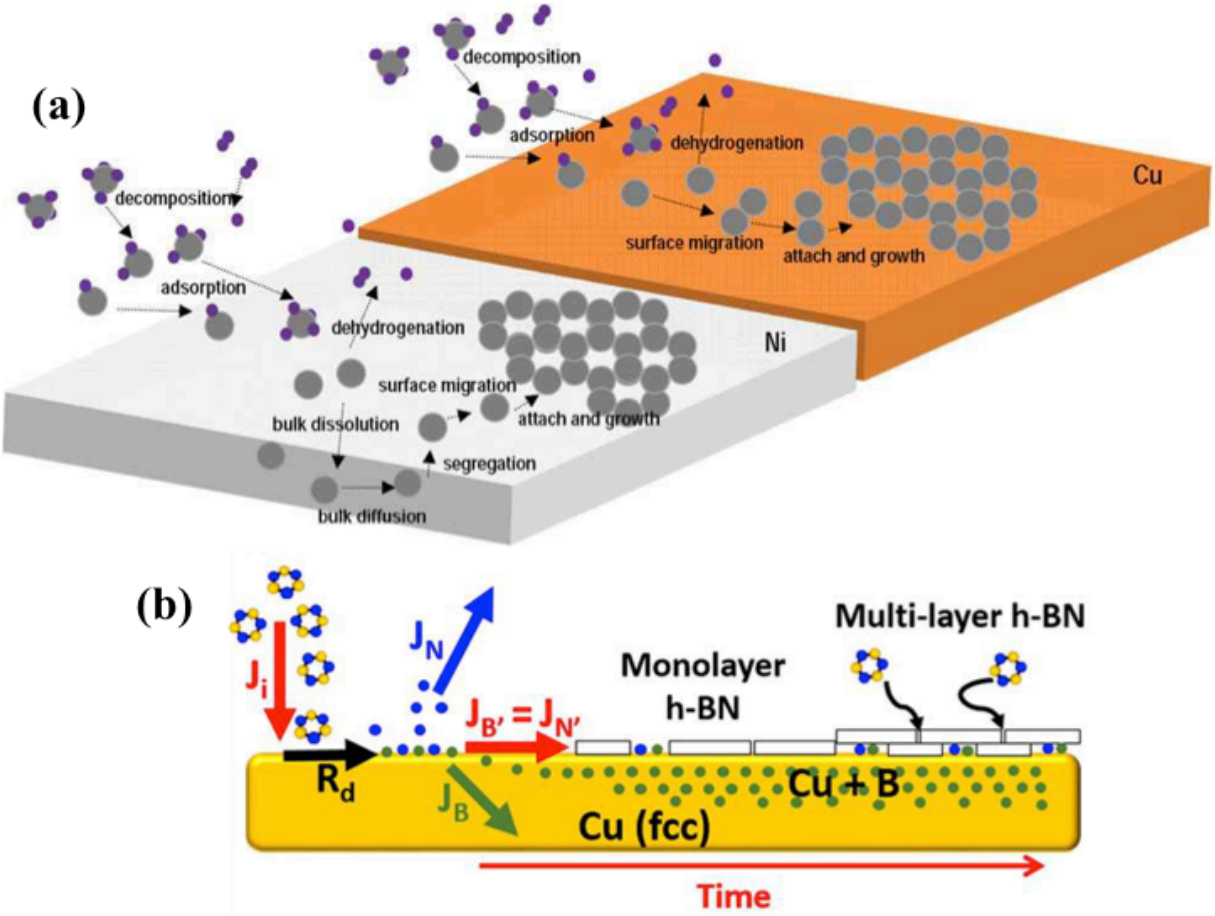

Figure 2.2. (a) Schematic diagram showing catalyst dependent growth kinetics of graphene on Cu and Ni [240]. (b) Schematic diagram showing h-BN growth process on Cu. J_i is the impingement flux of borazine, J_B is the diffusion flux of B into the Cu substrate, J_N is the diffusion flux of N out of the Cu substrate, and $J_{B'}$ and $J_{N'}$ are the flux of B and N atoms to form h-BN on Cu [241].

Methane (gas), ethanol (liquid) and solid hydrocarbons [53, 113-118] are used as a precursor for the growth of graphene. However, due to the weaker bond energy (between 292kJ/mole to 305 kJ/mole) of polystyrene (PS) in comparison to methane (410 kJ/mole) [242], PS was used as a precursor for graphene synthesis. Not the least, solid precursor PS (for detail see chapter 4) is not as expensive and flammable as methane (suitable by economic and safety purpose). AB is non-flammable and non-explosive under ambient condition. Many groups explore AB for h-BN growth. We use AB for the h-BN growth; details discussion about AB is made in chapter 5 and 6. The pyrolysis temperature and duration of both PS and AB (during growth stage of CVD) were found to be most important for the synthesis of large domains of graphene and h-BN.

Temperature and CVD atmosphere are key factors for the graphene and h-BN growth by CVD method. The ramping rate of furnace strongly influence the substrate morphology and hence the catalytic activity. In the CVD system, mostly Cu is preheated in Ar atmosphere with ramping rate of 10.5^{o}C/min from room temperature to 1050^{o}C. Cu annealed in H_2 or mixture of H_2 and Ar to improve the catalytic activity. The growth time, the ways of precursor supplying technique and gas composition during growth are primary concern of this thesis and is discussed in respective chapters. Finally, fast cooling technique was employed as soon as growth finished with identical gas composition during the growth.

Figure 2.3 shows CVD system used for the graphene and h-BN synthesis. Briefly a quartz tube of inner diameter 45 mm and length of 80 to 90 cm was used as a main reactor zone and is inserted into the double-splatted horizontal tubular furnace. Cu foil was kept inside the tube equivalent to the central part of furnace and processed through different stages of CVD (pre-heating, annealing, growth and cooling). During growth, either the heat utilized form the growth furnace (termed as single furnace CVD) or separate heating furnace was

used (termed as double furnace CVD) to supply the precursor. In single furnace CVD, temperature essential for precursor's pyrolysis was manipulated by using magnetic boat. Mass flow controllers are used for flowing specified quantity of Ar and H_2. By connecting exhaust with pump for the desired vacuum inside the chamber of atmospheric pressure CVD (APCVD) system and is utilized as Low pressure CVD (LPCVD) system. Most specific discussions are made in respective chapters.

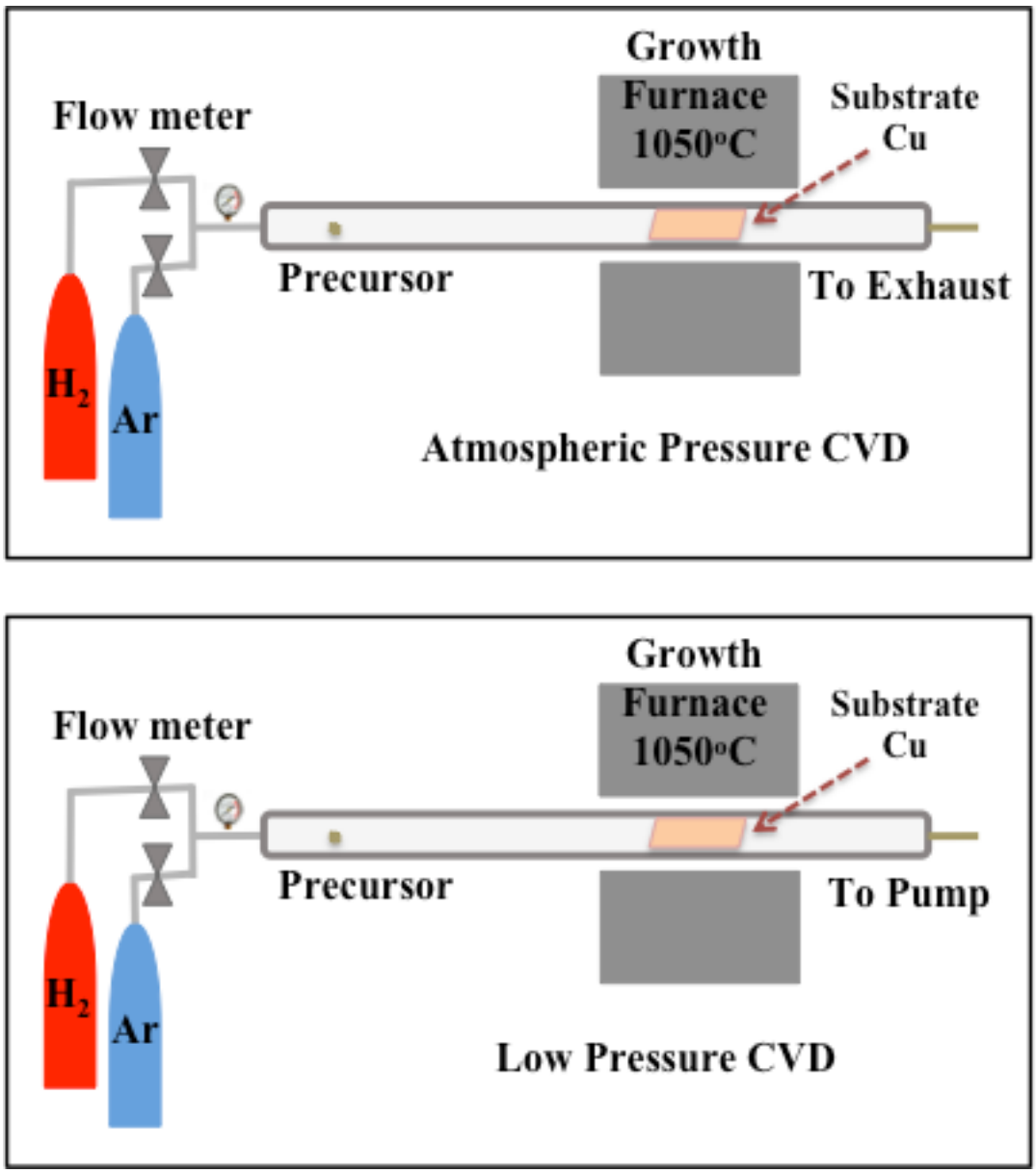

Figure 2.3. Schematic diagram of APCVD and LPCVD system.

2.2 Transfer Technique

Transfer process is most important step for the utilization of metal catalyzed CVD grown graphene and h-BN for electronics, composites, and applications as well as for their characterization. Poly(methyl methacrylate) (PMMA) assisted transfer of graphene and h-BN onto arbitrary substrate is most popular. At first, finite thickness of PMMA is deposited (PMMA solution prepared in anisole or acetone is spin coated or ordinarily drop casted) on the graphene or h-BN on the substrate (Cu). PMMA is dried for the crystallization for min prior to graphene and h-BN separation from metal either metal sacrificial [51, 54, 174, 243-249] (etching metals by strong etchant solution such as $FeCl_3$, $Fe(NO_3)_3$, ammonia per sulfate, etc.) or electrochemical delamination [110, 250, 251], (metals can be utilize for repeated growth process after transfer) technique. Finally, the deposited PMMA layer is removed form the top of graphene and h-BN after transferring onto the desired substrate [246, 243]. The complete removal of PMMA and few residuals metals particles are researched to be impossible; and degrades the electronic performance [27]. As an alternative of PMMA assisted process, iso-propyl alcohol (IPA) supportive direct transfer of graphene and h-BN onto TEM mesh is purposed [252, 253]. The details transfer process of graphene and h-BN is as summarized in **Figure 2.4.**

For the transfer process, 4.6 mg of PMMA was dissolved in 100 ml of acetone and the stock solution so prepared was deposited onto Cu substrate with graphene or h-BN (100 µl PMMA solution was spin coated with 4000rpm for 1 min in drop wisely). The dried PMMA layer along with h-BN or graphene was separated form Cu by $FeCl_3$+ HCl (Chapter 4), $Fe(NO_3)_3$ (Chapter 5) a solution etching process and electrochemical delamination process (Chapter 3 and 6). The 1N NaOH solution processed electrochemical delamination (Cu as cathode and Pt as anode) technique is found to be time efficient with fewer impurities after

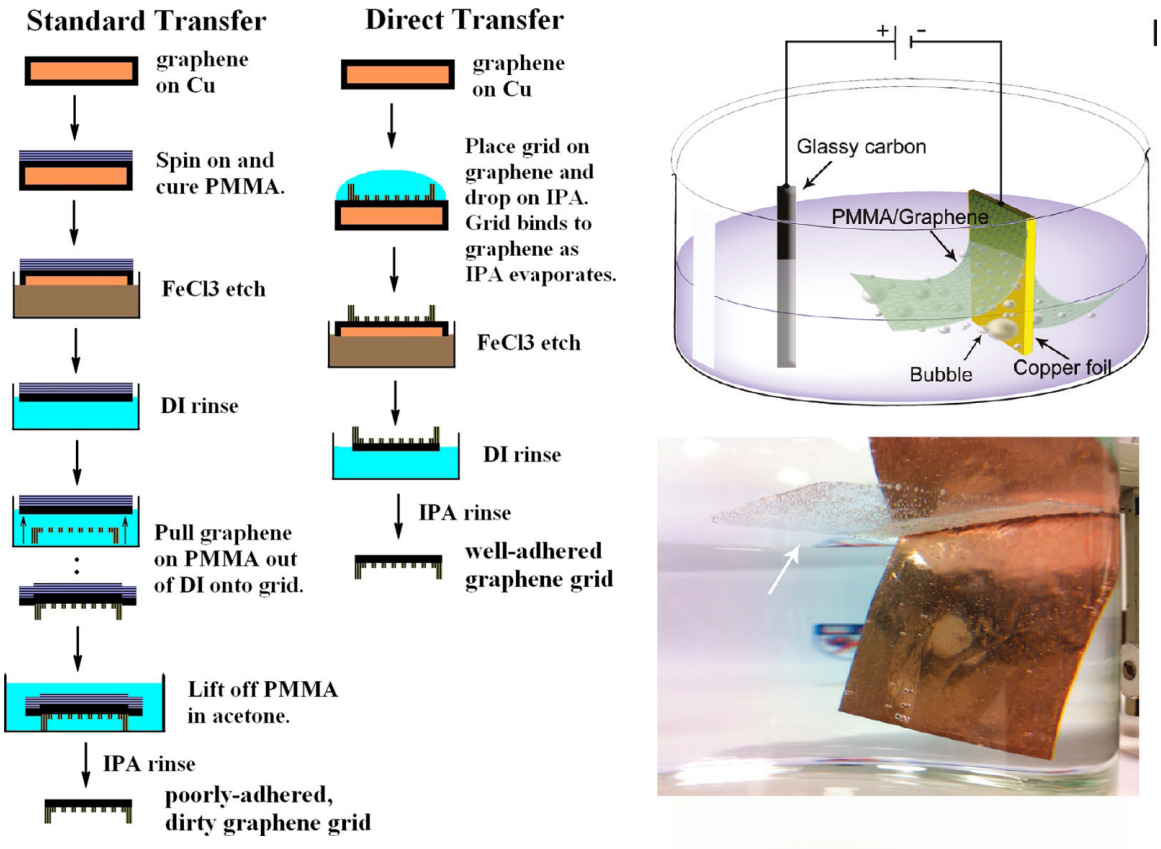

Figure 2.4. Schematics showing PMMA supportive and PMMA free transfer process onto TEM grid and identically onto other arbitrary substrate (left) [252]. Schematic showing electrochemical delamination of graphene and photograph showing pilling of PMMA and graphene from Cu (right) [251].

transfer. The scooped PMMA/graphene or PMMA/h-BN was transferred onto SiO_2/Si, quartz, PET and TEM mesh and finally PMMA was removed by hot acetone after drying for 5 min. As most of the samples consisted with h-BN and graphene crystals, intense care had been taken in different stages of transfer.

2.3 Characterization

The graphene and h-BN crystals grown on Cu by CVD method in this study were

characterized by different analytical technique based on their physical and chemical property. In this section, basic introduction to the instruments used for characterization of substrates and synthesized materials is provided along with their brief working principle.

2.3.1 Optical Microscopy

An Optical Microscope (OM) is found to be a straight-forwarded characterization tool for the identification of exfoliated graphene and h-BN transferred on to the SiO_2/Si substrate [14, 150, 183]. The optical transparency of both graphene and h-BN decrease with increasing layers numbers, resulting in distinguishable optical contrast on SiO_2/Si as shown in **Figure 2.5 (a)-(d)**. It should be noted that Si substrate with SiO_2 thickness of 300 and 90 nm gives the maximum optical contrast of 11% and 2.3% per layer respectively for graphene and h-BN for white light [200, 254]. Most convenient method was demonstrated for direct identification of graphene deposited on Cu by oxidizing the undelaying Cu across the graphene grain boundary and defects and is integrated for h-BN as well [255, 256]. The different optical interference contrasts between oxidized and un-oxidized Cu facilitated the direct identification of graphene and h-BN areas under an optical microscope as shown in **Figure 2.5 (e)**. This technique further extended for the identification of grain boundaries (GBs) by selectively damaging graphene GBs using oxygen plasma and thermally oxidizing underlying copper through the defective GBs in CVD graphene film [255, 257].

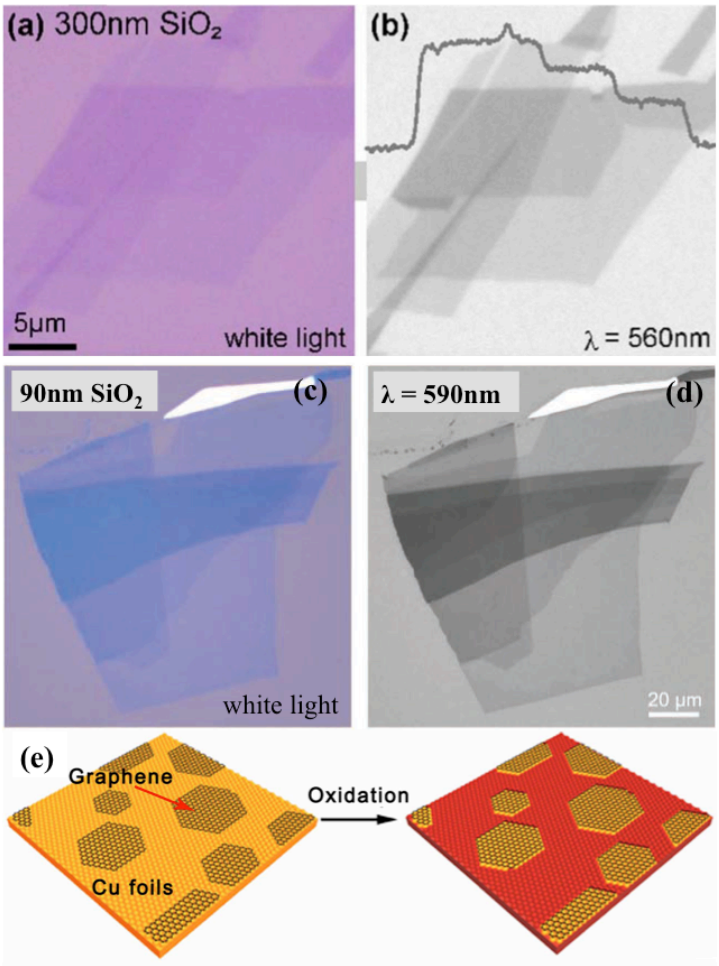

Figure 2.5. OM images of mechanically exfoliated graphene and h-BN under white light. (a) graphene on 300 nm SiO_2/Si, (b) enhanced in contrast with green filter and line overlaid showed respective thickness [254], (c) h-BN on 90 nm SiO_2/Si, (d) enhanced in contrast with green filter [200]. Bottom most right side in (a)-(d) are representing the monolayer regions of graphene and h-BN. (e) Schematics of oxidation of Cu for the identification of graphene and similar technique adopted for h-BN [255].

An OM (VHX-500) with a Moticam 2000 2.0Mpixel camera in reflectance mode has been employed to obtain the optical images presented throughout this thesis. OM is used to rapidly investigate the various samples including the surface morphologies of substrates, confirmation of grown materials, layers number identification of graphene and h-BN after transferring onto SiO_2, etc.

2.3.2 Raman Spectroscopy

Raman spectroscopy is a technique widely used to obtain structural and electronic information of sample by utilizing inelastic scattering of monochromatic light source form the sample in a vibrational mode. This technique is relatively easy, non-destructive, non-contacting, and quick to obtain the spectrum at room temperature and ambient pressure, which can be used as a fingerprint for the identification of physical property of materials. This technique is intensively used for the layer number identification and qualitative information regarding the graphene and h-BN [53, 200, 258-260]. Raman scattering spectra and mapping of graphene and h-BN presented in this thesis were obtained by using NRS-3300 Raman spectrometer with laser source of wavelength 532.8 nm at room temperature.

Three characteristics peaks are widely recognized in graphene around 1350, 1580, and 2690 cm^{-1} named as D, G and 2D peaks respectively as shown in **Figure 2.6 (a)** [258] The G peak is assigned to in-plane vibration of sp^2 carbon-carbon stitching bonds (E_{2g} phonon). Where as D peak is assigned to first-order zone boundary phonons, which strongly indicates the amount of disorder present in the graphitic materials and is absent in defect free graphene. The 2D peak arises from the inter-valley scattering of the electrons by the Brillouin zone boundary phonons, is an overtone of D peak representing the stacking order. The shift in position of individual peaks are strongly associated with the light source used for the detection of spectra as well as the layer numbers of graphene as shown in **Figure 2.6 (b)-(d)** [259]. The high intensity ratio of 2D to G peak (2D/G), a weak D peak and narrowed 2D peak width are indicators of good crystalline quality of graphene. Generally for layer identification, 2D/G ratio with 1 is for bilayer layer, more

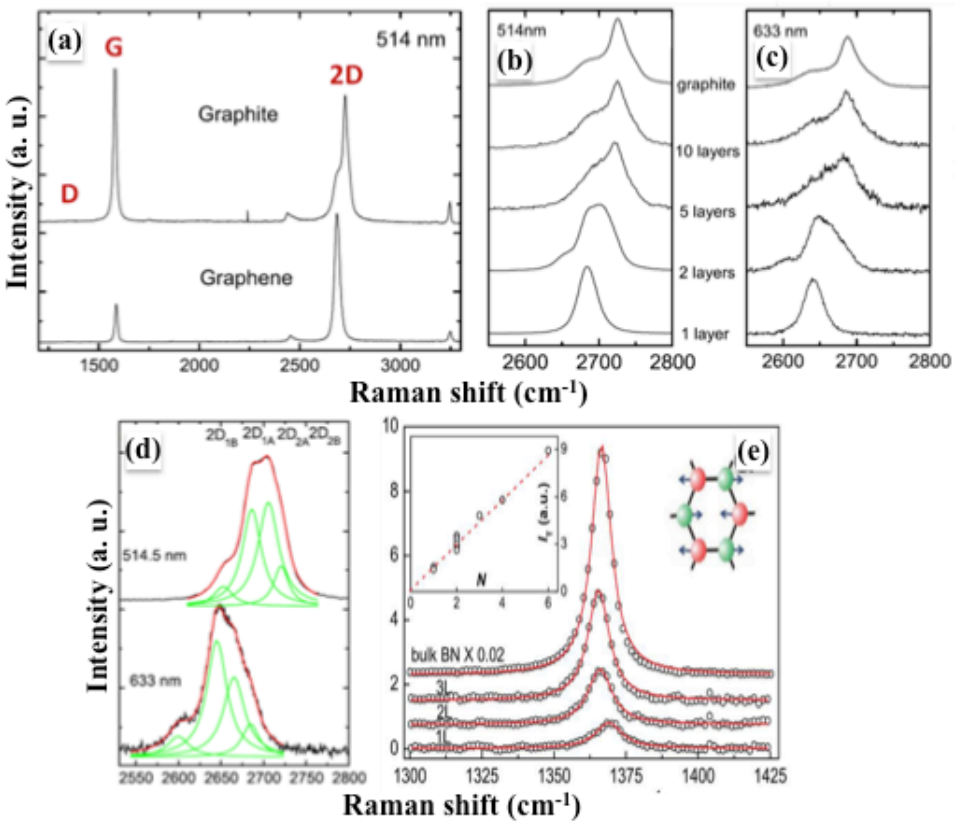

Figure 2.6. (a) Raman spectra at 514 nm comparing bulk graphite and graphene. Changes in Raman spectra with increasing number of graphene layers (b) at 514 nm and (c) 633 nm. (d) Four components of 2D peaks in bilayer graphene showing an increased band with increasing layer [259]. (e) Raman spectra of mono-, bi-, tri- layer and bulk h-BN (inset left showing the variation in integrated intensity I_T with respect to the number of layers N and inset right illustrating the phonon mode responsible for the Raman peak) [200].

than 1 for monolayer and less than 1 for multilayer graphene [53]. Similarly, broader 2D peak indicates the increasing layer number as represented by **Figure 2.6 (d)** with four different de-convoluted peaks.

Analogous to the G peak in graphene, in plane vibration of sp^2 Boron-Nitrogen stitching bond (E_{2g} phonon) observed in h-BN and is blue shifted around $4cm^{-1}$ from the

peak position 1366 cm^{-1} for bulk h-BN as shown in **Figure 2.6 (e)** [156, 200]. The observed blue shift for monolayer h-BN expected due to slightly shorter B–N bond resulting in hardening of the E_{2g} phonon mode [200, 261]. However, on increasing the layer thickness, the E_{2g} mode starts to red shift with increased intensity due the softening of B-N bonds by interlayer interactions as represented in **Figure 2.6 (e)** and its inset. More specifically layer number of h-BN can be identified by full width half maxima (FWHM) of E_{2g} peak, its intensity and position.

2.3.3 Scanning electron Microscopy (SEM)

Scanning electron microscope (SEM) is routinely used for the characterization of graphene and h-BN morphology by following its first use in CVD synthesized graphene on Cu [113]. SEM can generates the high resolution images of specimen by utilizing secondary scattered electrons received on the SEM detector form the samples surface when focused beam of high energy electron beam incident on the surface. SEM and field emission SEM (FESEM) images presented in this thesis were obtained by using JEOL JSM-5600 and JEOL JSM-7800F respectively operated in the accelerating voltage range of 2-20 keV. The microscopic details of graphene and h-BN domains morphologies, wrinkles and etched structure were carefully analyzed with the help of SEM. SEM can be further utilized to obtain the varying layer number (ad-layers) within a graphene and h-BN domains or within a film.

2.3.4 Electron Backscattered Diffraction (EBSD)

Electron back-scattered diffraction (EBSD) is a micro-crystallographic

characterization technique in SEM to obtain the quantitative information of phase analysis and orientation of sample. The micro-structural information of sample is obtained from the Braggs diffraction of the electrons by the sample crystals when fine beam of high-energy electron beam incident on the sample surface. EBSD analysis has been carried out on graphene and h-BN deposited on Cu substrate to understand the substrate grain orientation effect on the growth of graphene and h-BN [216, 262, 263]. Polycrystalline Cu foils used for growth process and their influence on the grown graphene and h-BN is intensively studied. In this thesis, JEOL JSM-7001FF operated by an accelerating voltage 20 keV with 70° angle of incident beam and is equipped with an EBSD detector performed EBSD analysis.

2.3.5 Atomic force Microscopy (AFM)

An atomic force microscope (AFM) has capabilities of spatially measuring the surface topography on an atomic scale. That is why ever since the discovery of graphene, AFM is relied as a characterization tools along side with OM [12, 183]. This is a straight way to determine the thickness of graphene and h-BN with approximate interlayer distance. However, the measured height of monolayer is prone to be higher than in theory for both graphene and h-BN. Various impurities and functional groups as well as the unavoidable solvent derived from the transfer process may account for the relatively larger layer thickness [74, 150, 183, 205, 264, 265]. Therefore, AFM is a complementary approach for the thickness measurement. AFM (JSPM-5200) study was carried out for the as-synthesized and transferred graphene and h-BN by using CNF incorporated Si tip cantilever in contact mode.

2.3.6 Transmission Electron Microscopy (TEM)

In transmission electron microscopy (TEM), a fine beam of electrons is transmitted through an ultra-thin specimen and the image is recorded based on the information of interacting beam with the specimen as it passes through. TEM is found to be promising characterizing tool for graphene, h-BN and other 2D materials due to their ultra thin ness. The elemental composition, crystallinity, layer number (at the folded and twisted edges) information, defects etc. can be obtained precisely by using TEM. In this thesis, JEM ARM-200F and JEOL 2010 were used for the structural analysis of graphene and h-BN.

2.3.7 X-Ray Photoelectron Spectroscopy (XPS)

X-ray photoelectron spectroscopy (XPS) is a spectroscopic technique that measures the elemental composition of a sample surface by irradiating a substrate with monochromatic X-rays. The photo-emitted electrons from the sample surface (5-10 nm depth from surface) being received at the electron energy analyzer and hence resulting spectra produced. Thus produced spectra of the binding energy and intensity of a photoelectron peak from which the elemental composition, chemical state, and quantity of a detected element can be determined. In this thesis, the elemental composition and bonding of foreign elements on Cu substrates as well as grown materials (h-BN and graphene) were acquired by XPS (Versa Probe) using a monochromated Al Kα excitation source (1486.6 eV).

Chapter 3

Influence of copper foil polycrystalline structure on graphene crystals growth and anisotropic etching

3.0 Introduction

Growth of single crystals, bi-layer stacking, and controlling layer numbers in large-area continuous film are explored by the CVD process for practical device applications [51, 139, 140, 266-270]. In this prospect, carrier gases, precursor materials, catalyst substrates, reaction zone temperature and pressure etc. have been realized as the fundamental aspects for graphene growth by most of the research groups [263, 271-273]. Difference in shape, size, orientation and quality of graphene crystals with substrate crystallographic nature have been explored [263, 274, 275]. Variation of nucleation density of graphene with different faces of polycrystalline Cu substrate has been also reported [275, 276]. At the same time, H_2 gas concentration and base pressure in a CVD process have been explored on the graphene crystal growth on Cu surface [141, 277]. Thus, graphene crystals growth process on polycrystalline Cu substrate has been significantly investigated and reported on the effect of various CVD parameters on graphene growth. Another important aspect is the anisotropic etching of graphene lattice, which enabled to understand growth dynamics, wrinkle formation as well as enabling fabrication of well-defined graphene nanostructures [278-281].

Recent studies have revealed anisotropic etching process of graphene and other 2D materials for nanoribbon fabrication with control edge structures [282-284]. Anisotropic etching of the graphene basal plane has been achieved with metal nanoparticles in presence of H_2, selective oxidation, and water vapor at an elevated temperature [283-287]. It has been also observed that graphene etching in H_2 atmosphere can be caused by the ppm level oxidizing impurities in 99.999% H_2 gas [288]. The H_2 etching of graphene crystals on Cu substrate also provide significant information on growth as well as detecting graphene wrinkles [289]. Very recently, Zhang et al. had shown formation of different graphene morphologies depending on hydrogen etching process [290]. Edge passivation of CVD graphene has been observed based on the etching behavior.

The etching process can be an ideal reverse phenomenon to recognize graphene growth behavior as well as opening new opportunities to control the graphene structure. In all of the previous studies, effect of the polycrystalline nature of Cu foil has not been explored for etching behavior of graphene crystals. This chapter reveals the influence of Cu foil crystallographic structure on as-synthesized graphene anisotropic etching process. Graphene crystals were synthesized on polycrystalline Cu foil by a LPCVD system. Post growth etching of such graphene crystals significantly affected by the crystallographic orientation of Cu grains, where the difference in graphene structures depending on Cu grains can be recognized.

3.1 Experimental

The Cu foil (Nilaco, 99.9% purity) of thickness 20 μm was used in these experiments of graphene growth. Bare Cu foil of the size ~2×4 cm^2 was kept on boat and loaded into the horizontal tubular growth furnace. A LPCVD system is developed for graphene growth using

solid source precursor. The CVD chamber was evacuated by a rotatory pump and base pressure of 2 Pa was maintained. Here, it should be noted that the solid source vapor pressure is significantly important, such that the inserted precursor does not evaporate at low pressure. The growth furnace was heated at 10.5 ^{O}C/min from room temperature to 1050 ^{O}C with 2.8 standard cubic centimeter per minute (sccm) H_2 flow at a pressure of 13 Pa. Cu foil annealed for 1 hour without changing gas to remove impurities and increase the grain size. PS as the carbon source was evaporated (detailed discussion of PS is provided in chapter 4) for 20 min and carried to growth chamber with H_2. For the evaporation of carbon, second furnace was used and programmed with average heating rate of 3 ^{O}C/min. After the growth process, the growth furnace was rapidly cooled down to room temp within 30 min.

3.2 Results and Discussion

Figure 3.1 (a) shows optical microscope image of graphene crystals synthesized on various Cu grains of a Cu foil in a LPCVD technique. It can be observed that in some of the Cu grain the graphene domains are less dense and larger in size, while on some other grains there are significantly dense and smaller domains. This can be related to the influence of Cu crystallographic structure and anisotropy in carbon species diffusivity for graphene nucleation and growth process [291]. **Figure 3.1 (b)** shows a FESEM image of the nucleated graphene crystals on different Cu grains. The structure of the graphene crystal varies with Cu grains is also observed from the optical microscopy analysis. **Figure 3.1 (c)** shows corresponding EBSD analysis of Cu grain bellow the graphene crystal. The EBSD analysis clearly confirmed difference in Cu crystallographic orientation, which influence the size and shape of graphene crystals. The observed result can be correlated to previous findings for methane based CVD process [263, 274]. Raman studies were carried out for the graphene

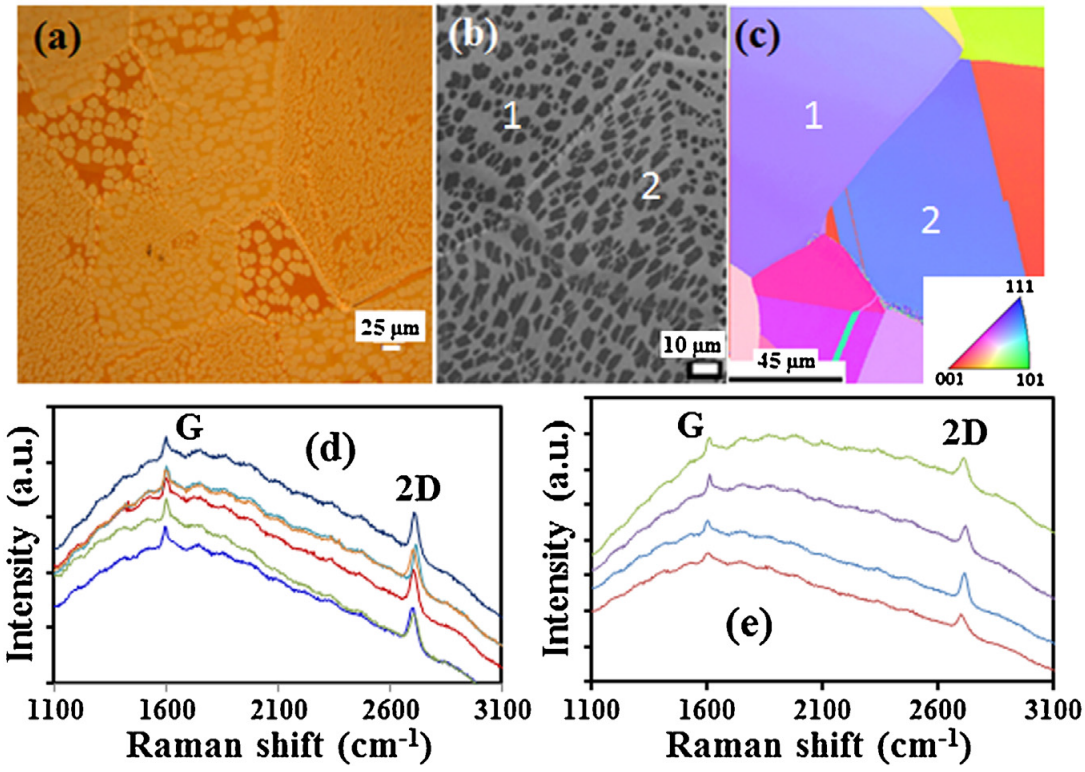

Figure 3.1. (a) Optical microscope image of graphene crystals synthesized on various Cu grains of a Cu foil by LPCVD technique. (b) FESEM image of the nucleated graphene crystals on different Cu grains and (c) Corresponding EBSD analysis. (d) and (e) Raman analysis of graphene at two different Cu grains.

crystals with contrasting shape on different Cu grains. **Figure 3.1(d) and (e)** shows Raman spectra at two different place of the Cu foil with different shape of graphene crystals. A graphitic G band and second order 2D band are observed at 1580 and 2700 cm^{-1}, respectively. In all the spectra 2D peak intensity is higher than that of G peak, confirming monolayer graphene in both the places. The obtained result of graphene crystal growth on polycrystalline foil can be correlated with various previous studies [274-276]. In contrast to previous report, this chapter demonstrates the anisotropic etching behavior of such graphene crystals on polycrystalline Cu surface. As followed, the etching behavior of graphene crystals is elaborated depending on the copper crystallographic structure.

The stripes and wrinkles of graphene on Cu grains and effect of anisotropic etching were explored. **Figure 3.2 (a)** shows an FESEM image of graphene crystals on polycrystalline Cu grains and grain boundaries. The formation of parallel stripes in the individual graphene crystals on Cu surface was observed. It has been reported that the graphene stripes are due to Cu surface reconstruction and related to two main factors, namely, the distribution of Cu grains and the cooling rate after graphene growth [292]. The stripes directions are different on different Cu grains. The formation of Cu grains with differ-

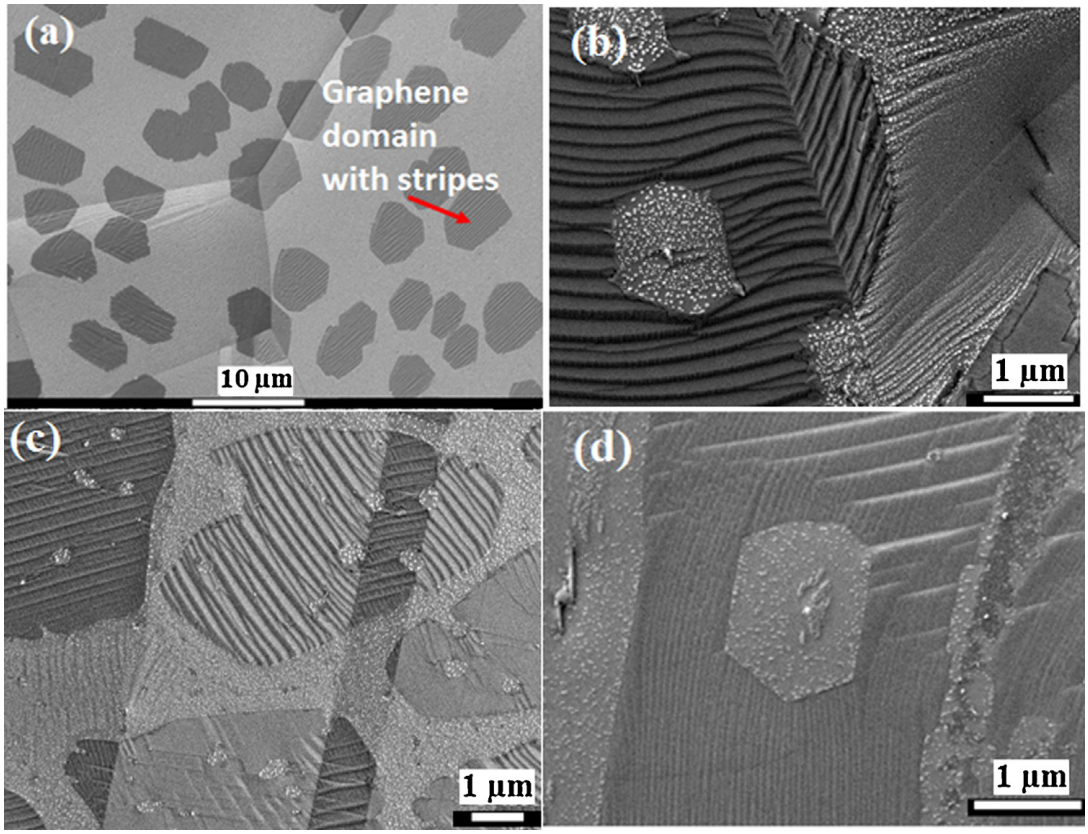

Figure 3.2. (a) Graphene crystal on different Cu grain with parallel stripes on individual crystals. (b) Hexagonal hole formation near Cu grain boundaries, where the graphene stripes direction are different in two neighboring Cu grain. (c) Difference in stripes direction of graphene on Cu grain and twins. (d) Hexagonal hole formation in the graphene crystal in presence of stripes and wrinkles.

ent orientations during high temperature annealing process for graphene growth determines the appearance of the stripes. **Figure 3.2 (b)** shows graphene on two different Cu grains and formation of stripes across the grain. A hexagonal hole with anisotropic etching also can be observed, which is independent of the graphene stripes directions. **Figure 3.2 (c)** shows the etched graphene crystal across twin boundaries and the strips direction in individual graphene on Cu grain and twins. It was observed that the stripes of same graphene crystal can be in different directions in the twin and Cu grain. Finally, the effect of stripes and wrinkles in formation of hexagonal holes by anisotropic etching process was confirmed. **Figure 3.2 (d)** shows a hexagonal hole formation in the graphene crystal in presence of stripes and wrinkles. The wrinkles were formed perpendicular to the stripes as also observed from APCVD technique [289, 292]. The hexagonal hole edges are formed independent of the stripes and wrinkles in the graphene synthesized by the LPCVD process. The observation of the Cu crystallographic orientation dependent etching effect of graphene crystals as well as formation of hexagonal holes in presence of stripes and wrinkles can be significant to understand the etching process in details.

Figure 3.3 (a) shows an FESEM image of the etched graphene crystals on different Cu grains. Dendritic and regular graphene crystals on two different Cu grain separated by the grain boundaries can be observed. The dendritic crystals were etched symmetrically from the branches of individual lob creating fractal pattern (position 1 of Cu grain), whereas etching of regular crystal from edge or creating hexagonal holes (position 2 of Cu grain). Formation of hexagonal holes and ribbon-like structures can be attributed to anisotropic etching process. **Figure 3.3 (b)** shows a higher resolution image of the dendritic etched graphene crystals. The image clearly shows lob structure of the graphene crystal and etched pattern similar to snowflake-dendritic crystals. Similarly, **Figure 3.3 (c)** shows regular

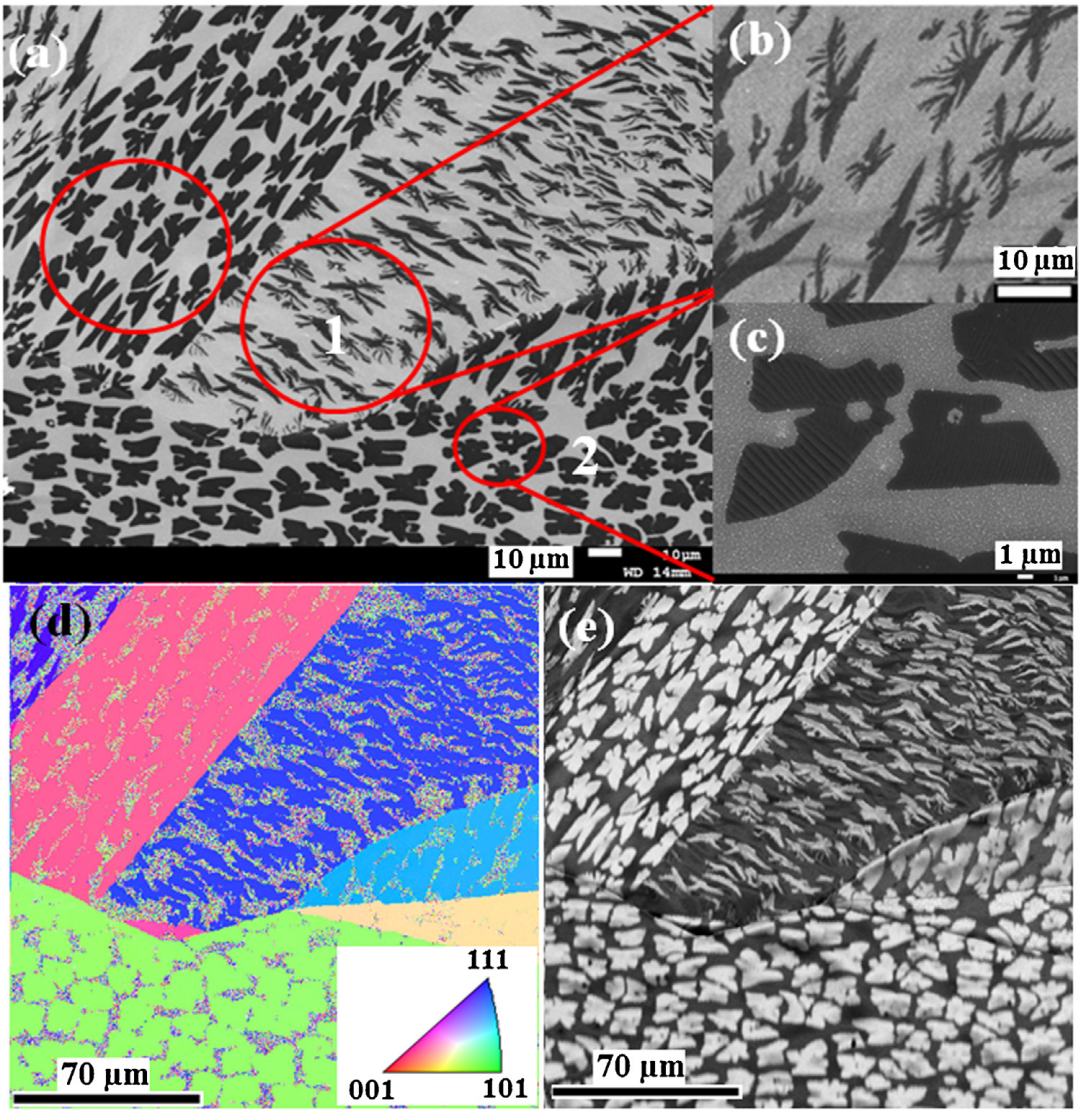

Figure 3.3. (a) FESEM image of the etched graphene crystals on different Cu grains, (b) and (c) higher resolution FESEM images at two different Cu grain with contrasting graphene etched structures. (d) Corresponding EBSD analysis of the Cu surface with different graphene etched structures. (e) Image quality parameter map for the EBSD pattern.

graphene crystals etched from edges or creating hexagonal hole, which can be related to Thangaraja et al. findings [281]. The etching of graphene crystal evidently shows effect of graphene growth on different grain and their anisotropic etching. ~~We carried out~~ EBSD analysis was carried out to confirm the Cu grain with respect to the etched graphene

structures. This will provide us the understanding of graphene growth and etching behavior on individual Cu grain in the LPCVD process. **Figure 3.3 (d)** shows EBSD mapping image with respect to **Figure 3.3 (a)**, in presence of the synthesized graphene crystals. The Cu grain structure are clearly visible in presence of graphene than that of oxidized region of Cu foil as shown in **Figure 3.3 (d)**. The dendritic crystals with lob structures are obtained on the (111) Cu grain. The dendritic lobed structure of the graphene domains suggests the growth mechanism associating with the six-fold symmetry of Cu(111) facet. Formation of dendritic lobed structure on Cu(111) using the solid PS as carbon source in the LPCVD process also can be related to the substrate mediated growth process, which is also observed for ethanol CVD process [293]. Nevertheless, regular graphene crystals are observed on the other facet of Cu grain. Due to the differences in nucleation and growth of graphene crystal on the polycrystalline Cu grain, the anisotropic etching behavior also significantly changes. This provides us tool to correlate the graphene growth and their anisotropic etching behavior. **Figure 3.3 (e)** shows image quality parameter mapping for EBSD pattern as of **Figure 3.3 (d)**. The image quality significantly changes due to oxidation of the Cu surfaces, while the image quality is higher for intact Cu surface in presence of the monolayer graphene. Thus, the EBSD analysis provides clear structural information of anisotropic etched graphene crystals on different Cu grains.

The graphene structures on two Cu grains were further investigated by Raman spectroscopy analysis. **Figure 3.4 (a)** and **(b)** shows FESEM image of the etched lobed dendritic and non-dendritic graphene crystals. Raman studies were carried out to investigate the structural properties of these two graphene crystals. **Figure 3.4 (c)** shows Raman spectra of the etched dendritic crystals on Cu foil. Graphitic G and second-order 2D Raman peaks are observed at around 1589 and 2704 cm^{-1}, respectively. The intensity of G peak is lower than

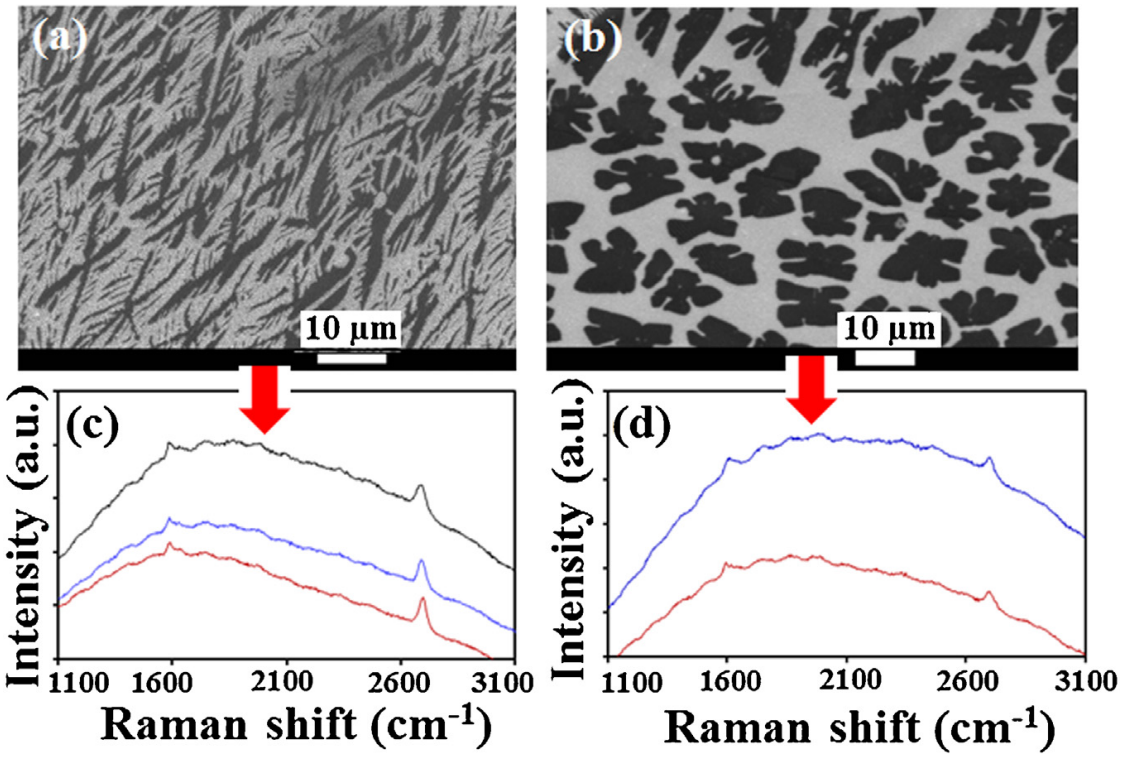

Figure 3.4. (a) Dendritic and (b) regular graphene crystal on two individual Cu grains. Raman spectra for the respective (c) dendritic and (d) regular graphene crystals.

that of 2D peak, indicating a monolayer graphene. In contrast to Thangaraja et al. findings, the dendritic crystals are monolayer graphene, whereas few-layer dendrites are formed in APCVD [281]. The regular graphene crystals as of **Figure 3.4 (d)** show a graphitic G and second-order 2D Raman peaks at around 1587 and 2705 cm^{-1}, respectively. There was not significant difference in 2D to G peak intensity than that of previous case. Raman analysis confirms formation of a monolayer, independent of dendritic or non-dendritic structural morphology of the graphene crystals.

Figure 3.5 (a) shows FESEM image of etched graphene crystals on different Cu grain to present the variation in etching rate. As shown in the figure, there is significant difference in etching rate at position 1 and 2. This suggests sharp contrast in graphene crystal structure

in the two different Cu grains. **Figure 3.5 (b)** and **(c)** shows the higher resolution FESEM images at position 1 and 2 of **Figure 3.5 (a)**. **Figure 3.5 (b)** shows smaller graphene flakes and ribbon like structures owing to higher etching rate at that particular Cu grain. **Figure 3.5 (c)** shows larger graphene flakes with etching in contrast to previous case. The Cu grain structure was explored to establish the cause in difference in etching

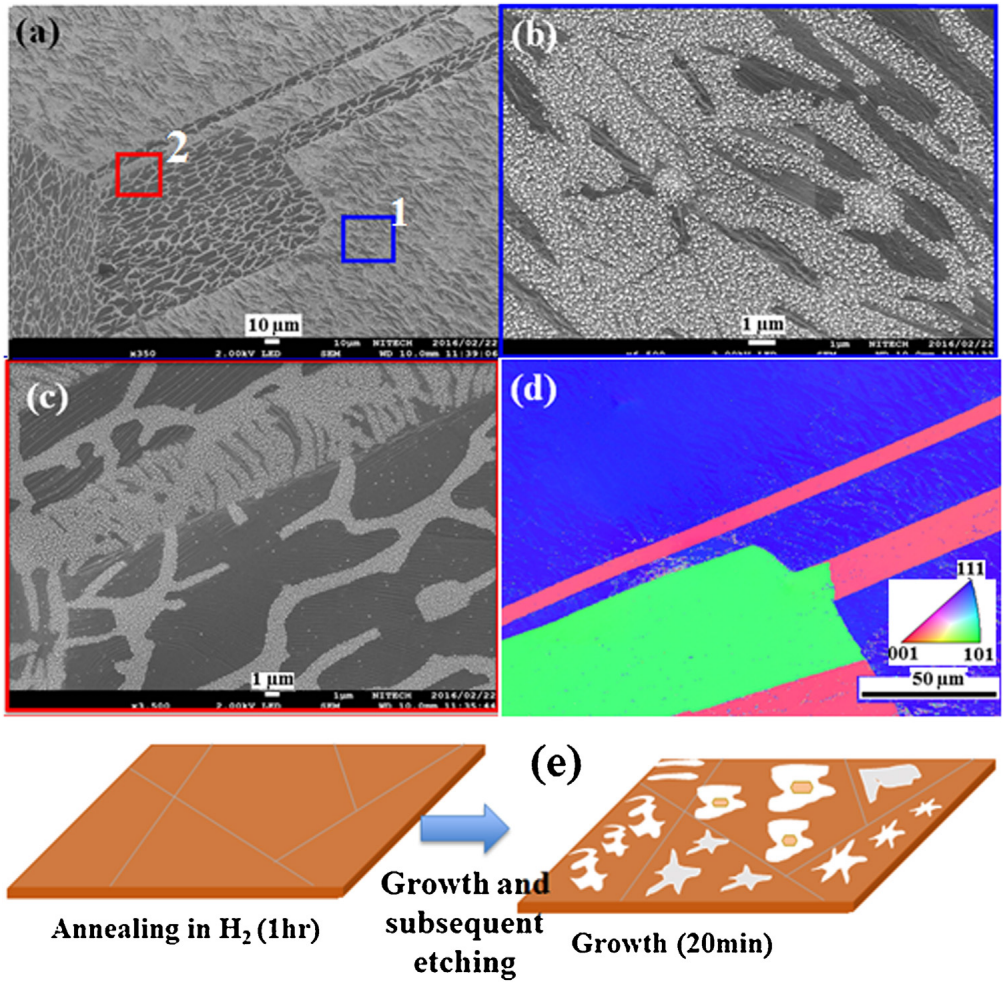

Figure 3.5. (a) Etched graphene crystals with dissimilar etching rate on different Cu grain. High resolution FESEM images for (b) highly etched and (c) less etched graphene crystals. (d) Corresponding EBSD analysis of the Cu surface with different graphene etched structures. (e) Schematic representation of graphene etched structure on polycrystalline Cu depending on the grain orientation.

rate. **Figure 3.5 (d)** shows corresponding EBSD analysis of the Cu surface with different graphene etched structures. In this case oxidation of the Cu surface was less so clear crystallographic structure in presence of the monolayer graphene also can be obtained. Faster graphene etching is observed on the Cu (111) grain, attributing to the minimum surface energy compared to other facets. Thus, it was observed that not only the growth of graphene crystals but the etching rate and structure also significantly depend on crystallographic nature of the Cu surface. **Figure 3.5 (e)** shows a schematic of the graphene etched structure with distinct morphology on different Cu facets. These etching behaviors can be related with hydrogen interaction, such as adsorption and desorption on various Cu facets [294-296]. The inter- action of atomic hydrogen with the basal Cu grains and thereby with carbon atoms can determine the etching rate and structures of the graphene crystals. The understanding of etching process will enable to identify the morphology of the graphene depending on the particular Cu facet.

3.3 Conclusions

In this chapter, the influence of Cu foil crystalline structure on as-synthesized graphene anisotropic etching process have been demonstrated. Graphene crystals were synthesized on polycrystalline Cu foil by a LPCVD technique using solid carbon source. Microscopic analysis shows difference in shape and size of graphene crystals with dis-similar nucleation within closure vicinity of neighboring Cu grains. It has been observed that the synthesized graphene stripes directions are different on different Cu grains and twins. Hexagonal hole with anisotropic etching are formed independent of the stripes and wrinkles in the graphene synthesized by the LPCVD process. FESEM and EBSD analysis of graphene crystals were performed after the etching process to visualize the etched direction and particular shapes formation. The difference in etched direction and formation of graphene

structures depending on the base Cu grain orientations were observed. The finding can be significant to understand etching kinetics of graphene crystals synthesized on polycrystalline Cu surface, and thereby recognizing the growth and etched structures.

Chapter 4

Effect of copper foil annealing process on large graphene domain growth by solid source-based chemical vapor deposition

4.0 Introduction

Variation of crystals size, structures and nucleation density of graphene crystals within closure vicinity of Cu grains was found to be strongly influenced by the crystallographic orientation of Cu as discussed in Chapter 3. Polycrystalline Cu employed for the growth substrate should be processed such a way that the nucleation density could be highly reduced. Besides this, the supply technique of precursor molecules essentially should not to initiate the secondary nucleation. Recently, significant effort has been given to synthesize large single crystal graphene on Cu and other catalytic substrates using the low pressure- and atmospheric pressure- CVD techniques [111, 126, 131, 266, 267, 297]. In this process, various factors significantly affect graphene nucleation and growth on Cu surface, such as, gas composition, growth temperature, flow rate of carbon source, and substrate surface [275, 293, 297-299]. Graphene domains with various shapes and crystalline structure have been obtained in a CVD process depending on the growth parameters. Graphene crystals nucleation and growth kinetics on substrate surface are important aspects, which control formation of monolayer, bi-layer, hexagonal structure, layer-stacking, and dendrite growth process [134, 137, 268, 300].

Creating an oxide layer on Cu surface and pre-annealing process to reduce nucleation density are important aspects to obtain large graphene domains [140]. Thus, it signifies that the processing of Cu surface is a critical step to achieve growth of larger graphene domains.

Sharma et al. reported the growth of individual graphene crystals on Cu foil using waste plastic as solid carbon source [117]. The waste plastic is composed of polyethylene- and PS-based polymers, which decompose to produce carbon-containing organic molecules. In a solid source CVD process, various other carbon-containing organic molecules can be used for graphene growth [115, 116, 301]. The solid precursor material can be directly inserted into the CVD chamber; thus, solid wastes or various other non-gaseous hydrocarbons can be used as precursors in the developed process without supplying hydrocarbon gas from external source. This chapter explores graphene growth using solid PS as precursor in the APCVD process on processed Cu foil surface. PS has been significantly used in production of plastic-based materials and single largest components in various waste plastics [302, 303]. PS is formed with inter- connection of styrene monomers, where benzene, toluene, and styrene molecules can be obtained with decomposition. These types of organic molecules contain both π and σ-bonds, in contrast to only C–H σ-bonds of methane (CH_4) molecules. Dehydrogenation and decomposition of these organic molecules for graphene growth can be significantly affected by the catalytic Cu surface [137, 293, 304]. The solid PS precursor is investigated for graphene synthesis as an alternative to gaseous sources, considering the weaker C–H bond energy (~292–305 kJ/mol) than that of methane (410 kJ/mol) [242]. The suitable melting point (~240 ^{O}C) and vapor pressure of PS allows us to control heating and evaporation of the precursors for longer growth duration. The key factor to achieve growth of large graphene domains in the CVD process is controlling the metal catalyst surface structure. Here, the transformation of Cu surface morphology and crystallographic structures in the

annealing process has been reveled by EBSD analysis to achieve large graphene domain growth.

4.1 Experimental Methods

Identical Cu foils as discussed in section 3.1 were polished by electroless process in a $FeCl_3$ solution. 5 g of $FeCl_3$ was dissolved in 10 ml of HCl and 100 ml of deionized (DI) water. Electroless polishing was carried out by dipping the Cu foil pieces into the solution for around 15 second. Subsequently, Cu foil pieces were rinsed with DI water. Finally, Cu pieces were rinsed with acetone by sonication to remove any residual $FeCl_3$.

PS of molecular weight ~192000 was used as a solid precursor for graphene synthesis alike in chapter 3. **Figure 4.1 (a)** shows the molecular structure of PS [$(C_8H_8)n$]. The Cu foils were put in the horizontal quartz tube of single furnace CVD system as shown in **Figure 4.1 (b)**. Temperature of the furnace was increased by 10.5 ^oC/min up to 1050 ^oC in Ar atmosphere before maintaining constant temperature of 1050 ^oC in H_2 environment for 4 hour. It took 100 min to reach the set temperature of the furnace in Ar atmosphere; within this period, the surface of Cu foil oxidized significantly to form a copper oxide layer [**Figure 4.1 (c)**]. Subsequently, the copper oxide layer was reduced and Cu surface recrystallized by annealing in H_2 atmosphere. PS was evaporated in a control process, such that the temperature on the precursor increased by 5 ^oC/ 20 min for 4 hour as shown in the temperature profile **Figure 4.1 (d)**. For the graphene growth, a mixture of Ar and H_2 in 98:2 sccm is used as carrier gas. Subsequently, the CVD furnace was cooled down to the room temperature in the same Ar and H_2 gas mixture.

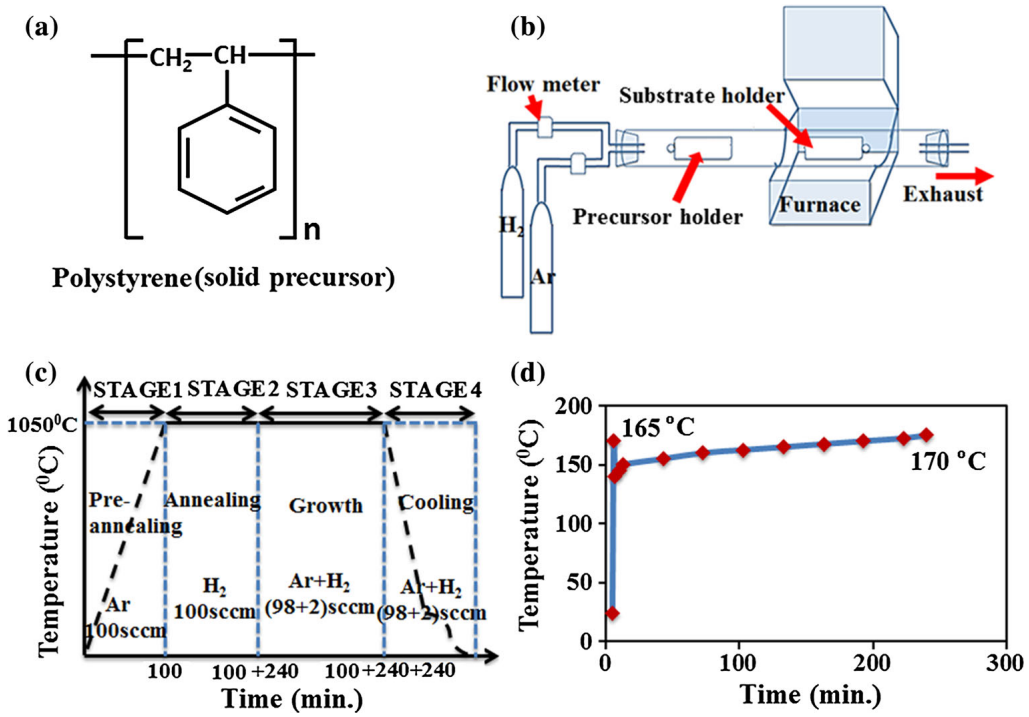

Figure 4.1. (a) Molecular structure of PS [$(C_8H_8)n$]. (b) Schematic diagram of the graphene synthesis process using solid PS precursor. (c) Four different stages of annealing of Cu foil, graphene growth, and cooling process. (d) Precursor evaporation profile (time vs temperature) for uninterrupted graphene growth.

4.2 Results and Discussion

The as-purchased Cu foil was treated with $FeCl_3$ solution to remove the impurity layer from top surface. The electroless polishing also enables to remove the Cu rolling lines to obtain a much uniform Cu surface for better lateral growth of graphene. The pre-treated Cu foil was annealed in Ar and H_2 atmosphere to achieve growth of large graphene domains. **Figure 4.2 (a)** shows photographs of Cu foils after the annealing treatments. Significant difference in Cu foils color can be observed with surface oxidation. The Cu foils pieces were heated in Ar atmosphere in the initial stage, which significantly oxidize the Cu surface.

Subsequently, annealing in H_2 the oxidized layer was reduced and Cu surface recrystallized. **Figure 4.2 (b)** shows XPS analysis of the Cu surface at different stages of the annealing treatment. The Cu sample was removed only after heating in Ar atmosphere (stage 1), which shows reddish color of the Cu surface indicating surface oxidation. Cu2p XPS spectra with four split peaks for the oxide surface were observed as shown in **Figure 2b** (stage 1). The peak centers at 932.6 and 952.5 eV correspond to Cu $2p^{3/2}$ and Cu $2p^{1/2}$, respectively. The other two peaks at around 944.1 and 962.5 eV are known as shake-up satellite peaks of copper oxide. The shake-up features of Cu2p XPS spectra clearly indicate oxidation of Cu foil and formation of an oxide surface. Now, annealing the substrate in H_2 atmosphere for 1 hour, the Cu 2p shake-up satellite peaks reduce, and further annealing for 4 hour (stage 2), the oxidation states reduces significantly. This suggests reduction of oxide layer and successive recrystallization of Cu surface. Previously Gan et al. [305] has demonstrated significant reduction in nucleation density by annealing in Ar only in the preheating step, followed by annealing in Ar/H_2 atmosphere. Here, it was observed that the oxidation and subsequent recrystallization of Cu foil occurred with the annealing process in Ar and H_2 atmospheres, respectively. The oxidation and subsequent recrystallization process can reduce graphene nucleation points and provides a smother surface for lateral growth of graphene domains [305]. The Cu surface structures were further investigated by EBSD mapping analysis of Cu surface.

EBSD analysis was performed at every step of annealing process to explore the transformation of crystallographic structures of the Cu foil. **Figure 4.3 (a)** shows EBSD mapping image of the as-received Cu foil without any annealing treatments. The as-purchased Cu foil does not contain any regular grain structures, where the smaller grains consist with various orientations. Now, the grain structure of Cu foil was analyzed at various

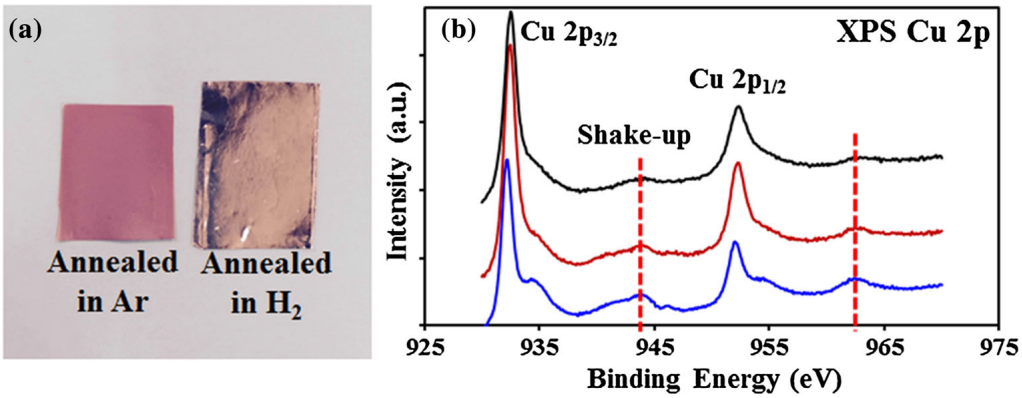

Figure 4.2. (a) Photographs of Cu foils after the annealing treatment in Ar and H_2 atmospheres. (b) XPS spectra of the Cu surface at different stages of the annealing treatment.

stages of annealing process. **Figure 4.3 (b)** shows EBSD mapping image of the same Cu foil after heating the Cu foil from room temperature to 1050 ^{o}C in Ar atmosphere. Significant transformation in grain structure than that of the as- purchased Cu foil can be observed. Cu grains of 20–25 μm were obtained, where the crystallographic orientations of the grains are (111), (101), (001), and several other higher index planes. Subsequently, the Cu foil was annealed in H_2 atmosphere at 1050 ^{o}C for 4 hour, to achieve recrystallization of Cu surface. **Figure 4.3 (c)** shows EBSD mapping image of the Cu foil in the intermediate stage of 1 hour annealing in H2 atmosphere. The Cu grain size enhanced significantly (as high as 500 μm) than that of the previous case; however, the crystallographic orientations remained random. Now, increasing the annealed duration to 4 hour not only enhanced the Cu grain size, but also Cu(111) crystallographic orientation was predominant as shown in **Figure 4.3 (d)**. It is well known that Cu crystallizes in the simple fcc crystal structure, where the (100), (110), and (111) surfaces are with the lowest surface energy. Again, Robinson et al. [306] has reported that Cu(111) surface is with lower surface energy among the lower index crystalline surface. This may be due to the fact that annealing the Cu foil around its melting temperature for longer duration, the Cu(111) predominantly appears in the Cu foil surface. Thus, the

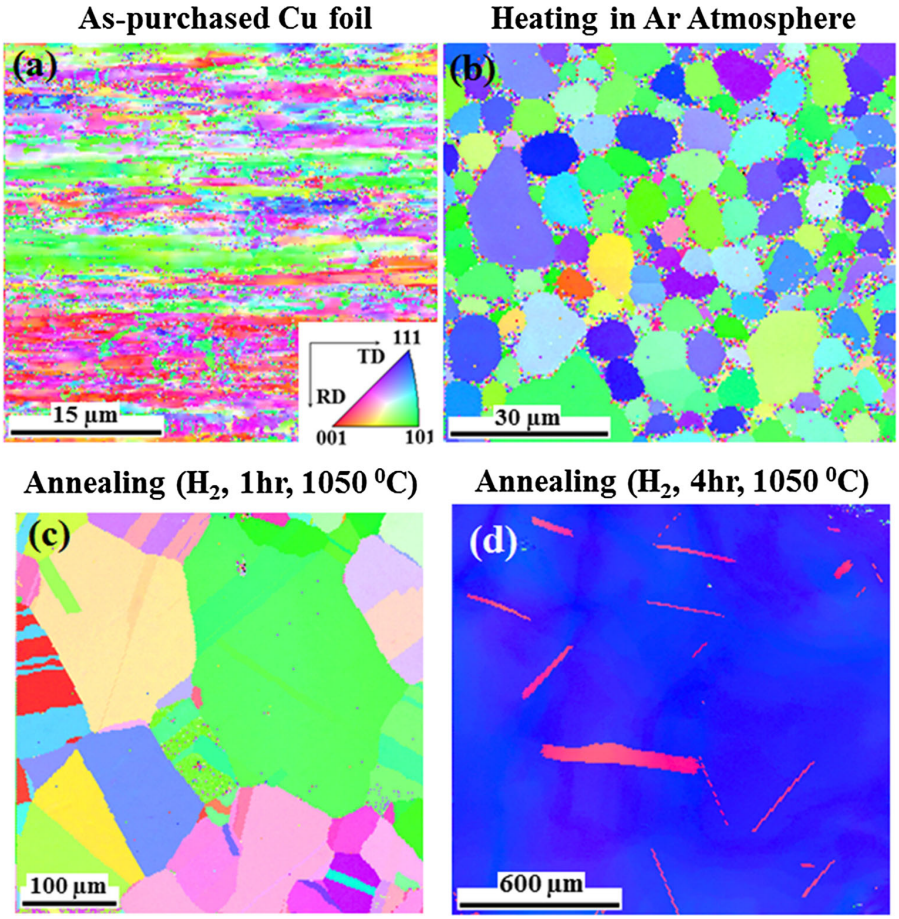

Figure 4.3. EBSD mapping image presenting the crystallographic nature of (a) the as-received Cu foil without any annealing treatments, (b) after heating the Cu foil up to 1050 ^{o}C (1 hour 40 min duration), (c) annealing in H_2 atmosphere for 1 hour (intermediate stage), and (d) annealing in H_2 atmosphere for 4 hour duration.

pre-treated Cu foil with preferential crystallographic orientation can be most suitable to grow larger graphene domain in developed solid source-based CVD process. Thus, it has confirmed the transformation of Cu grain structures at various annealing steps with different gas atmospheres and annealing durations.

Figure 4.4 (a)–(c) shows optical microscope images of graphene domains synthesized on the treated Cu surface. The optical images were taken with mild oxidation of the Cu

substrates. Round and hexagonal shapes with brighter contrast on the Cu foil represent the graphene domains. Growth of several such individual graphene domains was observed on the Cu foil, where the lateral size is measured to be 300–825 µm. The graphene domains were obtained across different Cu grain and grain boundaries, which has been also confirmed in various other reports. In this particular process, growth of round- [**Figure 4.4 (a)**] as well as hexagonal [**Figure 4.4 (b)**] -shaped graphene domains with large lateral size has been observed. Growth of individual graphene domain with a distinct shape was further confirmed by FESEM analysis.

Figure 4.5 (a) – (c) shows SEM images of the graphene domains on Cu foil. The lateral size of the graphene domains are around 350–825 µm and also confirmed by SEM

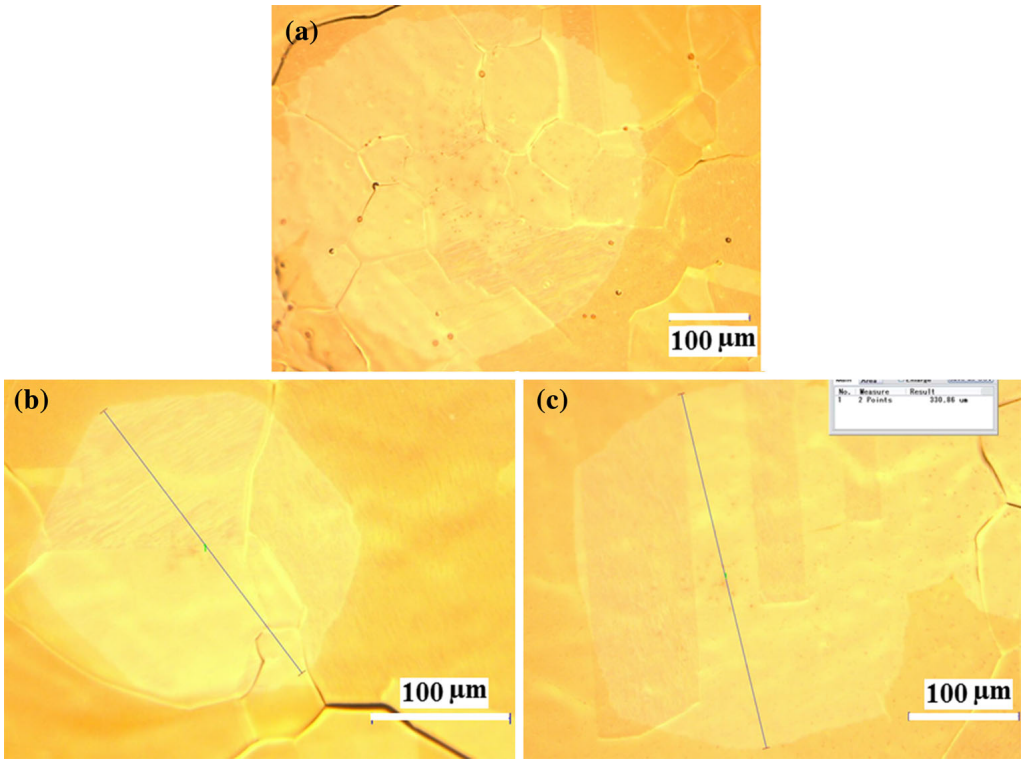

Figure 4.4. (a) – (c) Optical microscope images of graphene domains synthesize on the pretreated Cu foil. The optical images were taken with mild oxidation of the Cu substrates.

analysis. **Figure 4.5 (a)** shows a large individual graphene domain with lateral size of ~510 μm. The graphene domains also merged together for much larger graphene structures. **Figure 4.5 (b)** shows two individual graphene domain of the size around of ~350 μm merged together. Such two merged graphene domains were obtained in millimeter scale. **Figure 4.5 (c)** shows two individual graphene domain of size 560 and 825 μm merging to form a millimeter scale structure. The optical microscopy and SEM analysis clearly shows possibility of synthesizing millimeter scale graphene domains on the processed Cu foil. For the growth of large graphene domains, the PS precursor was evaporated slowly at a control

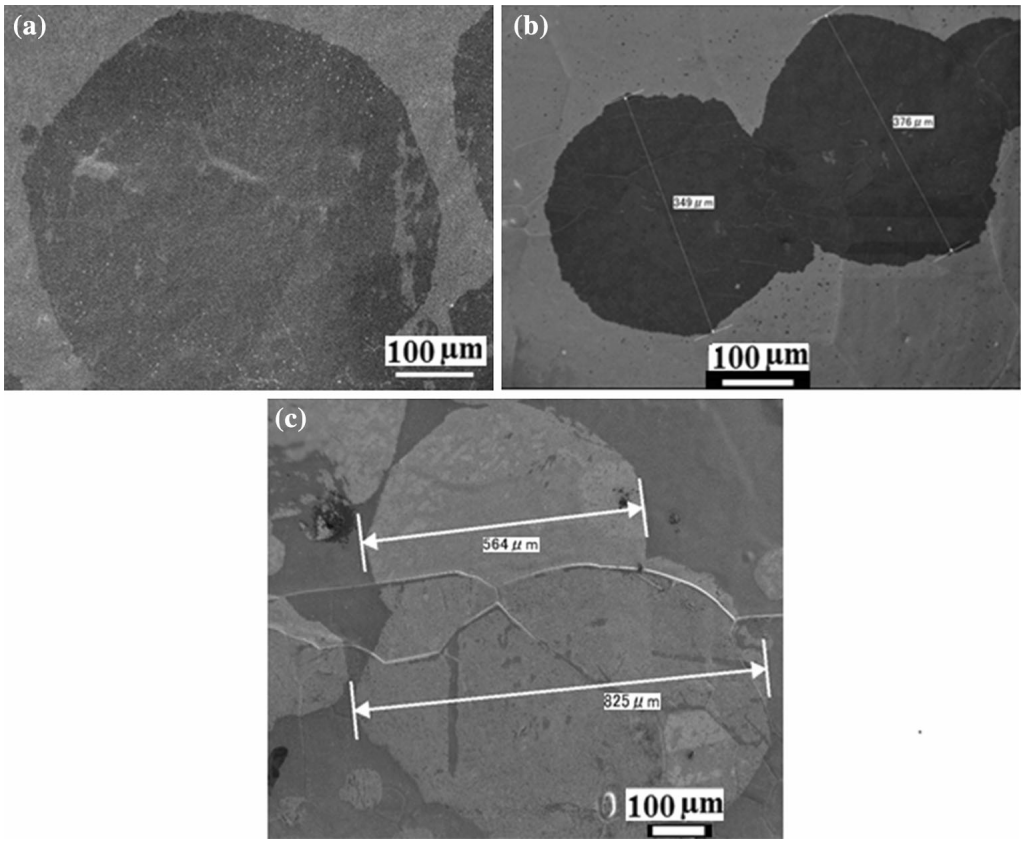

Figure 4.5. SEM images of (a) an individual graphene domain (~510 μm), (b) merging of two individual graphene domains of sizes 350 and 375 μm. (c) Formation of millimeter scale structures with merging of 560 and 825 μm large two graphene domains.

rate (stage 3). In the beginning, the precursor was heated to a higher temperature (165 ^{o}C) to initiate the graphene nucleation. Subsequently, the heating temperature was reduced and then gradually increased at a fixed rate as shown in **Figure 4.1 (c)**. In the growth process, controlling the carbon flux with evaporation of precursor plays critical role to obtain larger graphene domains [307]. It is important that there is continuous flow of organic molecules with the decomposition of PS for uninterrupted graphene growth.

Figure 4.6 shows Raman analysis of two different types of hexagonal-shaped graphene domains obtained in these experiments. **Figure 4.6 (a)** shows an optical microscope image of monolayer graphene domain of 240 μm size transferred on SiO_2/Si substrate, with a secondary nucleation site. Raman analysis was carried out at different points of the domains as shown in **Figure 4.6 (b)**. Graphitic G and second-order 2D Raman peaks are observed around 1589 and 2686 cm^{-1}, respectively. The FWHM of G and 2D peaks are around 15 and 33 cm^{-1}, respectively. The higher intensity of 2D peak than that of G peak corresponds to monolayer graphene. However, around the secondary nucleation sites smaller domain-like structures with more than single-layer graphene were observed. Raman study shows less defect in the as-synthesized monolayer graphene domain, while transferring to the SiO_2/Si substrate, defect- induced D band was observed due to the effect of impurities from the wet etching process. On the other hand, **Figure 4.6 (c)** shows an optical microscope image of a few-layer graphene domain transferred on SiO_2/Si substrate. Graphitic G and second-order 2D Raman peaks are observed around 1600 and 2690 cm^{-1}, respectively. The intensity of 2D peak reduces than that of G peak as measured inside of the graphene domain. The color contrast of the optical microscope images and the Raman spectra provides the evidence of graphene layer numbers in the domain. Such type of overlapped single hexagonal domain is difficult to identify on the as-synthesized Cu foil. Transferring the graphene on SiO_2/Si

substrate provides a clear insight of the structure. Previously, it has been reported that additional layers can grow in the underneath of the individual graphene domain, forming bi-layer or few-layer structures [308, 309]. Thus, in this chapter large monolayer as well as overlapped layers individual graphene domains were obtained on the pre-treated Cu foil. It is expected that this study will provide an insight for synthesis of centimeter scale single-layer, bi-layer, or tri-layer individual graphene domain by the solid source-based APCVD technique.

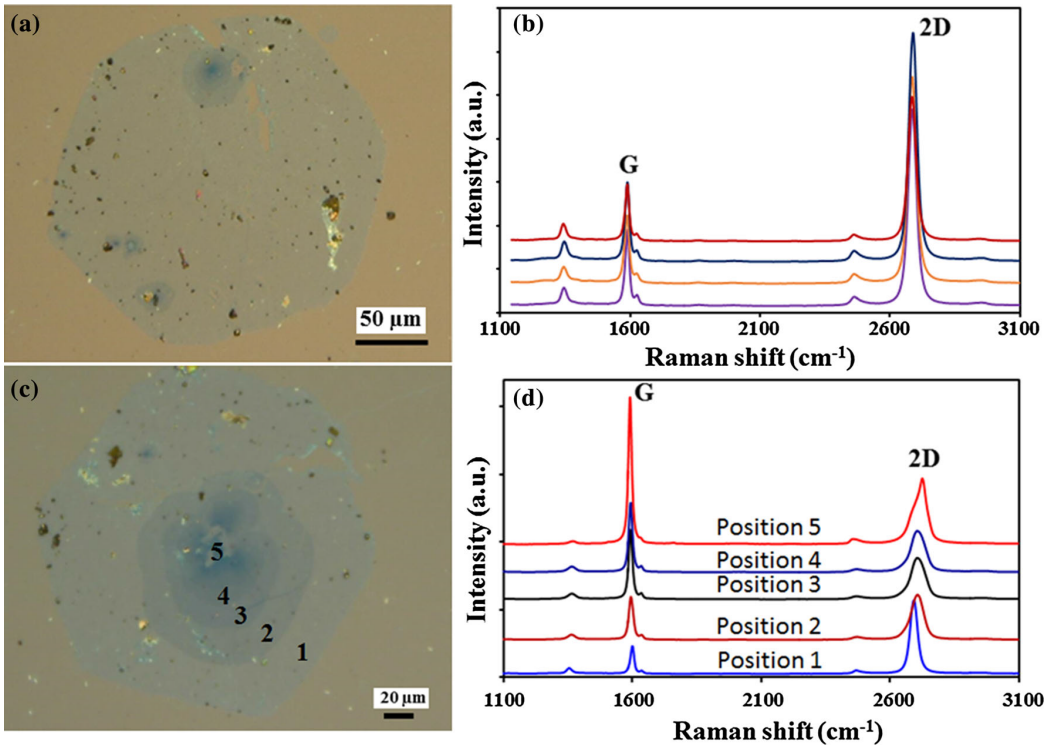

Figure 4.6. (a) Optical microscope image of monolayer graphene domain (~240 µm) transferred on SiO_2/Si substrate and (b) Raman spectra at different points of the domains (excluding the secondary nucleation point). (c) Optical microscope image of a few-layer graphene domain transferred on SiO_2/Si substrate (~243 µm). (d) Raman spectra at five different points for different layer numbers of the domain.

4.3 Conclusions

In summary, the transformation of Cu surface crystallographic structures in every step of an annealing process by EBSD analysis have been reveled to achieve large graphene domain growth. Electroless polished Cu foils were annealed at 1050 ^{o}C to obtain a smoother and favorable crystallographic surface with reduced nucleation density. Cu grains structures evolved at various stages of the annealing process and significantly transformed as confirmed by EBSD studies. Large grains (~560 μm) with preferential Cu(111) crystallographic orientation were obtained by annealing the Cu foil for 4 hour in H_2 atmosphere. Hexagonal- and round-shaped graphene domains with the size of 240 and 560 μm, respectively, were obtained on the processed Cu surface. Optical microscopy and Raman analysis showed the presence of monolayer graphene domain; however, few-layer individual domain was also observed depending on the absorbed carbon atoms on Cu surface. Our findings show the significant transformation of the Cu surface at different annealing stages to achieve less nucleation density and enabling growth of larger graphene domains.

Chapter 5

Morphology-Controlled Synthesis of Hexagonal Boron Nitride Crystals by Chemical Vapor Deposition

5.0 Introduction

As summarized in chapters 1 and 2, h-BN is well accepted as a better substrate than the conventionally used SiO_2 due to the absence of dangling bonds and charge traps. The highest mobility of graphene has been reported on an h-BN substrate, mimicking the property of freestanding graphene [15]. Exfoliating h-BN layers from a bulk h-BN crystal, however, is not very effective due to the presence of chemical bonding between neighboring layers [146]. Recent development in CVD has made large-area synthesis of high-quality h-BN film possible with high controllability over the quality and number of layers [51, 174, 310, 311]. For graphene case, the shape evolution of graphene crystal has been studied extensively with shapes ranging from hexagonal, triangle, round shape, flower shaped and fractals [117, 132, 312-314]. Crystals with different morphology offer different catalytic, magnetic and electronic behavior due to different edge orientations [315, 316]. Experimental factors, such as use of H_2, pressure inside growth chamber and surface orientation of underlying substrates, has been shown to have vital role in determining shape of graphene crystal [118, 312, 321]. In contrast for h-BN, few studies have been reported on morphological studies of h-BN

crystal and their experimental manipulation. Previously, Sharma et al. revealed the etching mechanism of triangular h-BN crystals in the presence of H_2 in CVD study [317].

This chapter discuses about the synthesis of high quality h-BN on Cu foil using APCVD with controlled shape of h-BN crystals ranging from conventional triangular to hexagonal shape. Very recently, it has been noticed that the precursor temperature has decisive role in the control of the morphology of synthesized h-BN crystal on Cu foil in the APCVD process. Tuning the supply rate of BN building blocks by manipulating precursor-heating temperature, even the transformation of hexagonal h-BN crystal to triangular symmetry was controllable. Hexagon shaped h-BN crystal is believed to have alternating B and N terminated vertices contrast with N terminated triangular crystals. Magnetic, catalytic and electronic properties of 2D crystals are found to be highly dependent on edge termination. In this regard, different properties can be expected from hexagonal crystals compared to triangular. Recent studies on synthesis of in plane hetero-structure of h-BN and graphene can also benefit from morphology-tuned synthesis of h-BN. Only N-C bond can be expected on interface during synthesis of triangular h-BN crystals followed by graphene growth. Whereas on hexagonal h-BN crystal surrounded by graphene, both B-C and N-C bonding is expected on interface providing rich variety of edge related of properties. These B-C and N-C edges can be cut into nano-ribbons and their properties explored for device fabrications.

5.1 Experimental Methods

In the present investigation, single furnace APCVD is used for the synthesis of h-BN on Cu substrate using AB (H_3NBH_3) as precursor. CVD system employed to grow h-BN consisted of single zone split furnace with quartz tube as reactor zone. AB was placed in a

magnetic boat, which can be dragged towards and away from furnace with an external magnet as shown in **Figure 5.1 (a)**. As AB is solid it is easy to handle and less hazardous compared to gaseous precursors. Rate of sublimation of precursor is controlled by varying distance between precursor-boat and furnace.

Before h-BN synthesis, Cu foil was annealed in H_2 (100 sccm) atmosphere for 30 min at 1020ºC. During growth H_2 was replaced with 84 sccm of Ar. AB was heated by dragging magnetic boat with precursor towards growth furnace. Temperature of precursor was examined with infrared thermometer (IRT). Growth period was around 10 min for both temperatures (90ºC and 130ºC) for the synthesis of triangular and hexagonal crystals respectively. Absorbance of h-BN on quartz substrate was measured with UV-Vis.

Under thermal treatment, AB decomposes to borazine and amino borane with production of H_2 [**Figure 5.1 (b)**] [318]. Borazine is the main building block for h-BN synthesis, which dehydrogenate on catalytic substrate to produce h-BN flake. Prior to growth Cu foil was annealed at 1020ºC in 100 sccm H_2 for 30 min. Annealing in H_2 helps to get rid of organic impurities, oxide layer and surface oxygen as well as makes surface flat with reduced roughness. During growth H_2 was replaced with 84 sccm of Ar. Magnetic boat with precursor was maintained at distance of 15 cm from furnace. Temperature of precursor increased slowly from room temperature to 90ºC observed with external IRT. After growth of 10 min, furnace was for cooled under atmospheric condition.

5.2 Results and Discussion

F**igure 5.1 (c), (d)**, and **(e)** shows OM and SEM images of as synthesized triangular

h-BN crystals. h-BN triangles are found to be almost equiangular with sharp edges with size 5~10 µm. At some places, multiple triangular crystals overlap to form polygonal structures as seen in **Figure 5.1 (d)**. For optical characterization, h-BN on Cu foil was slightly annealed at 170ºC under atmospheric condition to partially oxidize the Cu substrate. Oxidized Cu substrate helps easier identification of h-BN crystals due to its distinct pinkish contrast with an ordinary optical microscope. With growth time as long as 30 min, individual h-BN crystals merged to form the continuous film as shown in **Figure 5.1 (f)**. Some reddish patches are partially oxidized bare Cu surface.

As-synthesized continuous h-BN film on Cu was characterized with XPS. **Figure 5.2 (a)** shows binding energy values of B and N at 190.6 eV and 398.23 eV which are close to

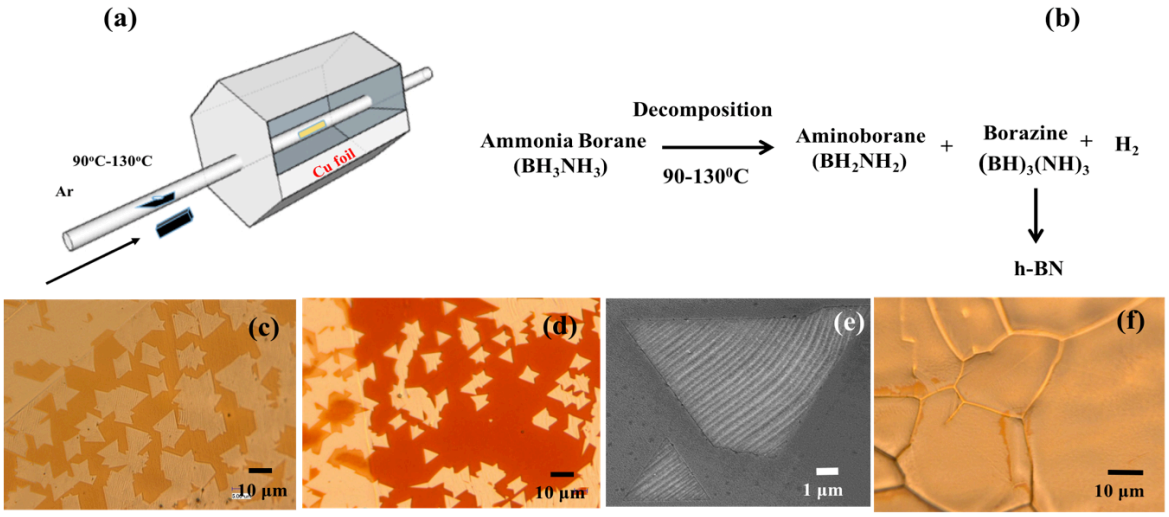

Figure 5.1. (a) Schematics of CVD system (b) Decomposition mechanism of AB. (c, d) Optical images of triangular h-BN crystal of size 5~10 µm. (e) SEM image of h-BN crystal with strips demonstrating negative thermal expansion of h-BN. (f) Continuous h-BN film synthesized with growth time around 30 min.

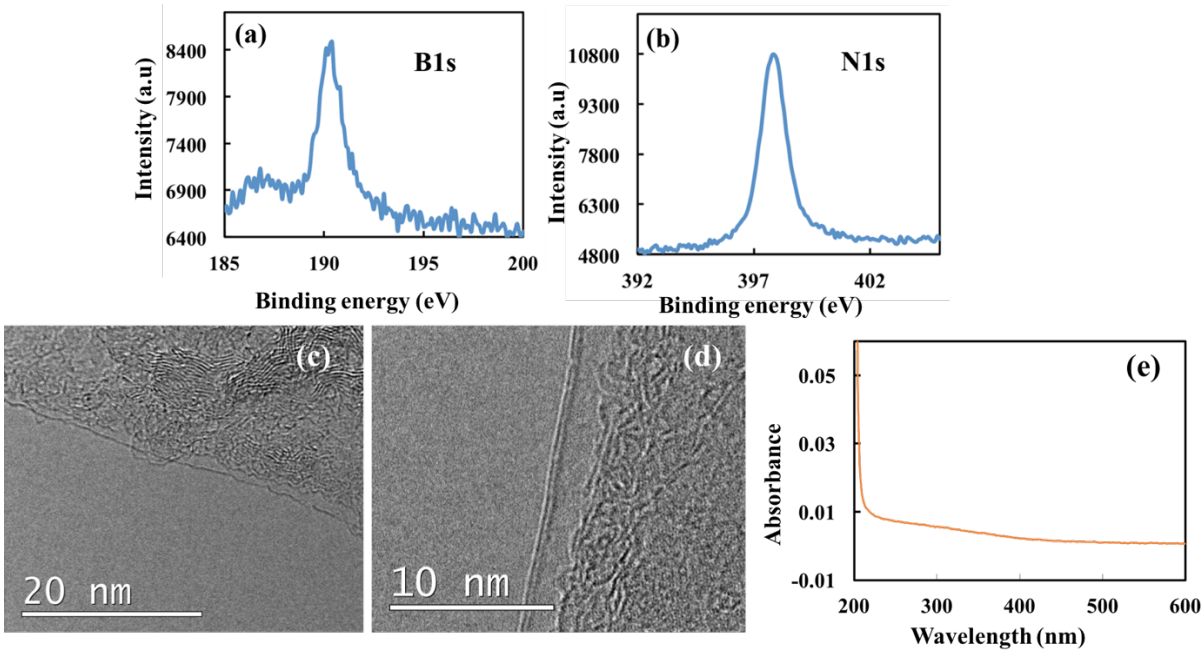

Figure 5.2. XPS spectra of (a) B and (b) N core edges at 190.6 eV and 398.2 eV respectively. TEM image showing presence of (c) monolayer and (d) bilayer h-BN film. (e) h-BN film on quartz showing negligible absorbance (less than 0.01).

reported values for h-BN. PMMA was spin coated on h-BN/Cu to transfer film to TEM grid. Cu was etched using Iron (III) Nitrate Nonahydrate ($Fe(NO_3)_3.9H_2O$) solution. As-transferred h-BN was characterized with TEM. **Figure 5.2 (a), (b)** shows the presence of monolayer and bilayer h-BN film. The h-BN film was also transferred to quartz substrate to study optical properties. Transferred h-BN film is found to be highly transparent as shown by **Figure 5.2 (e)**. In case of graphene, different experimental conditions affect growth mechanism. Parameters, such as carrier gas and its flow rate, substrate treatment, background pressure, synthesis temperatures, have found to play major role during graphene nucleation and growth. It will be also the case for h-BN growth.

Understanding the effect of these parameters, especially kinetic and thermodynamical factors, will be crucial for the synthesis of h-BN with desired attributes such as thickness and morphology and size of crystals. Growth temperature is a major thermodynamic parameter. Gas flow rate, supply rate of precursor and the constituent carrier gas are kinetic factors. In the following, effect of precursor heating temperature on morphology of crystals will be discussed. Making an analogy with CVD synthesis of graphene, h-BN synthesis on Cu involves following major steps: (1) Adsorption of BN building blocks on Cu substrate, (2) dehydrogenation of BN radicals, (3) surface diffusion, and (4) edge attachment. Beside these steps, etching of h-BN during growth is also a major phenomenon, which cannot be neglected for understanding overall crystal growth phenomenon. Since growth and etching occur simultaneously in the APCVD, crystal growth is regular attachment of atoms to the crystal edges after certain atoms are etched. Sharma et al. revealed H_2 as highly efficient etching agent of h-BN at high temperature, similar to graphene case where H_2 plays an important role in determining shape of graphene crystal by etching the weak carbon-carbon bond on crystal edges [226]. To avoid H_2 induced etching, only Ar was used as carrier gas during crystal growth in this work.

Vlassiouk et al. showed that the role of evaporating Cu on determining morphology of h-BN crystal in low pressure CVD [141]. The APCVD system was operated at low temperature (1020 ^{o}C) so that one can avoid the major Cu evaporation during h-BN synthesis. After avoiding etching of h-BN and evaporation of Cu during growth, the role of precursor temperature on crystal growth and morphology of h-BN was studied while all other experimental conditions remaining same. As demonstrated above, regular sharp edge triangular h-BN crystals was obtained with precursor heating temperature 90ºC, further designed second set of experiment in which precursor boat was placed closer (10cm) to

furnace for rapid decomposition and increased supply of borazine. Temperature around 130ºC was maintained on precursor boat. The growth was carried for 10 min and subjected to cooling.

h-BN crystals with hexagonal morphology were observed instead of triangular crystals as shown in **Figure 5.3**. Hexagonal crystals were almost same size as that of triangular. Bigger crystals along with smaller h-BN crystals have roughly adopted hexagonal morphology with irregular edge. Some h-BN crystals [**Figure 5.3 (c)** and **5.3 (d)**] showed wrinkled surface due to negative thermal expansion coefficient of h-BN. During cooling of h-BN/Cu after growth, Cu substrate shrinks whereas h-BN expands leading to formation of wrinkles. Since grain boundaries are defective sites, large number of h-BN nucleation can be observed around Cu grain boundary [**Figure 3 (c)**]. Due to chemical potential difference between B and N species, triangles are the equilibrium shapes for h-BN crystals [320]. In the present work, by maintaining high concentration of precursor in growth zone, more homogeneous crystal growth occurs leading to formation of hexagonal h-BN crystals. Tay et al. mentioned surface oxygen on Cu foil as contributing factor for hexagonal crystal [215]. In this work, presence of oxygen was avoided by high temperature annealing in H_2 atmosphere.

Further to prove the role of borazine concentration, the experiment was conducted for 10 min, in which first half part of experiment grew hexagonal crystals by high supply rate of precursor (at 130ºC) and rapidly reducing the precursor temperature (90ºC) in the remaining part of the experiment. Samples were cooled at atmospheric condition and characterized with optical microscope and SEM.

Figure 5.4 shows the modulation of hexagonal crystal under decreased supply rate of

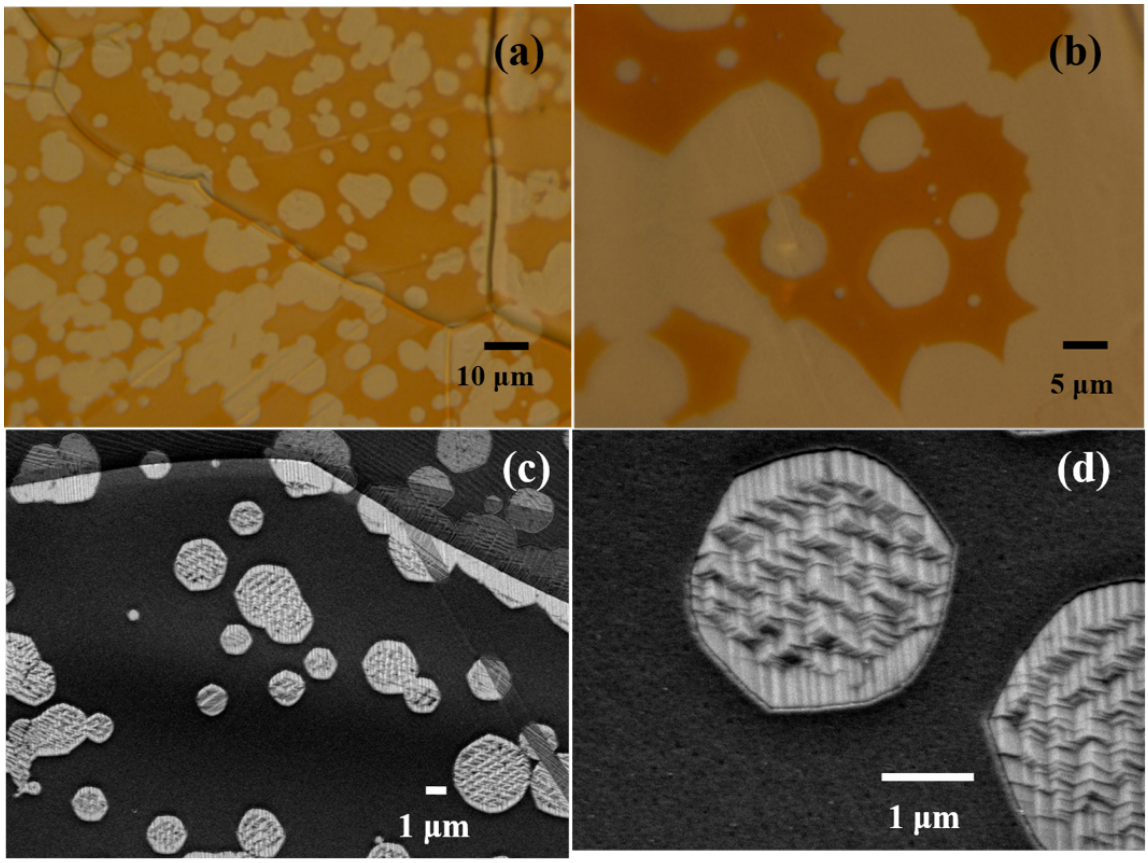

Figure 5.3. (a, b) Optical image of hexagonal shaped h-BN crystals synthesized at precursor heating temperature of 130°C. (c, d) SEM images of hexagon shaped h-BN crystal.

precursor. It is observed that under low concentration of precursor, growth dynamic is abruptly shifted from isotropic to directional. **Figure 5.4 (a)**, **(b), (c)**, and **(d)** shows crystals with unidirectional and bidirectional growth. As seen in **Figures 5.4 (h), (i), and (j)**, low precursor supply makes overall crystal growth velocity drastically reduced and crystal adopts one or two particular growth directions in other half of experiment. Interestingly, under continuous supply of low precursor (at 90ºC), double lobed h-BN crystal is transformed to triangular h-BN crystal with almost same angles (60º). **Figures 5.4 (i)** and **(j)** show the intermediate stage of transformation and almost transformed h-BN crystal to adopt triangular

morphology with clear bump feature from earlier hexagonal crystal, respectively. **Figure 5.4 (k)** presents schematics for transformation of hexagonal h-BN crystal to triangular form with different shape evolutions.

Effect of supply rate of precursor on morphology of synthesized graphene has been observed in previous reports [325]. Since all other experimental conditions remained identical in this work, it is obvious that the concentration of BN building blocks played major role in determining morphology of crystal. In the present work, triangular h-BN crystals demonstrated sharp interface synthesized under precursor heating temperature (90ºC)

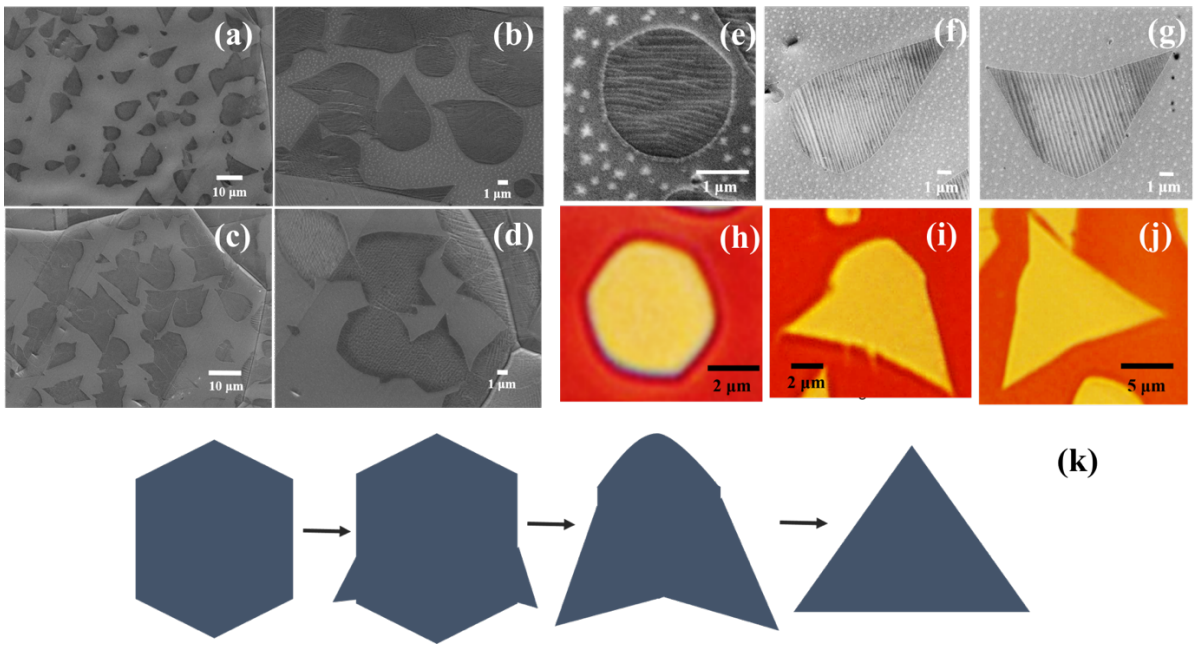

Figure 5.4. (a, b, c, d) Evolution of single lobed and bilobed structures from hexagon shaped h-BN crystal. Close up view of (e) hexagonal crystal, (f) single and (g) bilobed crystal. (h) Optical image of hexagonal crystal and its modulation to (i) intermediate state and almost (j) modulated triangle, showing little bump. k) Schematics representing growth zone.

transformation of hexagonal crystal to triangular with decreased supply of borazine to whereas hexagonal crystals had irregular and curved vertices. Crystals with straight edges in zigzag direction were synthesized when edge attachment is the limiting factor for crystal growth [317]. In addition, irregular edges would be attributed to growth mechanism where diffusion is rate-limiting factor [123, 322]. With knowledge of graphene synthesis process on Cu substrate, formation of triangular, hexagonal crystals and transformation of hexagonal to triangular crystal can be explained as follows. Triangles with zigzag edges are equilibrium shape for h-BN crystal under low supply of precursor due to edge attachment as the rate-

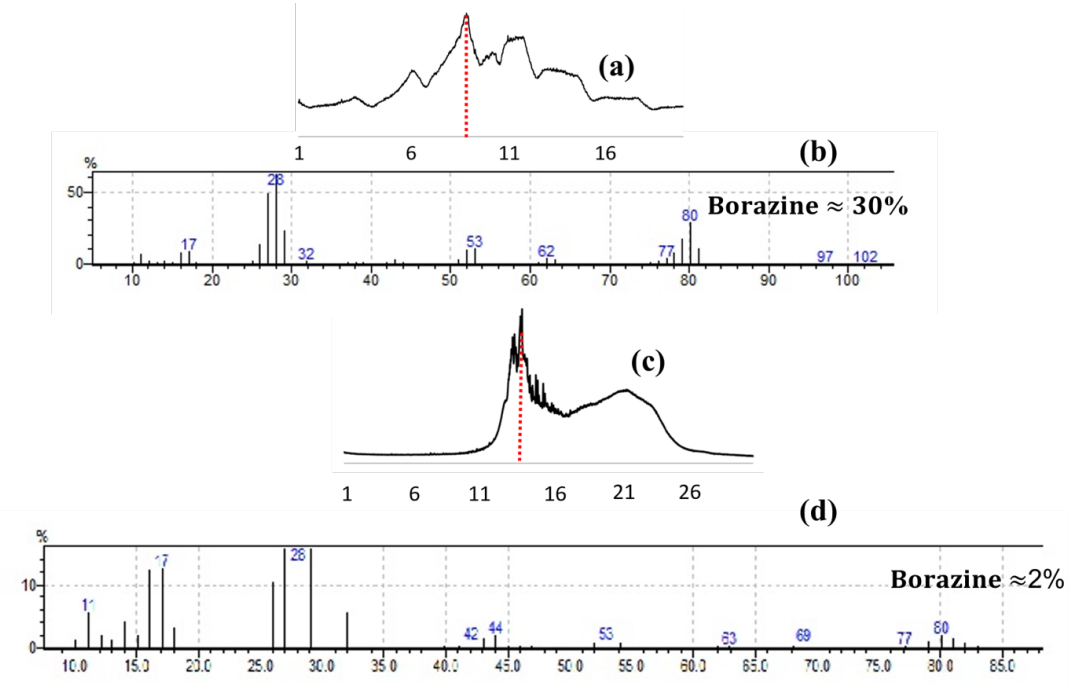

Figure 5.5. (a) EGA thermogram of AB heated at 130^{0}C showing maximum decomposition around 9th min. (b) Mass spectra complied at 9th min, showing relative abundance of borazine around 30%. (c) EGA thermogram of AB heated at 90ºC showing maximum decomposition around 13.5th min (d) Mass spectra complied at 13.5th min, showing relative abundance of borazine around 2%.

limiting phenomenon. During high concentration supply of BN radicals, kinetics at edge would be changed, with diffusion becoming rate-limiting phenomenon for crystal growth. Increased diffusion and availability of free B and N radicals makes crystal growth favorable on both B and N terminated edges for maintaining hexagonal morphology. In fact, h-BN synthesis under LPCVD, edges of h-BN crystal is known to be modulated from straight edges to curved morphology by heating AB at different temperatures [332]. In the present investigation, it was achieved by tuning the growth mechanism from edge attachment limited to diffusion limited by drastic reduction in supply of BN building blocks hence modulating crystal morphology.

To further analyze volumetric evolution of Borazine at different temperature, evolved gas analysis (EGA) followed by gas chromatography was done for the decomposition of AB at 90 and 130ºC under Ar atmosphere. **Figure 5.5 (a)**, shows EGA spectra of AB decomposition at 130ºC where the highest volume of gases is evolved around 9^{th} min. **Figure 5.5 (b)** presents mass spectra complied at 9^{th} min showing relative abundance of main building block borazine (atomic mass 80.5) around 30%. Similarly, **Figure 5.5 (c)** shows the decomposition of AB at 90ºC with main evolution of gas mainly around 13.5^{th} min. Follow up mass spectra was compiled at 13.5^{th} min as shown in **Figure 5.5 (d)**. Relative abundance of borazine was found to be around 2%. Thus, it can be concluded that with changing in precursor heating temperature, borazine concentration can be varied significantly, leading to different growth mechanism of h-BN crystals.

5.3 Conclusions

In summary, it was successfully adopted a method to synthesis of triangular and hexagonal shaped h-BN by APCVD. The synthesized method was highly controllable with

the transformation of hexagonal shape to triangular by controlling heating temperature of AB. The different modes of crystal growth were attributed to the concentration of BN building block in growth region as proved by EGA and gas chromatography analysis. This work would be promising as milestone for synthesis of h-BN crystals with variety of morphologies with different edge related electronic, magnetic and catalytic properties.

Chapter 6

Edge Controlled Growth of Hexagonal Boron Nitride Crystals on Copper Foil by Atmospheric Pressure Chemical Vapor Deposition

6.0 Introduction

In the previous chapter, it was demonstrated that AB pyrolysis in a wide range of temperature (90 to 130 ^{o}C) resulted in triangular and hexagonal h-BN crystals formation. The synthesized triangular crystals size was around 5~10 μm in edge length. Previous chapters clearly show the CVD synthesized h-BN crystals were more than 10 times smaller than graphene crystals. This is the clear indication of complexity in crystals growth mechanism of h-BN than graphene. The binary elements N and B should properly sp^2 hybridize for h-BN crystals. The CVD method is widely adopted in order to investigate complex growth mechanism as well as the synthesis of wafer-scale thin films and also h-BN domains [175, 213-229]. Thus, much effort has been devoted to synthesize the larger domain size h-BN [216, 217, 228, 229]. However, the achieved size is still as small as ~20 μm in edge length by APCVD [214]. From a simple geometric consideration, the number of crystal consisting atoms increases with an increase of crystal size in proportional to the square of edge length of the crystal. This implies that the amount of source atoms for the crystal growth should be increased properly to keep the growth rate proper and to not terminate the growth.

Nevertheless, this has not yet been attempted for the h-BN growth, maybe due to the difficulty in controlling the decomposition rate of AB. In what follows, in order to achieve the larger domain size h-BN growth, the controllable increase in the supply of B-N molecular species have been challenged by stepwise decomposition of AB in APCVD for the first time.

6.1 Experimental Methods

Figure 6.1 (a) shows a schematic representation of the APCVD system employed in this chapter. A solid source AB (H_3BNH_3) with B and N atoms in 1:1 stoichiometric ratio was used as a precursor. Cu foil, 2x4 cm^2 in size and 20 μm in thickness (Nilaco corporation), was used for substrates. For APCVD, 2-inch diameter horizontal tubular furnace was employed. A typical example of the change in furnace temperature is shown in **Figure 6.1 (b)**. 100 sccm Ar was introduced for 5 min before heating the furnace to make sure of an inert environment and then, the furnace was ramped at an average rate of 10.5 ^oC/min from room temperature to 1050 ^oC to pre-anneal the Cu substrate. Prior to the h-BN growth, Cu was annealed at 1050 ^oC for 30 min by introducing 17 sccm of H_2 mixed with 100 sccm Ar. Then, the H_2 gas flow rate was switched to 2 sccm mixed with 100 sccm Ar for the individual crystal growth of h-BN. After the h-BN growth, the sample was cooled down to room temperature rapidly without changing gas composition.

12 mg of AB, which was kept in magnetic boat [see **Figure 6.1 (c)** inset], was heated to the required temperatures monitored with an external IRT. The temperature of the AB loaded boat was controlled by the distance from the 1050 ^oC heated furnace. At the elevated temperatures, AB thermally decomposed into aminoborane (BH_2NH_2, solid), H_2 and borazine ($(HBNH)_3$, gas), and further pyrolysized borazine resulted in the h-BN on Cu [213, 317]. The decomposition temperature range of 60-85 ^oC of AB was sufficient to produce h-BN in

developed APCVD system. Two different methods, namely, (i) stepwise and (ii) constant decomposition of AB, were employed. In the stepwise decomposition, the increment step was set to be 5 ^{o}C in the temperature range of 65-80 ^{o}C [see **Figure 6.1 (c)**], namely, decomposition temperature increased at 4 steps in 65-80 ^{o}C. For the h-BN growth duration of 38, 50, 62, and 72 min (referred to Methods A, B, C and D, respectively, hereafter), the decomposition temperature of AB was kept at the respective step temperatures for 9, 12, 15 and 17.5 min, respectively [see **Figures 6.1 (b)** and **6.1 (c)**]. By contrast, in the experiment of the constant decomposition of AB, the decomposition temperature of AB was kept constant at 70 or 75 ^{o}C (referred to Methods E and F, respectively, hereafter).

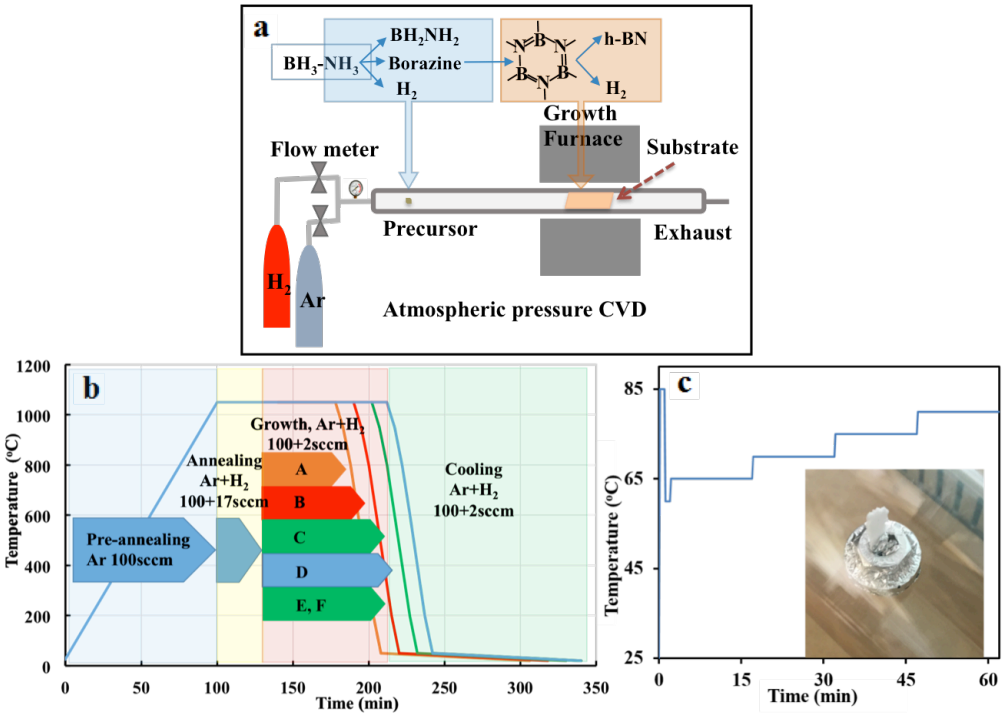

Figure 6.1. (a) Schematic illustration of the APCVD system with molecular decomposition in respective zone, (b) temperatures profile diagram of the furnace (with growth Methods A-F), (c) an example of temperature profile for heating AB for the growth time of 62 min (Method C; 15 min/step at 65-80 ^{o}C), and inset showing AB kept in magnetic boat.

For the transfer of the synthesized h-BN film and crystals onto SiO_2 (300 nm)/Si and TEM grids, PMMA assisted delamination [251] technique was adopted. Briefly, 4000 rpm for 1 min spin coated PMMA layer on the sample was cured in a hot oven at 80 ^oC for 5 min and then electrochemical delamination was done with 0.1N NaOH solution. PMMA assisted film was rinsed in deionized water several times to be transferred onto the desired substrate, and then the PMMA was removed by hot acetone.

6.2 Results and Discussion

Figure 6.2 shows OM images of as-synthesized h-BN crystals obtained with various AB heating durations. Individual h-BN crystals were distinctly recognizable due to the environmental oxidation of Cu at 200 ^oC and oxidative resistant of h-BN. **Figure 6.2 (a)** shows sparsely distributed regular triangular h-BN crystals of average domain size >10 μm obtained for the shortest growth time (38 min; Method A). With increasing the growth time, h-BN crystals of larger domains with preserved domain morphology grew, as shown in **Figures 6.2 (b)** and **2 (c)**. For the longest growth time (62 min; Method C), regular triangular shaped crystals of domains larger than 25 mm in edge length was obtained [see red arrow-indicated in **(d)**]. **Figure 6.2(C)** shows that h-BN crystals almost merged to form continuous film with bare Cu observed at only few places. On further increasing the growth time by 10 min (Method D) a fully covered continuous h-BN film was obtained. Minimization of crystal nucleation points is highly desirable during CVD synthesis of h-BN, so that high quality film can be synthesized with few grain boundaries.

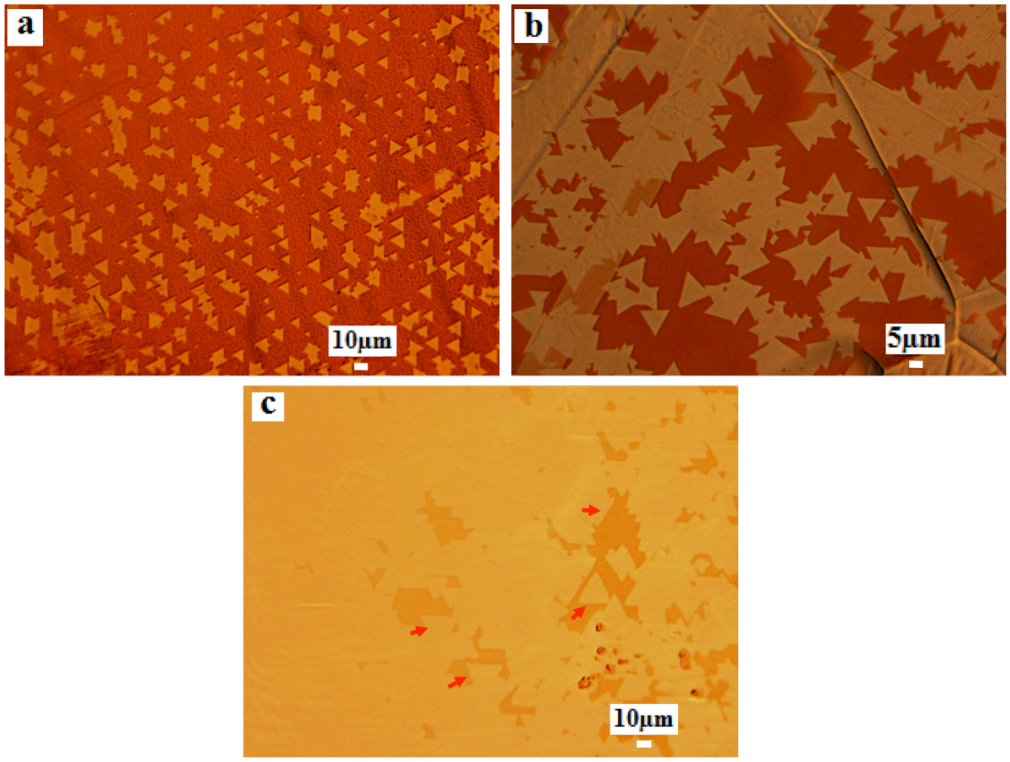

Figure 6.2. Optical microscope images of h-BN crystals grown for (a) 38 min (Method A; 9 min/step), (b) 50 min (Method B; 12 min/step) and (c) 62 min (Method C; 15 min/step). Arrows in (c), see text.

For a comparison, synthesis at constant AB heating temperatures was also carried out with other parameters maintained unchanged. **Figures 6.3 (a)** and **6.3 (b)** show OM images of as synthesized h-BN crystals for 62 min at 70 and 75 ^{o}C (Methods E and F), respectively. It should be noted that h-BN crystal shape strongly depends on the decomposition condition of AB: The crystal shape was regular triangular with sharp edges for the stepwise decomposition of AB, while it was truncated triangles and round shaped [see magnified AFM images in **Figure 6.7(c)** and **(d)**] for constant decomposition of AB at 70 and 75 ^{o}C, respectively, as summarized in **Figure 6.3 (c)** together with possible atomic arrangements of B and N in **Figure 6.3 (d)**. The evolution of regular triangular shape might be attributed to atomistic growth mechanism with N-rich zigzag and combination of B and N-rich armchair termination for straight and truncated part of triangles, respectively [320, 325]. By stepwise

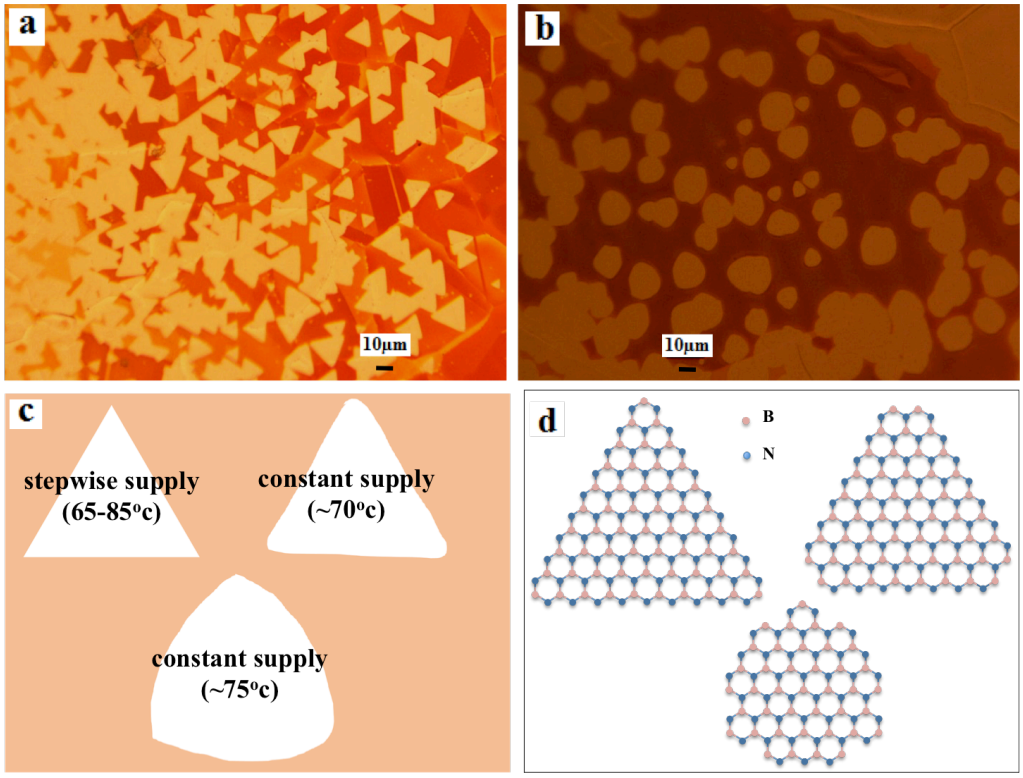

Figure 6.3. OM images of h-BN crystals obtained after the growth for 62 min at constant AB decomposition temperature at (a) 70 °C (Method D), and (b) 75 °C (Method E). (c) Schematic representation of observed crystal shapes and (d) corresponding atomic arrangements of B and N.

decomposition, geometrical demands of borazine quantity was believed to be supplied in every succeeding step, similar to the case of graphene growth [118, 319, 326]. With increase in decomposition temperature, many fold increase in quantity of borazine was reported in past work [317]. Hence increase in AB decomposition temperature during growth can be essential for preserving or accelerating crystal growth velocity. Hereafter the key aspects of h-BN growth in APCVD by stepwise growth technique will be discussed.

XPS analyses has been carried out to check the stoichiometry of different shaped h-

BN flakes synthesized on Cu by the methods C (perfect triangles), E (truncated triangles) and F (reuleaux triangles) as shown in **Figure 6.4**. XPS analysis was performed on the sample containing more than one crystal with similar shape by using 20 µm spot size of x-Ray. The h-BN characteristic peaks were confirmed at ~190.3 and ~397.7 eV for all types of samples, corresponding to B1s and N1s, respectively [**Figure 6.4(a) and 6.4(b)**]. The stoichiometry of the three h-BN samples with different edge structures was investigated from the highlighted peak areas. It was observed almost no difference in calculated atomic percent of B and N within the experimental error [inset of **Figure 6.4(a) and (b)**]. The reason would be as follows: For the atomic models shown in **Figure 6.3(d)**, the numbers of respective (N and B) atoms and atomic ratios for the respective shapes are as listed in **Table 6.1**. The sizes of those

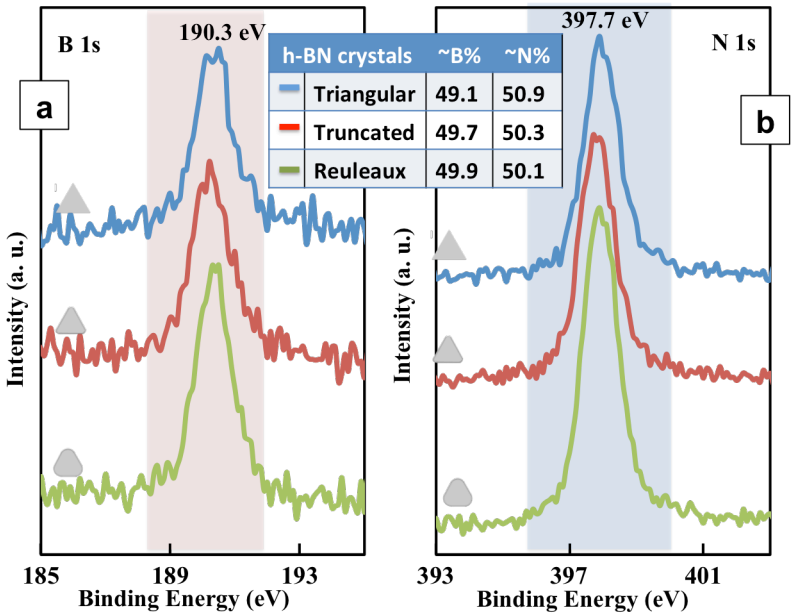

Figure 6.4. Characterization of h-BN. (a) B1s and (b) N1s XPS spectra of the h-BN crystals synthesized with Method C, E and F by blue, green and red colors, respectively. Inset shows the atomic percentage calculated from integral intensity peaks. XPS observation was performed using 20 µm spot size of x-Ray.

crystals are about 4 nm on edge length (calculated for 9 N atoms on edge with lattice constant for unit cell a= 2.504 Å [324]). Apparently, with increasing the crystal size, the atomic ratio of N to B decreases towards unity independent of the crystals shape. As shown in Figure 6.2(c), 6.3(a) and 6.3(b) the synthesized crystals were around 25 μm in size, thus the difference in atomic ratio of N to B should have been too small to be detected by XPS.

Table 6.1. Atomic ratio of N to B based on the atomic model of Figure 5.3 (d).

h-BN crystals shapes	atomic model [Figure 3(d)]	
	Ratio (N to B)	Counted
Perfect triangle	1.145	63 (N), 55 (B)
Truncated triangle	1.096	57 (N), 52 (B)
Reuleaux triangle	1.05	42 (N), 40 (B)

Figure 6.5(a) shows typical Raman spectra of the h-BN crystal, which was grown with the stepwise supply of AB for 38 min (Method A) and then transferred onto SiO_2/Si. A peak at 1373 cm^{-1} corresponds to E_{2g} vibration mode of monolayer sp^2 hybridized B-N bond stitching [200, 223]. The crystallinity of synthesized h-BN by method D was investigated by TEM. Low-magnification TEM image [**Figure 6.5(b)**] shows that h-BN mostly comprised of the continuous film. Residual Cu particles [red arrow-indicated in **(b)**] and fragility of h-BN at the folded edge in **Figure 6.5(b)** would occur due to the transfer process. **Figure 6.5(c)** and **6.5(d)** show the magnified TEM images on the edge of the film shown in **Figure 6.5(b)**, confirming that the synthesized film comprised of dominantly monolayer and bilayer h-BN at the folded edge. Interlayer distance was found to be around 0.35 nm close to the reported [175] values [**Figure 6.5(d)**]. Inset of **Figure 6.5(c)** shows six fold symmetric selected area

diffraction (SAED) pattern taken over continuous film at red circle area of **Figure 6.5(b)** showing high crystallinity.

Figure 6.6 shows SEM and corresponding EBSD images of the h-BN on Cu synthesized with Method A. As see in **Figure 6.6 (b)**, the h-BN crystals were characterized by dark contrast polygons with various size and orientation. The most of the polygons were triangular, and it should be noted that several triangular crystals grow across the grain boundary of Cu with keeping the triangular shape. In order to investigate the influence of the

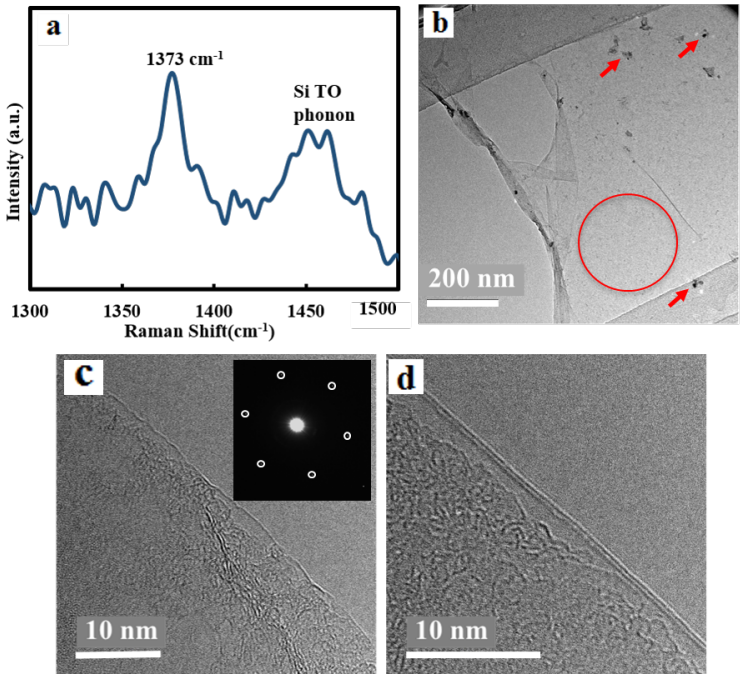

Figure 6.5. Characterization of h-BN. (a) Raman spectra of h-BN crystals (synthesized with Method A) on SiO_2/Si with characteristic peak position at 1373 cm^{-1} with FWHM ~14 cm^{-1}. (b) Low and (c, d) high magnification TEM images of the suspended h-BN film (Method D) on a holy carbon net. Inset shows typical diffraction pattern taken at red circle of 6.5(b).

crystallographic orientation of catalyst grains, EBSD mapping of the region corresponding to **Figure 6.6 (b)** was carried out [**Figure 6.6 (a)**]. As typically shown by red ellipses in **Figure 6.6 (b)**, h-BN crystals differed in shape and edge direction even on a single Cu grain, suggesting that h-BN crystal shape was not influenced strictly by the Cu orientation. However, h-BN triangular crystals differed in edge orientation by 0^{o}, 30^{o}, 60^{o} and 90^{o} (isolated h-BN crystals) on Cu (001) grains as shown in **Figure 6(b)** which is in agreement

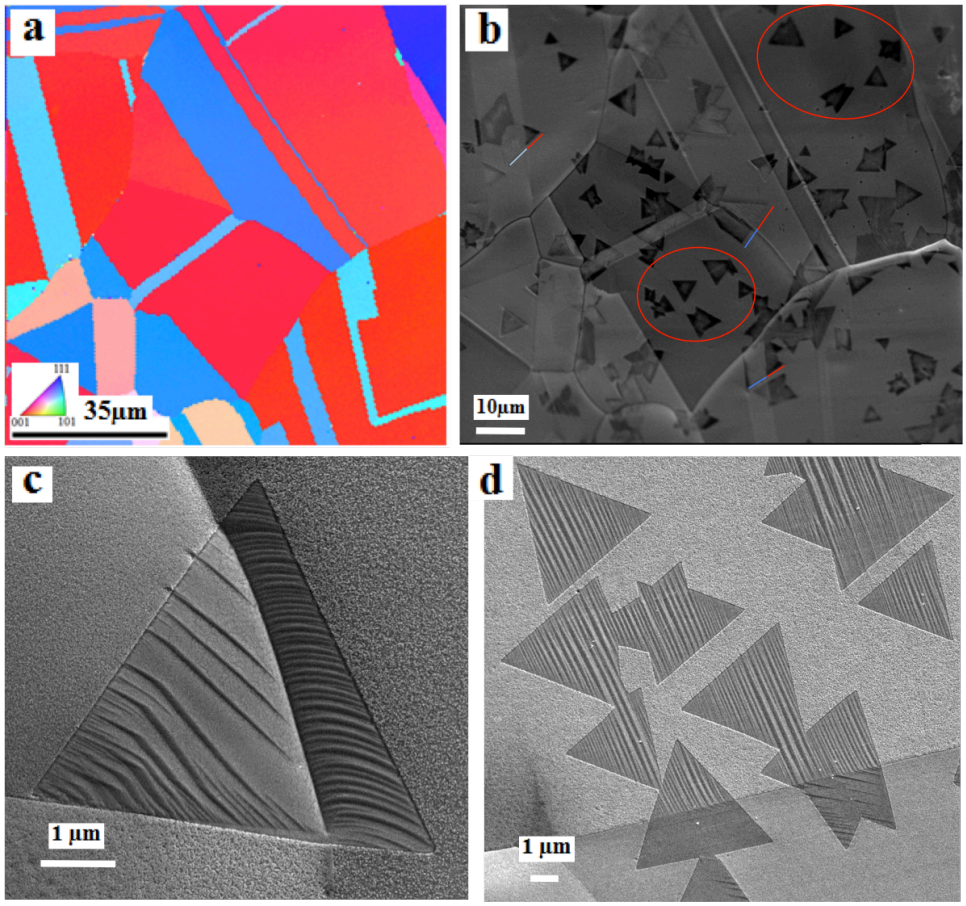

Figure 6.6. EBSD mapping with color key inset and (b) corresponding SEM image of the h-BN on Cu synthesized with Method A (stepwise growth for 38min). (c, d) Enlarged SEM images of typical (c) h-BN single crystal grown across Cu grains and (d) h-BN crystals with wrinkles well-aligned over several h-BN crystals on a single Cu grain.

with Song et al. [216]. Magnified SEM images, **Figure 6.6 (c)** and **6.6 (d)**, show typical examples of wrinkled h-BN on Cu grains. The parallel wrinkles aligned in a certain direction independent of the shape and orientation of h-BN crystals on a single Cu grain as shown in **Figure 6.6 (d)**. By contrast, as seen in **Figure 6.6 (c)**, the aligned direction of the wrinkles changed abruptly across the Cu grain boundary, although h-BN edge symmetry unaltered at all.

In order to obtain the quantitative information of the height of the wrinkles, AFM analysis was performed. **Figure 6.7 (a)** shows an AFM image of another example of the same sample as in **Figure 6.6**, disclosing the several triangular shaped h-BN crystals with aligned wrinkles grow on a single Cu grain. **Figure 6.7 (b)** shows an AFM line profile of the wrinkle attained along the arrow shown in **Figure 6.7 (a)**, revealing that the aligned h-BN wrinkle was sinusoidal-like with maximum 20 nm in heights and about 0.25 μm in wavelength. Line profile clearly shows that wavelength and height of h-BN wrinkles continuously increases from edge towards the center of crystal. This phenomenon was previously reported for graphene wrinkles [327] with no report on h-BN up to now. Nevertheless, after the transfer onto SiO_2/Si, h-BN was quite smooth without any wrinkles, as shown in **Figure 6.7 (c)**. AFM images **Figure 6.7(d)** and **6.7 (e)** show the h-BN crystal synthesized by method E and F respectively with truncated and reuleaux shaped morphology with aligned wrinkles similar to **Figure 6.7 (a)**. Variation in wrinkles alignment occurred with preserved edge orientation for reuleaux shaped h-BN crystal [**Figure 6.7 (e)**] as observed in **Figure 6.6 (c)** and **(d)**.

It was expected that with the growth of perfect triangle, a seamless continuous film can be obtained with less grain boundary and better electronic property. The h-BN film with less grain boundary can be significant for application as dielectric insulting layer in graphene

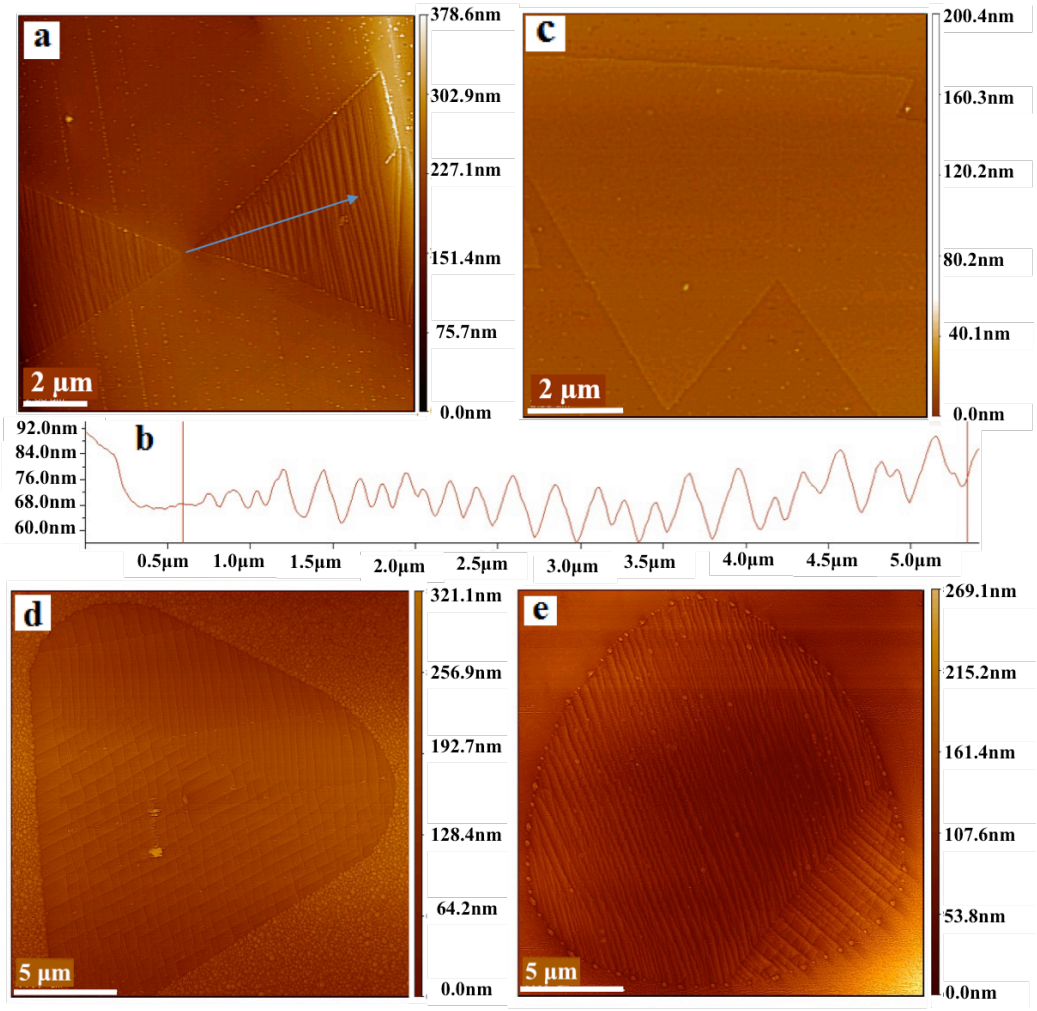

Figure 6.7. (a) AFM images of h-BN grown on Cu synthesized by method A. (b) AFM line profile measured along a blue arrow in Figure 6.7 (a). (c) AFM images of h-BN transfered onto SiO_2/Si. h-BN was synthesized with Method A. AFM images of h-BN grown on Cu synthesized by (d) method E and (e) method F.

and other two dimensional layered electronic devices. Graphene edges depending on different morphologies highly influence the electronic, magnetic properties and its chemical reactivity [328, 329]. Making an analogy to graphene, it is believed h-BN crystals with various morphologies such as truncated or reuleaux triangular can be attractive as they might offer various catalytic and edge related properties making their controlled growth highly desirable.

6.3 Conclusions

In summary, the edge controlled growth of h-BN crystals from regular to truncated triangles and round shapes have been explored by controlling the decomposition of AB in APCVD. The stepwise decomposition of AB rendered the regular triangular monolayer h-BN crystals with edge length of larger than 25 μm on Cu substrates, thus indicating the importance of partial pressure of precursor molecules for h-BN growth. Aligned wrinkles larger than 20nm formed on Cu due to the thermal strain of Cu surface and a negative expansion coefficient of h-BN. Nevertheless the h-BN transferred onto SiO_2/Si substrates was quite smooth without any wrinkles. Thus, it is believed that the stepwise decomposition technique is promising for the growth of the high quality and large domain size h-BN, which will be utilized as a platform for the further stacking of other 2D materials.

Chapter 7

Conclusions & Future Works

7.0 Overall conclusions

This thesis has demonstrated the CVD synthesis and characterization of graphene and h-BN crystals with detailed insight into control over two major factors: enhanced Cu catalytic property via thermal treatment, timely supplied precursor molecules to fulfill the geometrical demands of crystal growth at the graphene and h-BN basal planes via step-wise pyrolysis of PS and AB. The importance of larger graphene and h-BN crystals with almost identical growth condition is highly desirable to overcome the challenging issues for the single step synthesis of graphene and h-BN hetero-structures with graphene on h-BN or vice-versa. This thesis presented highly convincing graphene and h-BN synthesis approach as presented in previous chapters, which further ascertained the CVD emergence as of scalable approach. This thesis solely focused on understanding of graphene and h-BN growth kinetics and their characterization approach, and hence the materials implication into device performance is desirably expected as a future work. Because of single crystals synthetic approach, it can be believe that the devices fabricated by utilizing synthesized materials or materials produced by employing synthesis technique will overcomes various shortcomings of materials of other technique. This chapter will summarize major findings of high crystalline quality of graphene and h-BN crystals by optimizing numerous CVD parameters.

The influence of Cu foil crystalline structure on as-synthesized graphene crystals and their anisotropic etching process was studied. The highest nucleation density and etching rate was achieved on Cu (111) which due to its lowest surface energy than Cu (001) to Cu (110). The lattice parameters of FCC crystals for {111}, {001} and {110} planes are 0.577, 0.666 and 0.707 respectively and found their effects on growth and etching rates within closure vicinity of respective planes. The lattice parameters highly influence the strips and wrinkles alignment in synthesized graphene crystals and their anisotropic etching as well. However, hexagonal holes formed due to anisotropic etching were independent to strips and wrinkles alignments in graphene. The growth nature of graphene investigated in Chapter 3 through LPCVD synthesis technique was crucial to understand the growth mechanism and to optimize the CVD parameters for lager graphene domains.

Electroless polishing of Cu was done to remove native oxides and rolling lines, and further annealed at 1050 ^{o}C for subsequent recrystallization with predominance of Cu (111). Ar and H_2 environment annealing of Cu significantly influence the grain transformation thereby obtained a smother Cu surface with reducing nucleation density. On step-wisely supplying the precursor molecules on processed Cu, single graphene crystals larger than 560 μm were obtained. Either by using different gas composition or by using different annealing duration and speed, other facet terminated mono crystalline Cu surface may achieved. The precursor supplying technique was most effective over predominantly Cu (111) to synthesize larger crystals. Optical microscopy and Raman analysis showed the presence of monolayer graphene domain; however, few-layer individual domain was also observed depending on the absorbed carbon atoms on Cu surface. Similarly, the hexagonal- and circular- morphologies of graphene crystals on a substrate form single experiment were observed and symbolically indicated the crucial growth mechanism.

Controlled decomposition of PS was achieved for elapsed graphene crystals growth due to the chosen temperature range (165 - 175 °C), which was far below than the melting point (240 °C) of PS. For h-BN growth, AB was heated at 90 °C (below the melting point), 130 °C (higher than melting point) and form 130 to 90 °C in separate sets of experiments. Triangular and hexagonal crystals synthesized for respective temperatures of 90 °C and 130 °C, and the crystals morphology modulation occurred for combination of both. In this way a fully precursor supplied technique controlled h-BN crystals growth was achieved. The different modes of crystal growth were attributed to the concentration of BN building block in growth region as proved by EGA and gas chromatography analysis.

For pyrolysis of AB closure to melting point, rapidly decomposed into amino borane and borazine. The excess amount of borazine at a time resulted into continuous h-BN film few micron grins size due to catalytic limitation of Cu for excess supply. The controlled partial pressure of precursor molecules achieved with the pyrolysis of AB far below the melting temperature based on the result observed in chapter 5. However, the processing technique of crystals growth were terminate around 10 min with domain size around 5 to 10 μm, otherwise synthesized h-BN resulted into continuous film. Based on the experience of large graphene crystals case, AB heated step-wisely in a temperature range of 65-85^{o}C. With the elapsed growth time of 62 min large single crystal h-BN was synthesized with edge length of 25 μm. Aligned wrinkles larger than 20nm were also observed on h-BN due to the thermal strain of Cu surface and a negative expansion coefficient of h-BN. Synthesized materials were characterized by Raman, TEM, XPS which showed higher crystalline material quality.

7.1 Recommendation for Future Works

For the next generation nano-electronics, graphene and h-BN are intensively studied and sought as promising materials. Technological potential could be achieved with 2D system by using high quality and large area graphene and h-BN films synthesized via CVD methods. Despite the many interesting results presented in this thesis, the following additional works could be done in near future.

Solid precursors were advantageous in the environment friendly issues and offered ease in manipulation than liquid and gas precursors. Vapors of precursors were generated by instant pyrolysis of AB and PS inside the reactor zone. The issues of homogeneously mixing of precursor molecules with carrier gases could be solved by external pyrolysis chamber to ease the growth process. Furthermore rapidly heating and cooling of substrate could be done to modify the substrate crystalline structures and make shorter the CVD processing time. A modified precursor feeding system can be developed to make localized growth process of graphene and h-BN crystals. The catalytic activity of Cu closure its melting point found to be most effective, so low temperatures melting metals can be used to lower the processing temperatures. Catalytic activities of Cu further make effective at low temperatures (below 400^{o}C) either by Cu chlorination process, or by composite alloys with techniques such as Cu-Al, Cu-Ga.

Graphene and h-BN nano ribbon extensively investigated for the band gap issues (tunable band gap in graphene nano ribbon and reducible band gap in h-BN nano ribbon). The plasma etching process of the surfaces could be employed on the well aligned graphene and h-BN wrinkles leaving behind aligned graphene and h-BN nano ribbon on Cu. Well aligned nano ribbons are highly desirable in nano electronics.

PMMA transferred based hetero-structures were intensively explored. However, the residual polymer left behind hinders the electronic performance. The single batch hetero-structure synthesis of graphene and h-BN and with other 2D materials is highly desirable. Most specifically, single batch synthesis of graphene and other 2D materials on h-BN (if could possible) is most promising for extended device performance. The optimized condition for the growth of graphene and h-BN crystals with various edge orientations offers suitable single batch synthesis route. The step-wisely pyrolysis technique employed for the AB and PS can switch into one another during single batch synthesis process for the synthesis of graphene and h-BN lateral hetero-structures. The precursor controlling technique further employed for other 2D materials (MoS_2, WS_2, $MoSe_2$, WSe_2, etc.) for their larger domain synthesis purpose. Hetero-structures of two or more 2D materials synthesized in single batch CVD process could be most promising materials in nano electronics.

List of Publications used for the Thesis

1. **Kamal P. Sharma**, Sachin M. Shinde, Mohamad Saufi Rosmi, Subash Sharma, Golap Kalita, Masaki Tanemura, Effect of copper foil annealing process on large graphene domain growth by solid source-based chemical vapor deposition**.** Journal of Materials Science 51, 7220 (2016), **Chapter 4**.

2. Subash Sharma, **Kamal P. Sharma,** Mohamad S. Rosmi, Yazid Yaakob, Mona I. Araby, Hajime Ohtani, Golap Kalita, and Masaki Tanemura, Morphology-Controlled Synthesis of Hexagonal Boron Nitride Crystals by Chemical Vapor Deposition. **Crystal Growth Design**, 16 (11), 6440 (2016), **Chapter 5**.

3. **Kamal P. Sharma**, Rakesh D. Mahyavanshi, Golap Kalita, Masaki Tanemura, Influence of copper foil polycrystalline structure on graphene anisotropic etching. **Applied Surface Science** 393, 428 (2017), **Chapter 3.**

4. **Kamal P. Sharma**, Subash Sharma, Aliza K. Sharma, Balaram Paudel Jaishi, Golap Kalita, Masaki Tanemura**,** Edge Controlled Growth of Hexagonal Boron Nitride Crystals on Copper Foil by Atmospheric Pressure Chemical Vapor Deposition. ***CrystEngComm*****,** 20, 550 – 555 (2018), **Chapter 6.**

List of Co-authored Publications

1. Amutha Thangaraja, Sachin M. Shinde, Golap Kalita, Remi Papon, Subash Sharma, Ritesh kumar Vishwakarma, **Kamal P. Sharma** and Masaki Tanemura, Structure dependent hydrogen induced etching features of graphene crystals. **Applied Physics Letters** 106, 253106 (2015).

2. Ritesh K. Vishwakarma, Subash Sharma, Sachin shinde, **Kamal Sharma**, Amutha Thangaraja, Golap Kalita and Masaki Tanemura, Fabrication of particular structures of hexagonal boron nitride and boron-carbon- nitrogen layers by anisotropic etching. **physica e low-dimensional systems and nanostructures** (10.1016/j.physe.2015.12.004).

3. Mohamad Saufi Rosmi, Sachin M. Shindei, Nor Dalila A. Rahman, Amutha Thangaraja, Subash Sharma, **Kamal P. Sharma**, Yazit Yaakkob, Ritesh K. Vishwakarma, Suruyani Abu Bakar, Golap Kalita, Hajime Ohtani, Masaki Tanemura, Synthesis of high quality monolayer graphene from waste chicken fat by low pressure chemical vapor deposition (LPCVD). **Materials Research Bulletin** 83, 573 (2016).

4. Remi Papon, **Kamal P. Sharma**, Rakesh D. Mahayavanshi, Subash Sharma, Ritesh K. Vishwakarma, Mohamad S. Rosmi, Toshio Kawahara, Joseph Cline, Golap Kalita, Masaki Tanemura, CuNi binary alloy catalyst for growth of nitrogen-doped graphene by low pressure chemical vapor deposition. **Rapid Research Letter** 10, (10), 749 (2016).

5. Rakesh D. Mahyavanshi, Golap Kalita, **Kamal P. Sharma**, Masaharu Kondo, Dewa Takeshita, Toshio Kawahara, Masaki Tanemura, Synthesis of MoS2 ribbons and their

branched structures by chemical vapor deposition in sulfur enriched environment. **Applied Surface Science** 409, 396 (2017).

6. Subash Sharma, Balaram Paudel Jaishi, **Kamal P. Sharma,** Mona Ibharim, Golap Kalita, Masaki Tanemura, Synthesis of freestanding WS2 trees and fibers on Au by chemical vapor deposition (CVD), **physica status solidi (a)**, (2017).

List of Conferences

1. **Kamal P. Sharma**, Golap Kalita and Masaki Tanemura**.** In-situ oxygen evolution from substrate holder for large area graphene crystal growth in an atmospheric pressure CVD (Oral), **The 76th Japan society of applied physics (JSAP) autumn meeting**, 15th September, 2015, Nagoya, Japan

2. **Kamal P. Sharma**, Subash Sharma, Golap Kalita and Masaki Tanemura. Effect of Copper foil annealing process on large area graphene crystal growth by atmospheric pressure chemical vapor deposition (Poster), **The 28th International Microprocesses and Nanotechnology (MNC)** Conference 2015, Toyama, Japan

3. **Kamal Prasad Sharma**, Subash Sharma, Golap Kalita, Masaki Tanemura**.** Role Of Copper Substrate Annealing On Graphene Crystal Synthesis By Atmospheric Pressure Chemical Vapor Deposition (Oral), **The 11th IEEE International Conference on Nano/Micro Engineered and Molecular Systems (IEEE NEMS)** 17th, April 2016, Sendai, Japan

4. **Kamal P. Sharma**, Golap Kalita, Masaki Tanemura**.** Influence of Cu crystallographic orientations on graphene anisotropic etching (Oral), **The 63rd Japan society of applied physics (JSAP) Spring meeting**, 19th March, 2016, Tokyo, Japan

5. **Kamal P. Sharma**, Golap Kalita, Masaki Tanemura. Influence of Copper Crystallo-graphic orientation on Growth and Etching of graphene (Oral), **The 29th International Microprocesses and Nanotechnology (MNC) Conference** 2016, Kyoto, Japan

6. **Kamal Prasad Sharma**, Golap Kalita, Masaki Tanemura. Edge Controlled Growth of Hexagonal Boron Nitride Crystals by Atmospheric Chemical Vapor Deposition (Poster), **The 78th Japan society of applied physics (JSAP) autumn meeting**, 5th September 2017, Fukuoka, Japan

7. **Kamal Prasad Sharma**, Golap Kalita, Masaki Tanemura. Controllable Synthesis of Hexagonal Boron Nitride Crystals on Cu foils by Atmospheric Chemical Vapor Deposition (Poster), **The 5th Japan Society of Applied Physics Student Chapter Tokai Symposium 2017, JSAP SCTS 2017**, 29th October 2017, Nagoya University, Nagoya, Japan

8. **Kamal Prasad Sharma,** Golap Kalita, Masaki Tanemura. Chemical Vapor Deposition Based Rapid Graphene Growth System (Poster), **The 30th International Microprocesses and Nanotechnology (MNC) Conference** 2017, Jeju, Korea

List of Tables

List of Figures

SEM image of the h-BN on Cu synthesized with Method A (stepwise growth for 38min). (c, d) Enlarged SEM images of typical (c) h-BN single crystal grown across Cu grains and (d) h-BN crystals with wrinkles well-aligned over several h-BN crystals on a single Cu grain.

6.7 (a) AFM images of h-BN grown on Cu synthesized by method A. (b) AFM line profile measured along a blue arrow in Figure 6.7(a). (c) AFM images of h-BN transfered onto SiO_2/Si. h-BN was synthesized with Method A. AFM images of h-BN grown on Cu synthesized by (d) method E and (e) method F. 90

References

[1] Moore, G. E. No exponential is forever: But 'Forever' can be delayed, *Dig. Tech Papers Int. Solid-State Circuits Conf.*, **2003**, 20–23.

[2] Yakobson, B. I.; Smalley, R. E. Fullerene Nanotubes: $C_{1,000,000}$ and Beyond: Some Unusual New Molecules—long, Hollow Fibers with Tantalizing Electronic and Mechanical Properties—have Joined Diamonds and Graphite in the Carbon Family. *Am. Sci.* **1997**, *85*, 324–337.

[3] Ruoff, R.S.; Ruoff, A. L. The bulk modulus of C60 molecules and crystals: A molecular mechanics approach. *Appl. Phys. Lett.* **1991**, *59*, 1553–1555.

[4] Popov, V. N. Carbon Nanotubes: Properties and Application. *Mater. Sci. Eng. R Reports* **2004**, *43*, 61–102.

[5] De Volder, Michael F. L.; Tawfick, S. H.; Baughman, R. H.; Hart, A. J. Carbon Nanotubes: Present and Future Commercial Applications. *Science.* **2013**, *339*, 535–539.

[6] Landau L. D. Zur. Theorie der phasenumwandlungen I. *Physikalische Zeitschrift der Sow- jetunion*. **1937,** 11, 26–35.

[7] Peierls R. Quelques propriétés typiques des corps solides. *Annales de l'institut Henri Poincaré*. **1935,** 5 (3), 177–222.

[8] Arthur C. Clarke, profiles of the future. **1962**.

[9] E. A. Davis. Nevill Mott: Reminiscences And Appreciations. *CRC Press*, **1998**, 213.

[10] Rotkin, S. V.; Hess, K. Possibility of a Metallic Field-Effect Transistor. *Appl. Phys. Lett.* **2004**, *84*, 3139–3141.

[11] Giem, A. physics @FOM Veldhoven **2011**, evening lecture.

[12] Novoselov, K. S.; Geim, A. K.; Morozov, S. V.; Jiang, D.; Zhang, Y.; Dubonos, S.

V.; Grigorieva, I. V.; Firsov, A. A. Electric Field Effect in Atomically Thin Carbon Films. *Science* **2004***, 306,* 666–669.

[13] Gibney, E. 2D or Not 2D. *Nature* **2015**, *522*, 274–276.

[14] Geim, A. K.; Grigorieva, I. V. Van Der Waals Heterostructures. *Nature* **2014**, *499*, 419–425.

[15] Dean, C. R.; Young, A. F.; Meric, I.; Lee, C.; Wang, L.; Sorgenfrei, S.; Watanabe, K.; Taniguchi, T.; Kim, P.; Shepard, K. L.; Hone J. Boron Nitride Substrates for High-Quality Graphene Electronics. *Nat. Nanotechnol.* **2010**, *5*, 722–726.

[16] Tan, C.; Cao, X.; Wu, X.-J.; He, Q.; Yang, J.; Zhang, X.; Chen, J.; Zhao, W.; Han, S.; Nam, G.-H.; Sindoro, M.; Zhang, H. Recent Advances in Ultrathin Two-Dimensional Nanomaterials. *Chem. Rev.* **2017**, *117*, 6225−6331.

[17] Mak, K. F.; Lee, C.; Hone, J.; Shan, J.; Heinz, T. F. Atomically Thin MoS2: A New Direct-Gap Semiconductor. *Phys. Rev. Lett.* **2010**, *105*, 136805.

[18] Novoselov, K. S.; Fal'ko, V. I.; Colombo, L.; Gellert, P. R.; Schwab, M. G.; Kim, K. A Roadmap for Graphene. Nature **2012**, *490*, 192–200.

[19] Boehm, H. P.; Setton, R.; Stumpp, E. Nomenclature and terminology of graphite intercalation compounds. *Pure Appl.Chem.*, **1994,** *66*, 1893–1901

[20] Saito, R.; Dresselhaus, G.; Dresselhaus, M. S. Physical Properties of Carbon Nanotubes. *Imperial College Press* **1998**.

[21] Geim, A. K.; Novoselov, K. S. The Rise of Graphene. *Nat. Mater.* **2007**, *6*, 183–191..

[22] Gao, L.; Ni,G.-X.; Liu, B.; Castro Neto, A. H.; Loh, K. P. Face-to- face Transfer of Wafer-Scale Graphene Films. *Nature* **2014**, *505*, 190–194.

[23] Wallace, P. R. The Band Theory of Graphite. *Phys. Rev.*, **1947**, *71*, 622–634.

[24] Painter, G. S.; Ellis, D. E. Electronic Band Structure and Optical Properties of

Graphite from a Variational Approach. *Phys. Rev. B*, **1970**, *1*, 4747–4752.

[25] McClure, J.W. Band Structure of Graphite and de Haas-van Alphen Effect. *Phys.Rev.*, **1957**, *108*, 612–618.

[26] Novoselov, K. S.; Geim, A. K.; Morozov, S. V.; Jiang, D.; Katsnelson, M. I.; Grigorieva, I. V.; Dubonos, S. V.; Firsov, A. A. Two-Dimensional Gas of Massless Dirac Fermions in Graphene. *Nature* **2005**, *438*, 197–200.

[27] Bolotin, K. I.; Sikes, K. J.; Hone, J.; Stormer, H. L.; Kim, P. Temperature-Dependent Transport in Suspended Graphene. *Phys. Rev. Lett.* **2008**, *101*, 096802.

[28] Bolotin, K. I.; Sikes, K. J.; Jiang, Z.; Klima, M.; Fudenberg, G.; Hone, J.; Kim, P.; Stormer, H. L. Ultrahigh Electron Mobility in Suspended Graphene. *Solid State Commun.* **2008**, *146*, 351–355.

[29] Du, X.; Skachko, I.; Barker, A.; Andrei, E. Y. Approaching Ballistic Transport in Suspended Graphene. *Nat. Nanotechnol.* **2008**, *3*, 491–495.

[30] Morozov, S. V.; Novoselov, K. S.; Katsnelson, M. I.; Schedin, F.; Elias, D. C.; Jaszczak, J. A.; Geim, A. K. Giant Intrinsic Carrier Mobilities in Graphene and Its Bilayer. *Phys. Rev. Lett.* **2008**, *100*, 016602.

[31] Novoselov, K. S.; Jiang, Z.; Zhang, Y.; Morozov, S. V; Stormer, H. L.; Zeitler, U.; Maan, J. C.; Boebinger, G. S.; Kim, P.; Geim, A. K. Room-Temperature Quantum Hall Effect in Graphene. *Science* **2007**, *315*, 1379.

[32] Zhang, Y.; Tan, Y.; Stormer, H.; Kim, P. Experimental Observation of the Quantum Hall Effect and Berry's Phase in Graphene. *Nature* **2005**, *438*, 201–204.

[33] Casiraghi, C.; Pisana, S.; Novoselov, K. S.; Geim, A. K.; Ferrari, A. C. Raman Fingerprint of Charged Impurities in Graphene. *Appl. Phys. Lett.* **2007**, *91*, 233108.

[34] Pisana, S.; Lazzeri, M.; Casiraghi, C.; Novoselov, K. S.; Geim, A. K.; Ferrari, A. C.; Mauri, F. Breakdown of the Adiabatic Born-Oppenheimer Approximation in

Graphene. *Nat. Mater.* **2007**, *6*, 198–201.

[35] Fialkovsky, I. V.; Marachevsky, V. N.; Vassilevich, D. V. Finite-Temperature Casimir Effect for Graphene. *Phys. Rev. B* **2011**, *84*, 35446.

[36] Katsnelson, M. I.; Novoselov, K. S.; Geim, A. K. Chiral Tunnelling and the Klein Paradox in Graphene. *Nat. Phys.* **2006**, *2*, 620–625.

[37] Saito, K.; Nakamura, J.; Natori, A. Ballistic Thermal Conductance of a Graphene Sheet. *Phys. Rev. B. Phys.* **2007**, *76*, 115409.

[38] Nika, D. L.; Ghosh, S.; Pokatilov, E. P.; Balandin, A. A. Lattice Thermal Conductivity of Graphene Flakes: Comparison with Bulk Graphite. *Appl. Phys. Lett.* **2009**, *94*, 203103.

[39] Balandin, A. A.; Ghosh, S.; Bao, W.; Calizo, I.; Teweldebrhan, D.; Miao, F.; Lau, C. N. Superior Thermal Conductivity of Single-Layer Graphene. *Nano Lett.* **2008**, *8*, 902–907.

[40] Nair, R. R.; Blake, P.; Grigorenko, A. N.; Novoselov, K. S.; Booth, T. J.; Stauber, T.; Peres, N. M. R.; Geim, A. K. Fine Structure Constant Defines Visual Transperency of Graphene. *Science* **2008**, *320*, 1308.

[41] Zhao, H.; Aluru, N. R. Temperature and Strain-Rate Dependent Fracture Strength of Graphyne. *J. Appl. Phys.* **2014**, *47,* 064321.

[42] Lee, C.; Wei, X.; Kysar, J. W.; Hone, J. Measurement of the Elastic Properties and Intrinsic Strength of Monolayer Graphene. *Science* **2008**, *321*, 385–388.

[43] Elias, D. C.; Nair, R. R.; Mohiuddin, T. M. G.; Morozov, S. V.; Blake, P.; Halsall, M. P.; Ferrari, A. C.; Boukhvalov, D. W.; Katsnelson, M. I.; Geim, A. K.; Novoselov, K. S. Control of Graphene's Properties by Reversible Hydrogenation: Evidence for Graphane. *Science.* **2009**, *323*, 610–613.

[44] Bunch, J. S.; Verbridge, S. S.; Alden, J. S.; Van Der Zande, A. M.; Parpia, J. M.;

Craighead, H. G.; McEuen, P. L. Impermeable Atomic Membranes from Graphene Sheets. *Nano Lett.* **2008**, *8*, 2458–2462.

[45] Berger, C.; Song, Z.; Li, X.; Wu, X.; Brown, N.; Naud, C.; Mayou, D.; Li, T.; Hass, J.; Marchenkov, A. N.; Conrad, E. H.; First, P. N.; de Heer, W. A. Electronic Confinement and Coherence in Patterned Epitaxial Graphene. *Science* **2006**, *312*, 1191–1196.

[46] Ponomarenko, L. A.; Schedin, F.; Katsnelson, M. I.; Yang, R.; Hill, E. W.; Novoselov, K. S.; Geim, A. K. Chaotic Dirac Billiard in Graphene Quantum Dots. *Science* **2008**, *320*, 356–358.

[47] Castro Neto, A. H.; Peres, N. M. R.; Novoselov, K. S.; Geim, A. K. The Electronic Properties of Graphene. *Rev. Mod. Phys.* **2009**, *81*, 109–162.

[48] Liao, L.; Lin, Y. C.; Bao, M.; Cheng, R.; Bai, J.; Liu, Y.; Qu, Y.; Wang, K. L.; Huang, Y.; Duan, X. High-Speed Graphene Transistors with a Self-Aligned Nanowire Gate. *Nature* **2010**, *467*, 305–308.

[49] Wu, Y.; Lin, Y. M.; Bol, A. A.; Jenkins, K. A.; Xia, F.; Farmer, D. B.; Zhu, Y.; Avouris, P. High-Frequency, Scaled Graphene Transistors on Diamond-like Carbon. *Nature* **2011**, *472*, 74–78.

[50] Pop, E.; Varshney, V.; Roy, A. K. Thermal Properties of Graphene: Fundamentals and Applications. *MRS Bull.* **2012**, *37*, 1273–1281.

[51] Bae, S.; Kim, H.; Lee, Y.; Xu, X.; Park, J.-S.; Zheng, Y.; Balakrishnan, J.; Lei, T.; Ri Kim, H.; Song, Y. I.; Kim, Y.-J.; Kim, K. S.; Ozyilmaz, B.; Ahn, J.-H.; Hong, B. H.; Iijima, S. Roll-to-Roll Production of 30-Inch Graphene Films for Transparent Electrodes. *Nat. Nanotechnol.* **2010**, *5*, 574–578.

[52] Schwierz, F. Graphene Transistors: Status, Prospects, and Problems. *Proc. IEEE* **2013**, *101*, 1567–1584.

[53] Reina, A.; Jia, X.; Ho, J.; Nezich, D.; Son, H.; Bulovic, V.; Dresselhaus, M. S.; Jing, K. Large Area, Few-Layer Graphene Films on Arbitrary Substrates by Chemical Vapor Deposition. *Nano Lett.* **2009**, *9*, 30–35.

[54] Li, X.; Zhu, Y. W.; Cai, W.; Borysiak, M.; Han, B.; Chen, D.; Piner, R. D.; Colombo, L.; Ruoff, R. S. Transfer of Large-Area Graphene Films for High-Performance Transparent Conductive Electrodes. *Nano Lett.* **2009**, *9*, 4359–4363.

[55] Bonaccorso, F.; Sun, Z.; Hasan, T.; Ferrari, A. C. Graphene Photonics and Optoelectronics. *Nat. Photonics* **2010**, *4*, 611–622.

[56] Bae, S.-H; Lee, Y.; Sharma, B. K.; Lee, H.-J; Kim, J.-H.; Ahn, J.-H Graphene-Based Transparent Strain Sensor. *Carbon* **2012**, *51*, 236–242.

[57] Blake, P.; Brimicombe, P. D.; Nair, R. R.; Booth, T. J.; Jiang, D.; Schedin, F.; Ponomarenko, L. A.; Morozov, S. V; Gleeson, H. F.; Hill, E. W.; Geim, A. K.; Novoselov, K. S. Graphene-Based Liquid Crystal Device. *Nano Lett.* **2008**, *8*, 1704–1708.

[58] Ryu, J.; Kim, Y.; Won, D.; Kim, N.; Park, J. S.; Lee, E -K.; Cho, D.; Cho, S.-P.; Kim, S. J.; Ryu, G. H.; Shin, H. S.; Lee, Z.; Hong, B. H.; Cho, S. Fast Synthesis of High-Performance Graphene by Rapid Thermal Chemical Vapor Deposition. *ACS Nano* **2014**, *8*, 950–956.

[59] Ahn, J-H; Hong B. H. Things You Could Do with Graphene, "Graphene for Displays That Bend". *Nature Nanotechnol.* **2014**, *9*, 737–747.

[60] Zhu, Y.; Murali, S.; Cai, W.; Li, X.; Suk, J. W.; Potts, J. R.; Ruoff, R. S. Graphene and Graphene Oxide: Synthesis, Properties, and Applications. *Adv. Mater.* **2010**, *22*, 3906–3924.

[61] Ramanathan, T.; Abdala, A. A.; Stankovich, S.; Dikin, D. A.; Herrera-Alonso, M.; Piner, R. D.; Adamson, D. H.; Schniepp, H. C.; Chen, X.; Ruoff, R. S.; Nguyen, S.

T.; Aksay, I. A.; Prud'Homme, R. K.; Brinson, L. C. Functionalized Graphene Sheets for Polymer Nanocomposites. *Nat. Nanotechnol.* **2008**, *3*, 327–331.

[62] Kim, H.; Abdala, A. A.; MacOsko, C. W. Graphene/polymer Nanocomposites. *Macromolecules* **2010**, *43*, 6515–6530.

[63] Wang, Q.; Wang, C.; Zhang, M.; Jian, M.; Zhang, Y. Feeding Single-Walled Carbon Nanotubes or Graphene to Silkworms for Reinforced Silk Fibers. *Nano Lett.* **2016**, *16*, 6695–6700.

[64] Liu, J. Things You Could Do with Graphene, "Charging graphene for energy". *Nat. Nanotechnol.* **2014**, *9*, 739–741.

[65] Miller, J. R.; Outlaw, R. A.; Holloway, B. C. Graphene Double Layer Capacitor with Ac Line Filtering Performance. *Science* **2010**, *329*, 44120–44120.

[66] Zhu, Y.; Murali, S.; Stoller, M. D.; Ganesh, K. J.; Cai, W.; Ferreira, P. J.; Pirkle, A.; Wallace, R. M.; Cychosz, K. A.; Thommes, M.; Su, D.; Stach, E. A.; Ruoff, R. S. Carbon-Based Supercapacitors Produced by Activation of Graphene. *Science* **2011**, *332*, 1537–1542.

[67] Prasai, D.; Tuberquia, J. C.; Harl, R. R.; Jennings, G. K.; Bolotin, K. I. Graphene: Corrosion-Inhibiting Coating. *ACS Nano* **2012**, *6*, 1102–1108.

[68] Böhm, S. Things You Could Do with Graphene, "graphene against corrosion". *Nat. Nanotechnol.* **2014**, *9*, 741–742.

[69] Garaj, S.; Hubbard, W.; Reina, A.; Kong, J.; Branton, D.; Golovchenko, J. A. Graphene as a Subnanometre Trans-Electrode Membrane. *Nature* **2010**, *467*, 190–193.

[70] Yang, L.; Zhang, L.; Webster, T. J. Carbon Nanostructures for Orthopedic Medical Applications. *Nanomedicine* **2011**, *6*, 1231–1244.

[71] Geim, A. K. Graphene : Status and Prospects. *Science* **2009**, *324*, 1530–1534.

[72] Lu, X.; Yu, M.; Huang, H.; Ruoff, R. S. Tailoring Graphite with the Goal of Achieving Single Sheets. *Nanotechnology* **1999**, *10*, 269–272.

[73] Bonaccorso, F.; Lombardo, A.; Hasan, T.; Sun, Z.; Colombo, L.; Ferrari, A. C. Production and Processing of Graphene and 2d Crystals. *Mater. Today* **2012**, *15*, 564–589.

[74] Hernandez, Y.; Nicolosi, V.; Lotya, M.; Blighe, F. M.; Sun, Z.; De, S.; McGovern, I. T.; Holland, B.; Byrne, M.; Gun'ko, Y. K.; Boland, J. J.; Niraj, P.; Duesberg, G.; Krishnamurthy, S.; Goodhue, R.; Hutchison, J.; Scardaci, V.; Ferrari, A. C.; Coleman, J. N. High-Yield Production of Graphene by Liquid-Phase Exfoliation of Graphite. *Nat. Nanotechnol.* **2008**, *3*, 563–568.

[75] O'Neill, A.; Khan, U.; Nirmalraj, P. N.; Boland, J.; Coleman, J. N. Graphene Dispersion and Exfoliation in Low Boiling Point Solvents. *J. Phys. Chem. C* **2011**, *115*, 5422–5428.

[76] Behrens, M. Über Die Verteilung Der Lipase Und Arginase Zwischen Zellkern Und Protoplasma Der Leber. Mit L Figur Im Text. *Hoppe. Seylers. Z. Physiol. Chem.* **2009**, *258*, 27–32.

[77] Maragó, O. M.; Bonaccorso, F.; Saija, R.; Privitera, G.; Gucciardi, P. G.; Iatì, M. A.; Calogero, G.; Jones, P. H.; Borghese, F.; Denti, P.; Nicolosi, V.; Ferrari, A. C. Brownian Motion of Graphene. *ACS Nano* **2010**, *4*, 7515–7523.

[78] Khan, U.; O'Neill, A.; Lotya, M.; De, S.; Coleman, J. N. High-Concentration Solvent Exfoliation of Graphene. *Small* **2010**, *6*, 864–871.

[79] Alzari, V.; Nuvoli, D.; Scognamillo, S.; Piccinini, M.; Gioffredi, E.; Malucelli,G.; Marceddu, S.; Sechi M.; Sannab, V.; Mariani, A. Graphene-Containing Thermoresponsive Nanocomposite Hydrogels of Poly (N-Isopropylacrylamide) Prepared by Frontal Polymerization. *J. Mater. Chem.* **2011**, *21*, 8727–8733.

[80] Lotya, M.; Hernandez, Y.; King, P. J.; Smith, R. J.; Nicolosi, V.; Karlsson, L. S.; Blighe, M.; De, S.; Wang, Z.; Mcgovern, I. T.; Alzari, V.; Scognamillo, D. N.; Duesberg, S. G. S.; Coleman, J. N. Liquid Phase Production of Graphene by Exfoliation of Graphite in Surfactant / Water Solutions. *J. Am. Chem. Soc.* **2009**, *131*, 3611–3620.

[81] Torrisi, F.; Torrisi, T.; Hasan, W.; Wu, Z.; Sun, A.; Lombardo, T.; Kulmala, G.-W.; Hsieh, S.; Jung, F.; Bonaccorso, P.; Paul, P. J.; Chu, D.; Ferrari, A. C. Inkjet-Printed Graphene Electronics. *ACS Nano* **2012**, *6*, 2992–3006.

[82] Brodie, B. C. XXIII.–Researches on the Atomic Weight of Graphite. *Q. J. Chem. Soc. London* **1860**, *12*, 261–268.

[83] Staudenmaier, L. Verfahren Zur Darstellung Der Graphitsäure. *Eur. J. Inorg. Chem.* **1898**, *31*, 1481–1487.

[84] William S. Hummers, J.; Offeman, R. E.; Jr, W. S. H.; William S. Hummers, J.; Offeman, R. E.; Hummers, W. S.; Offeman, R. E. Preparation of Graphitic Oxide. *J. Am. Chem. Soc.* **1958**, *80*, 1939.

[85] Héctor, A. B.; Jie, M.; Zunfeng, L.; Randall, M. Stoltenberg Zhenan, B.; Yongsheng, C. Evaluation of Solution-Processed Reduced Graphene Oxide Films as as Transparent Conductors. *ACS Nano* **2008**, *2*, 463–470.

[86] Matyba, P.; Yamaguchi, H.; Eda, G.; Chhowalla, M.; Edman, L.; Robinson, N. D. Graphene and Mobile Ions: The Key to All-Plastic, Solution-Processed Light-Emitting Devices. *ACS Nano* **2010**, *4*, 637–642.

[87] Sun, X.; Liu, Z.; Welsher, K.; Robinson, J. T.; Goodwin, A.; Zaric, S.; Dai, H. Nano-Graphene Oxide for Cellular Imaging and Drug Delivery. *Nano Res.* **2008**, *1*, 203–212.

[88] Chua, C. K.; Pumera, M. Chemical Reduction of Graphene Oxide: A Synthetic

Chemistry Viewpoint. *Chem. Soc. Rev.* **2014**, *43*, 291–312.

[89] Stankovich, S.; Dikin, D. A.; Dommett, G. H. B.; Kohlhaas, K. M.; Zimney, E. J.; Stach, E. A.; Piner, R. D.; Nguyen, S. B. T.; Ruoff, R. S. Graphene-Based Composite Materials. *Nature* **2006**, *442*, 282–286.

[90] Pei, S.; Cheng, H. M. The Reduction of Graphene Oxide. *Carbon N. Y.* **2012**, *50*, 3210–3228.

[91] Emtsev, K. V.; Bostwick, A.; Horn, K.; Jobst, J.; Kellogg, G. L.; Ley, L.; McChesney, J. L.; Ohta, T.; Reshanov, S. A.; Röhrl, J.; Rotenberg, E.; Schmid, A. K.; Waldmann, D; Weber, H. B.; Seyller, T. Towards Wafer-Size Graphene Layers by Atmospheric Pressure Graphitization of Silicon Carbide. *Nat. Mater.* **2009**, *8*, 203–207.

[92] Emtsev, K. V.; Speck, F.; Seyller, T.; Ley, L.; Riley, J. D. Interaction, Growth, and Ordering of Epitaxial Graphene on SiC{0001} Surfaces: A Comparative Photoelectron Spectroscopy Study. *Phys. Rev. B* **2008**, *77*, 155303.

[93] Forbeaux, I.; Themlin, J. M.; Charrier, A.; Thibaudau, F.; Debever, J. M. Solid-State Graphitization Mechanisms of Silicon Carbide 6H-SiC Polar Faces. *Appl. Surf. Sci.* **2000**, *162*, 406–412.

[94] Charrier, A.; Coati, A.; Argunova, T.; Thibaudau, F.; Garreau, Y.; Pinchaux, R.; Forbeaux, I.; Debever, J. M.; Sauvage-Simkin, M.; Themlin, J. M. Solid-State Decomposition of Silicon Carbide for Growing Ultra-Thin Heteroepitaxial Graphite Films. *J. Appl. Phys.* **2002**, *92*, 2479–2484.

[95] Hass, J.; Millán-Otoya, J. E.; First, P. N.; Conrad, E. H. Interface Structure of Epitaxial Graphene Grown on 4H-SiC(0001). *Phys. Rev. B* **2008**, *78*, 205424.

[96] Hass, J.; Feng, R.; Li, T.; Li, X.; Zong, Z.; De Heer, W. A.; First, P. N.; Conrad, E. H.; Jeffrey, C. A.; Berger, C. Highly Ordered Graphene for Two Dimensional

Electronics. *Appl. Phys. Lett.* **2006**, *89,* 143106.

[97] Shivaraman, S.; Barton, R. A.; Yu, X.; Alden, J.; Herman, L.; Chandrashekhar, M.; Park, J.; McEuen, P. L.; Parpia, J. M.; Craighead, H. G.; Spencher, M. G. Free-Standing Epitaxial Graphene. *Nano Lett.* **2009**, *9*, 3100–3105.

[98] Cai, T.; Jia, Z.; Yan, B.; Yu, D.; Wu, X. Hydrogen Assisted Growth of High Quality Epitaxial Graphene on the C-Face of 4H-SiC. *Appl. Phys. Lett.* **2015**, *106*, 013106.

[99] de Heer, W. A.; Berger, C.; Ruan, M.; Sprinkle, M.; Li, X.; Hu, Y.; Zhang, B.; Hankinson, J.; Conrad, E. Large Area and Structured Epitaxial Graphene Produced by Confinement Controlled Sublimation of Silicon Carbide. *Proc. Natl. Acad. Sci.* **2011**, *108*, 16900–16905.

[100] Huang, H.; Chen, W.; Chen, S.; Wee, A. T. S. Bottom-up Growth of Epitaxial Graphene on 6H-SiC(0001). *ACS Nano* **2008**, *2*, 2513–2518.

[101] Mcardle, T. J.; Chu, J. O.; Zhu, Y.; Liu, Z.; Krishnan, M.; Breslin, C. M.; Dimitrakopoulos, C.; Wisnieff, R.; Grill, A. Multilayer Epitaxial Graphene Formed by Pyrolysis of Polycrystalline Silicon-Carbide Grown on c-Plane Sapphire Substrates. *Appl. Phys. Lett.* **2011**, *98*, 2012–2015.

[102] Coletti, C.; Emtsev, K. V.; Zakharov, A. A.; Ouisse, T.; Chaussende, D.; Starke, U. Large Area Quasi-Free Standing Monolayer Graphene on 3C-SiC(111). *Appl. Phys. Lett.* **2011**, *99*, 2012–2015.

[103] Zheng, W.; Wong, S. Electrical Conductivity and Dielectric Properties of PMMA/expanded Graphite Composites Wenge. *Compos. Sci. Technol.* **2003**, *63*, 225–235.

[104] Kim, K. S.; Zhao, Y.; Jang, H.; Lee, S. Y.; Kim, J. M.; Kim, K. S.; Ahn, J. H.; Kim, P.; Choi, J. Y.; Hong, B.H. Large-Scale Pattern Growth of Graphene Films for Stretchable Transparent Electrodes. *Nature* **2009**, *457*, 706–710.

[105] Coraux, J.; N'Diaye, A. T.; Busse, C.; Michely, T. Structural Coherency of Graphene on Ir(111). *Nano Lett.* **2008**, *8*, 565–570.

[106] Sutter, P. W.; Flege, J. I.; Sutter, E. A. Epitaxial Graphene on Ruthenium. *Nat. Mater.* **2008**, *7*, 406–411.

[107] Varykhalov, A.; Rader, O. Graphene Grown on Co(0001) Films and Islands: Electronic Structure and Its Precise Magnetization Dependence. *Phys. Rev. B* **2009**, *80*, 035437.

[108] Wang, S. M.; Pei, Y. H.; Wang, X.; Wang, H.; Meng, Q. N.; Tian, H. W.; Zheng, X. L.; Zheng, W. T.; Liu, Y. C. Synthesis of Graphene on a Polycrystalline Co Film by Radio-Frequency Plasma-Enhanced Chemical Vapour Deposition. *J. Phys. D. Appl. Phys.* **2010**, *43*, 455402.

[109] Sutter, P.; Sadowski, J. T.; Sutter, E. Graphene on Pt(111): Growth and Substrate Interaction. *Phys. Rev. B* **2009**, *80*, 245411.

[110] Gao, L.; Ren, W.; Xu, H.; Jin, L.; Wang, Z.; Ma, T.; Ma, L.-P.; Zhang, Z.; Fu, Q.; Peng, L.-M. Repeated Growth and Bubbling Transfer of Graphene with Millimetre-Size Single-Crystal Grains Using Platinum. *Nat. Commun.* **2012**, *3*, 699.

[111] Kwon, S. Y.; Ciobanu, C. V.; Petrova, V.; Shenoy, V. B.; Bareño, J.; Gambin, V.; Petrov, I.; Kodambaka, S. Growth of Semiconducting Graphene on Palladium. *Nano Lett.* **2009**.

[112] Miniussi, E.; Pozzo, M.; Baraldi, A.; Vesselli, E.; Zhan, R. R.; Comelli, G.; Menteş, T. O.; Niño, M. A.; Locatelli, A.; Lizzit, S.; Alfè; D. Thermal Stability of Corrugated Epitaxial Graphene Grown on Re(0001). *Phys. Rev. Lett.* **2011**, *106*, 216101.

[113] Li, X.; Cai, W.; An, J.; Kim, S.; Nah, J.; Yang, D.; Piner, R.; Velamakanni, A.; Jung, I.; Tutuc, E.; Banerjee, S. K.; Colombo, L.; Ruoff, R. S. Large-Area Synthesis of

High-Quality and Uniform Graphene Films on Copper Foils. *Science* **2009**, *324*, 1312–1314.

[114] Chen, X.; Zhao, P.; Xiang, R.; Kim, S.; Cha, J.; Chiashi, S.; Maruyama, S. Chemical Vapor Deposition Growth of 5 Mm Hexagonal Single-Crystal Graphene from Ethanol. *Carbon N. Y.* **2015**, *94*, 810–815.

[115] Sun, Z.; Yan, Z.; Yao, J.; Beitler, E.; Zhu, Y.; Tour, J. M. Growth of Graphene from Solid Carbon Sources. *Nature* **2010**, *468,* 549–552.

[116] Ruan, G.; Sun, Z.; Peng, Z.; Tour, J. M. Growth of Graphene from Food, Insects, and Waste. *ACS Nano* **2011**, *5*, 7601–7607.

[117] Sharma, S.; Kalita, G.; Hirano, R.; Shinde, S. M.; Papon, R.; Ohtani, H.; Tanemura, M. Synthesis of Graphene Crystals from Solid Waste Plastic by Chemical Vapor Deposition. *Carbon N. Y.* **2014**, *72*, 66–73.

[118] Sharma, K. P.; Shinde, S. M.; Rosmi, M. S.; Sharma, S.; Kalita, G.; Tanemura, M. Effect of Copper Foil Annealing Process on Large Graphene Domain Growth by Solid Source-Based Chemical Vapor Deposition. *J. Mater. Sci.* **2016**, *51*, 7220–7228.

[119] Karu, A. E.; Beer, M. Pyrolytic Formation of Highly Crystalline Graphite Films. *J. Appl. Phys.* **1966**, *37*, 2179–2181.

[120] May, J. W. Platinum Surface LEED Rings. *Surf. Sci.* **1969**, *17*, 267–270.

[121] Kholin, N.A.; Rut'kov, E.V.; Tontegode, A.Y. The nature of the adsorption bond between graphite islands and iridium surface. *Surf. Sci.* **1984**, *139*, 155–172.

[122] Gall, N. R.; Rut'Kov, E. V.; Tontegode, A. Y. Intercalation of Nickel Atoms under Two-Dimensional Graphene Film on (111)Ir. *Carbon N. Y.* **2000**, *38*, 663–667.

[123] Bartelt, N. C.; McCarty, K. F. Graphene Growth on Metal Surfaces. *MRS Bull.* **2012**, *37*, 1158–1165.

[124] Marago, O. M.; Jones, P. H.; Bonaccorso, F.; Scardaci, V.; Gucciardi, P. G.; Rozhin, A. G.; Ferrari, A. C. Femtonewton Force Sensing with Optically Trapped Nanotubes. *Nano Lett.* **2008**, *8*, 3211–3216.

[125] Kobayashi, T.; Bando, M.; Kimura, N.; Shimizu, K.; Kadono, K.; Umezu, N.; Miyahara, K.; Hayazaki, S.; Nagai, S.; Mizuguchi, Y.; Murakami, Y.; Hobara, D. Production of a 100-M-Long High-Quality Graphene Transparent Conductive Film by Roll-to-Roll Chemical Vapor Deposition and Transfer Process. *Appl. Phys. Lett.* **2013**, *102*, 023112.

[126] Vlassiouk, I.; Fulvio, P.; Meyer, H.; Lavrik, N.; Dai, S.; Datskos, P.; Smirnov, S. Large Scale Atmospheric Pressure Chemical Vapor Deposition of Graphene. *Carbon N. Y.* **2012**, *54*, 58–67.

[127] Zhong, G.; Wu, X.; Arsie, L. D.; Teo, K. B. K.; Rupesinghe, N. L.; Jouvray, A.; Robertson, J. Growth of Continuous Graphene by Open Roll-to-Roll Chemical Vapor Deposition. *Appl. Phys. Lett.* **2016**, *109*. 193103

[128] Polsen, E. S.; McNerny, D. Q.; Viswanath, B.; Pattinson, S. W.; John Hart, A. High-Speed Roll-to-Roll Manufacturing of Graphene Using a Concentric Tube CVD Reactor. *Sci. Rep.* **2015**, *5*, 1–12.

[129] Deokar, G.; Avila, J.; Razado-Colambo, I.; Codron, J. L.; Boyaval, C.; Galopin, E.; Asensio, M. C.; Vignaud, D. Towards High Quality CVD Graphene Growth and Transfer. *Carbon N. Y.* **2015**, *89*, 82–92.

[130] Lee, H. C.; Jo, S. B.; Lee, E.; Yoo, M. S.; Kim, H. H.; Lee, S. K.; Lee, W. H.; Cho, K. Facet-Mediated Growth of High-Quality Monolayer Graphene on Arbitrarily Rough Copper Surfaces. *Adv. Mater.* **2016**, *28*, 2010–2017.

[131] Zhou, H.; Yu, W. J.; Liu, L.; Cheng, R.; Chen, Y.; Huang, X.; Liu, Y.; Wang, Y.; Huang, Y.; Duan, X. Chemical Vapour Deposition Growth of Large Single Crystals

of Monolayer and Bilayer Graphene. *Nat. Commun.* **2013**, *4*, 2096.

[132] Hofmann, S.; Braeuninger-Weimer, P.; Weatherup, R. S. CVD-Enabled Graphene Manufacture and Technology. *J. Phys. Chem. Lett., 2015, 6, 2714–2721*.

[133] Geng, D.; Meng, L.; Chen, B.; Gao, E.; Yan, W.; Yan, H.; Luo, B.; Xu, J.; Wang, H.; Mao, Z.; *et al.* Controlled Growth of Single-Crystal Twelve-Pointed Graphene Grains on a Liquid Cu Surface. *Adv. Mater.* **2014**, *26*, 6423–6429.

[134] Geng, D.; Wu, B.; Guo, Y.; Huang, L.; Xue, Y.; Chen, J.; Yu, G.; Jiang, L.; Hu, W.; Liu, Y. Uniform Hexagonal Graphene Flakes and Films Grown on Liquid Copper Surface. *Proc. Natl. Acad. Sci.* **2012**, *109*, 7992–7996.

[135] Meca, E.; Lowengrub, J.; Kim, H.; Mattevi, C.; Shenoy, V. Epitaxial Graphene Growth and Shape Dynamics on Copper: Phase- Field Modeling and Experiments. *Nano Lett.* **2013**, *13*, 5692–5697.

[136] Jacobberger, R. M.; Arnold, M. S. Graphene Growth Dynamics on Epitaxial Copper Thin Films. *Chem. Mater.* **2013**, *25*, 871–877.

[137] Wu, B.; Geng, D.; Xu, Z.; Guo, Y.; Huang, L.; Xue, Y.; Chen, J.; Yu, G.; Liu, Y. Self-Organized Graphene Crystal Patterns. *NPG Asia Mater.* **2013**, *5*, e36.

[138] Artyukhov, V. I.; Liu, Y.; Yakobson, B. I. Equilibrium at the Edge and Atomistic Mechanisms of Graphene Growth. *Proc. Natl. Acad. Sci.* **2012**, *109*, 15136–15140.

[139] Li, X.; Magnuson, C. W.; Venugopal, A.; An, J.; Suk, J. W.; Han, B.; Borysiak, M.; Cai, W. W.; Velamakanni, A.; Zhu, Y. W.; Fu, L. F.; Vogel, E. M.; Voelkl, E.; Colombo, L.; Ruoff, R. S. Graphene Films with Large Domain Size by a Two-Step Chemical Vapor Deposition Process. *Nano Lett.* **2010**, *10*, 4328–4334.

[140] Hao, Y.; Bharathi, M. S.; Wang, L.; Liu, Y.; Chen, H.; Nie, S.; Wang, X.; Chou, H.; Tan, C.; Fallahazad, B.; Ramanarayan, H.; Magnuson, C. W.; Tutuc, E.; Yakobson, B. I.; McCarty, K. F.; Zhang, Y.-W.; Kim, P.; Hone, J.; Colombo, L.; Ruoff, R. S.

The Role of Surface Oxygen in the Growth of Large Single-Crystal Graphene on Copper. *Science* **2013**, *342*, 720–723.

[141] Vlassiouk, I.; Smirnov, S.; Regmi, M.; Surwade, S. P.; Srivastava, N.; Feenstra, R.; Eres, G.; Parish, C.; Lavrik, N.; Datskos, P.; Dai, S.; Fulvio, P. Graphene Nucleation Density on Copper: Fundamental Role of Background Pressure. *J. Phys. Chem. C* **2013**, *117*, 18919–18926.

[142] Xu, X.; Zhang, Z.; Qiu, L.; Zhuang, J.; Zhang, L.; Wang, H.; Liao, C.; Song, H.; Qiao, R.; Gao, P.; Hu, Z.; Liao, L.; Liao, Z.; Yu, D.; Wang, E.; Ding, F.; Peng, H.; Liu, K. Ultrafast Growth of Single-Crystal Graphene Assisted by a Continuous Oxygen Supply. *Nat. Nanotechnol.* **2016**, *11*, 1–13.

[143] Safron, N. S.; Arnold, M. S. Experimentally Determined Model of Atmospheric Pressure CVD of Graphene on Cu. *J. Mater. Chem. C* **2014**, *2*, 744–755.

[144] Terasawa, T. O.; Saiki, K. Radiation-Mode Optical Microscopy on the Growth of Graphene. *Nat. Commun.* **2015**, *6*, 1–6.

[145] Zhang, Y.; Zhang, L.; Zhou, C. Review of Chemical Vapor Deposition of Graphene and Related Applications. *Acc. Chem. Res.* **2013**.

[146] Pakdel, A.; Bando, Y.; Golberg, D. Nano Boron Nitride Flatland. *Chem Soc Rev* **2014**, *43*, 934–959.

[147] Chopra, N. G.; Luyken, R. J.; Cherrey, K.; Crespi, V. H.; Cohen, M. L.; Louie, S. G.; Zettl, A. Boron Nitride Nanotubes. *Science* **1995**, *269*, 966–967.

[148] Stéphan, O.; Bando, Y.; Loiseau, A.; Willaime, F.; Shramchenko, N.; Tamiya, T.; Sato, T. Formation of Small Single-Layer and Nested BN Cages under Electron Irradiation of Nanotubes and Bulk Material. *Appl. Phys. A Mater. Sci. Process.* **1998**, *67*, 107–111.

[149] Golberg, D.; Bando, Y.; Stéphan, O.; Kurashima, K. Octahedral Boron Nitride

Fullerenes Formed by Electron Beam Irradiation Octahedral Boron Nitride Fullerenes Formed by Electron Beam Irradiation. *Appl. Phys. Lett.* **1998**, *73*, 2441-2443.

[150] Novoselov, K. S.; Jiang, D.; Schedin, F.; Booth, T. J.; Khotkevich, V. V.; Morozov, S. V.; Geim, A. K. Two-Dimensional Atomic Crystals. *Proc. Natl. Acad. Sci.* **2005**, *102*, 10451–10453.

[151] Corso, M.; Auwärter, W.; Muntwiler, M.; Tamai, A.; Greber, T.; Osterwalder, J. Boron Nitride Nanomesh. *Science* **2004**, *303*, 217–220.

[152] Lin, Y.; Connell, J. W. Advances in 2D Boron Nitride Nanostructures: Nanosheets, Nanoribbons, Nanomeshes, and Hybrids with Graphene. *Nanoscale* **2010**, *4*, 6908.

[153] Ooi, N.; Rairkar, A.; Lindsley, L.; Adams, J. B. Electronic Structure and Bonding in Hexagonal Boron Nitride. *J. Phys. Condens. Matter* **2006**, *18*, 97–115.

[154] Won, C. Y.; Aluru, N. R. Structure and Dynamics of Water Confined in a Boron Nitride Nanotube. *J. Phys. Chem. B* **2008**, *112*, 1812–1818.

[155] Blase, X.; De Vita, A.; Charlier, J. C.; Car, R. Frustration Effects and Microscopic Growth Mechanisms for BN Nanotubes. *Phys. Rev. Lett.* **1998**, *80*, 1666–1669.

[156] Golberg, D.; Bando, Y.; Huang, Y.; Terao, T.; Mitome, M.; Tang, C. Boron Nitride Nanotubes and Nanosheets. *ACS Nano* **2010**, *4*, 2979–2993.

[157] Marom, N.; Bernstein, J.; Garel, J.; Tkatchenko, A.; Joselevich, E.; Kronik, L.; Hod, O. Stacking and Registry Effects in Layered Materials: The Case of Hexagonal Boron Nitride. *Phys. Rev. Lett.* **2010**, *105*, 046801.

[158] Warner, J. H.; Rummeli, M. H.; Bachmatiuk, A.; Buchner, B. Atomic Resolution Imaging and Topogarphy of Boron Nitride Sheet Produced by Chemical Exfoliation. *ACS Nano* **2010**, *4*, 1299–1304.

[159] Ribeiro, R. M.; Peres, N. M. R. Stability of Boron Nitride Bilayers: Ground-State

Energies, Interlayer Distances, and Tight-Binding Description. *Phys. Rev. B* **2011**, *83*, 235312.

[160] Engler, M.; Ruisinger, B.; Damasch, R.; Ruisinger, B.; Eichler,J. Hexagonal Boron Nitride (hBN) – Applications from Metallurgy to Cosmetics. *Ceram. forum Int.* **2007**, *12*, 49–53.

[161] Li, J.; Dahal, R.; Majety, S.; Lin, J. Y.; Jiang, H. X. Hexagonal Boron Nitride Epitaxial Layers as Neutron Detector Materials. *Nucl. Instruments Methods Phys. Res. Sect. A Accel. Spectrometers, Detect. Assoc. Equip.* **2011**, *654*, 417–420.

[162] Solozhenko, V. L.; Lazarenko, a G.; Petitet, J. P.; Kanaev, a V. Bang Gap Energy of Graphite-like Hexagonal Boron Nitride. *J. Phys. Chem. Solids* **2001**, *62*, 1331–1334.

[163] Liu, L.; Feng, Y. P.; Shen, Z. X. Structural and Electronic Properties of *H* -BN. *Phys. Rev. B* **2003**, *68*, 104102.

[164] Watanabe, K.; Taniguchi, T.; Kanda, H. Direct-Bandgap Properties and Evidence for Ultraviolet Lasing of Hexagonal Boron Nitride Single Crystal. *Nat Mater* **2004**, *3*, 404–409.

[165] Taniguchi, T.; Watanabe, K. Synthesis of High-Purity Boron Nitride Single Crystals under High Pressure by Using Ba-BN Solvent. *J. Cryst. Growth* **2007**, *303*, 525–529.

[166] Blase, X.; Rubio, A.; Louie, S. G.; Cohen, M. L. Quasiparticle Band Structure of Bulk Hexagonal Boron Nitride and Related Systems. *Phys. Rev. B* **1995**, *51*, 51,6868.

[167] Weitz, R. T.; Yacoby, A. Graphene Rests Easy. *Nat. Nanotechnol.* **2010**, *5*, 699–700.

[168] Giovannetti, G.; Khomyakov, P. A.; Brocks, G.; Kelly, P. J.; Van Den Brink, J. Substrate-Induced Band Gap in Graphene on Hexagonal Boron Nitride: Ab Initio Density Functional Calculations. *Phys. Rev. B* **2007**, *76*, 073103.

[169] Sevik, C.; Kinaci, A.; Haskins, J. B.; Cagin, T. Characterization of Thermal Transport in Low-Dimensional Boron Nitride Nanostructures. *Phys. Rev. B* **2011**, *84*, 085409.

[170] Ouyang, T.; Chen, Y.; Xie, Y.; Yang, K.; Bao, Z.; Zhong, J. Thermal Transport in Hexagonal Boron Nitride Nanoribbons. *Nanotechnology* **2010**, *21*, 245701.

[171] Lindsay, L.; Broido, D. A. Theory of Thermal Transport in Multilayer Hexagonal Boron Nitride and Nanotubes. *Phys. Rev. B* **2012**, *85*, 35436.

[172] Jo, I.; Pettes, M. T.; Kim, J.; Watanabe, K.; Taniguchi, T.; Yao, Z.; Shi, L. Thermal Conductivity and Phonon Transport in Suspended Few-Layer Hexagonal Boron Nitride. *Nano Lett.* **2013**, *13*, 550–554.

[173] Lindsay, L.; Broido, D. A. Enhanced Thermal Conductivity and Isotope Effect in Single-Layer Hexagonal Boron Nitride. *Phys. Rev. B* **2011**, *84*, 155421.

[174] Song, L.; Ci, L.; Lu, H.; Sorokin, P. B.; Jin, C.; Ni, J.; Kvashnin, A. G.; Kvashnin, D. G.; Lou, J.; Yakobson, B. I.; Ajayan, P. M. Large Scale Growth and Characterization of Atomic Hexagonal Boron Nitride Layers. *Nano Lett.* **2010**, *10*, 3209–3215.

[175] Shi, Y.; Hamsen, C.; Jia, X.; Kim, K. K.; Reina, A.; Hofmann, M.; Hsu, a L.; Zhang, K.; Li, H.; Juang, Z. Y.; Dresselhaus, M. S.; Li, L. J.; Kong, J. Synthesis of Few-Layer Hexagonal Boron Nitride Thin Film by Chemical Vapor Deposition. *Nano Lett.* **2010**, *10*, 4134–4139.

[176] Boldrin, L.; Scarpa, F.; Chowdhury, R.; Adhikari, S. Effective Mechanical Properties of Hexagonal Boron Nitride Nanosheets. *Nanotechnology* **2011**, *22*, 505702.

[177] Li, C.; Bando, Y.; Zhi, C.; Huang, Y.; Golberg, D. Thickness-Dependent Bending Modulus of Hexagonal Boron Nitride Nanosheets. *Nanotechnology* **2009**, *20*,

385707.

[178] Kim, S. M.; Hsu, A.; Park, M. H.; Chae, S. H.; Yun, S. J.; Lee, J. S.; Cho, D.-H.; Fang, W.; Lee, C.; Palacios, T.; Dresselhaus, M.; Kim, K. K.; Lee, Y. H.; Kong, J. Synthesis of Large-Area Multilayer Hexagonal Boron Nitride for High Material Performance. *Nat. Commun.* **2015**, *6*, 8662.

[179] Li, L. H.; Cervenka, J.; Watanabe, K.; Taniguchi, T.; Chen, Y. Strong Oxidation Resistance of Atomically Thin Boron Nitride Nanosheets. *ACS Nano* **2014**, *8*, 1457–1462.

[180] Rand, M. J.; Roberts, J. F. Preparation and Properties of Thin Film Boron Nitride. *J. Electrochem. Soc.* **1968**, *115*, 423.

[181] Satti, A.; May, P.; Wang, Z.; Mcgovern, I.; Coleman, J. Oxygen Radical Functionalization of Boron Nitride Nanosheets. *J. Am. Chem. Soc.* **2012**, *134*, 18758–18771.

[182] Liu, Z.; Gong, Y.; Zhou, W.; Ma, L.; Yu, J.; Idrobo, J. C.; Jung, J.; MacDonald, A. H.; Vajtai, R.; Lou, J.; Ajayan, P. M. Ultrathin High-Temperature Oxidation-Resistant Coatings of Hexagonal Boron Nitride. *Nat. Commun.* **2013**, *4*, 2541.

[183] Lee, C.; Li, Q.; Kalb, W.; Liu, X. Z.; Berger, H.; Carpick, R. W.; Hone, J. Frictional Characteristics of Atomically Thin Sheets. *Science* **2010**, *328*, 76–80.

[184] Wang, H.; Taychatanapat, T.; Hsu, A.; Watanabe, K.; Taniguchi, T.; Jarillo-herrero, P.; Palacios, T. BN / Graphene / BN Transistors for RF Applications. *Nano* **2011**, *32*, 1209–1211.

[185] Britnell, L.; Gorbachev, R. V.; Jalil, R.; Belle, B. D.; Schedin, F.; Katsnelson, M. I.; Eaves, L.; Morozov, S. V.; Mayorov, A. S.; Peres, N. M. R.; Castro Neto, A. H.; Leist, J.;Geim, A. K.; Ponomarenko, L. A.; Novoselov, K. S. Electron Tunneling through Ultrathin Boron Nitride Crystalline Barriers. *Nano Lett.* **2012**, *12*, 1707–

1710.

[186] Petrone, N.; Chari, T.; Meric, I.; Wang, L.; Shepard, K. L.; Hone, J. Flexible Graphene Field-Effect Transistors Encapsulated in Hexagonal Boron Nitride. *ACS Nano* **2015**, *9*, 8953–8959.

[187] Lee, G. H.; Yu, Y. J.; Cui, X.; Petrone, N.; Lee, C. H.; Choi, M. S.; Lee, D. Y.; Lee, C.; Yoo, W. J.; Watanabe, K.; Taniguchi, T.; Nuckolls, C.; Kim, P.; Hone, J. Flexible and Transparent MoS2 Field-Effect Transistors on Hexagonal Boron Nitride-Graphene Heterostructures. *ACS Nano* **2013**, *7*, 7931–7936.

[188] Zhi, C.; Xu, Y.; Bando, Y.; Golberg, D. Highly Thermo-Conductive Fluid with Boron Nitride Nanofillers. *ACS Nano* **2011**, *5*, 6571–6577.

[189] Taha-Tijerina, J.; Narayanan, T. N.; Gao, G.; Rohde, M.; Tsentalovich, D. A.; Pasquali, M.; Ajayan, P. M. Electrically Insulating Thermal Nano-Oils Using 2D Fillers. *ACS Nano* **2012**, *6*, 1214–1220.

[190] Zhi, C.; Bando, Y.; Tang, C.; Kuwahara, H.; Golberg, D. Large-Scale Fabrication of Boron Nitride Nanosheets and Their Utilization in Polymeric Composites with Improved Thermal and Mechanical Properties. *Adv. Mater.* **2009**, *21*, 2889–2893.

[191] Song, W. L.; Wang, P.; Cao, L.; Anderson, A.; Meziani, M. J.; Farr, A. J.; Sun, Y. P. Polymer/boron Nitride Nanocomposite Materials for Superior Thermal Transport Performance. *Angew. Chemie - Int. Ed.* **2012**, *51*, 6498–6501.

[192] Tran, T. T.; Bray, K.; Ford, M. J.; Toth, M.; Aharonovich, I. Quantum Emission from Hexagonal Boron Nitride Monolayers. *Nat. Nanotechnol.* **2016**, *11*, 37–41.

[193] Aldalbahi, A.; Feng, P. Development of 2-D Boron Nitride Nanosheets UV Photoconductive Detectors. *IEEE Trans. Electron Devices* **2015**, *62*, 1885–1890.

[194] Wang, X.; Pakdel, A.; Zhi, C.; Watanabe, K.; Sekiguchi, T.; Golberg, D.; Bando, Y. High-Yield Boron Nitride Nanosheets from “Chemical Blowing”: Towards

Practical Applications in Polymer Composites. *J. Phys. Condens. Matter* **2012**, *24,* 314205.

[195] Wang, Y.; Shi, Z.; Yin, J. Boron Nitride Nanosheets: Large-Scale Exfoliation in Methanesulfonic Acid and Their Composites with Polybenzimidazole. *J. Mater. Chem.* **2011**, *21*, 11371.

[196] Balmain, W. H. Bemerktcngen Iiber Die Bildung von Verbin- Dungen Des Bors Icnd Silicizrrrrs Mit Stickstoff Und Gewissen Metallen. *J. Prakt. Chem* **1842**, *27*, 422–430.

[197] Lipp, A.; Schwetz, K. A.; Hunold, K. Hexagonal Boron Nitride : Fabrication , Properties and Applications. *J. Eur. Ceram. Soc.* **1989**, *5*, 3–9.

[198] Rudolph, S. Boron Nitride (BN). *Am. Ceram. Soc. Bull.* **2000,** 79, 50.

[199] Paciĺ, D.; Meyer, J. C.; Girit, Ç.; Zettl, A. The Two-Dimensional Phase of Boron Nitride: Few-Atomic-Layer Sheets and Suspended Membranes. *Appl. Phys. Lett.* **2008**, *92*, 133107.

[200] Gorbachev, R. V.; Riaz, I.; Nair, R. R.; Jalil, R.; Britnell, L.; Belle, B. D.; Hill, E. W.; Novoselov, K. S.; Watanabe, K.; Taniguchi, T.; Geim, A. K.; Blake, P. Hunting for Monolayer Boron Nitride: Optical and Raman Signatures. *Small* **2011**, *7*, 465–468.

[201] Wang, L.; Meric, I.; Huang, P. Y.; Gao, Q.; Gao, Y.; Tran, H.; Taniguchi, T.; Watanabe, K.; Campos, L. M.; Muller, D. A.; Guo, J.; Kim, P.; Hone, J.; Shepard, K. L.; Dean, C. R. One-dimensional Electrical Contact to a Two-Dimensional Material. *Science* **2013**, *342*, 614−617.

[202] Jin, C.; Lin, F.; Suenaga, K.; Iijima, S. Fabrication of a Freestanding Boron Nitride Single Layer and Its Defect Assignments. *Phys. Rev. Lett.* **2009**, *102*, 195505.

[203] Cunningham, G.; Lotya, M.; Cucinotta, C. S.; Sanvito, S.; Bergin, S. D.; Menzel,

R.; Shaffer, M. S. P.; Coleman, J. N. Solvent Exfoliation of Transition Metal Dichalcogenides: Dispersibility of Exfoliated Nanosheets Varies Only Weakly between Compounds. *ACS Nano* **2012**, *6*, 3468–3480.

[204] Han, W. Q.; Wu, L.; Zhu, Y.; Watanabe, K.; Taniguchi, T. Structure of Chemically Derived Mono- and Few-Atomic-Layer Boron Nitride Sheets. *Appl. Phys. Lett.* **2008**, *93*, 223103.

[205] Coleman, J. N.; Lotya, M.; Neill, A. O. '; Bergin, S. D.; King, P. J.; Khan, U.; Young, K.; Gaucher, A.; De, S.; Smith, R. J.; Shvets, I. V.; Arora, S. K.; Stanton, G.; Kim, H. Y.; Lee, K.; Kim, G. T.; Duesberg, G. S.; Hallam, T.; Boland, J. J.; Wang, J. J.; Donegan, J. F.; Grunlan, J. C.; Moriarty, G.; Shmeliov, A.; Nicholls, R. J.; Perkins, J. M.; Grieveson, E. M.; Theuwissen, K.; Mccomb, D. W.; Nellist, P. D.; Nicolosi, V. Two-Dimensional Nanosheets Produced by Liquid Exfoliation of Layered Materials. *Science* **2011**, *331*, 568–571.

[206] Zhou, K. G.; Mao, N. N.; Wang, H. X.; Peng, Y.; Zhang, H. L. A Mixed-Solvent Strategy for Efficient Exfoliation of Inorganic Graphene Analogues. *Angew. Chemie - Int. Ed.* **2011**, *50*, 10839–10842.

[207] Cao, L.; Emami, S.; Lafdi, K. Large-Scale Exfoliation of Hexagonal Boron Nitride Nanosheets in Liquid Phase. *Mater. Express* **2014**, *4*, 165–171.

[208] Takahashi, T.; Itoh, H.; Takeuchi, A. Chemical Vapor Deposition of Hexagonal Boron Nitride Thick Film on Iron. *J. Cryst. Growth* **1979**, *47*, 245–250.

[209] Sano, M.; Aoki, M. Chemical Vapour Deposition of Thin Films of BN onto Fused Silica and Sapphire. *Thin Solid Films* **1981**, *83*, 247–251.

[210] Arya, S. P. S; D'Amico, A. Preparation, properties and applications of boron nitride thin films. *Thin Solid Films* **1988**, *157*, 267–282.

[211] Phani, A. R. Thin Films of Boron Nitride Grown by CVD. *Bull. Mater. Sci.* **1994**,

17, 219–224.

[212] Nagashima, A.; Tejima, N.; Gamou, Y.; Kawai, T.; Oshirna, C. Electronic Structure of Monolayer Hexagonal Boron Nitride Physisorbed on Metal Surfaces. *Phys. Rev. Lett.* **1995**, *75*, 3918–3921.

[213] Kim, K. K.; Hsu, A.; Jia, X.; Kim, S. M.; Shi, Y.; Hofmann, M.; Nezich, D.; Rodriguez-Nieva, J. F.; Dresselhaus, M.; Palacios, T.; Kong, J. Synthesis of Monolayer Hexagonal Boron Nitride on Cu Foil Using Chemical Vapor Deposition. Nano Lett. 2011, 12, 161−166.

[214] Stehle, Y.; Meyer, H. M.; Unocic, R. R.; Kidder, M.; Polizos, G.; Datskos, P. G.; Jackson, R.; Smirnov, S. N.; Vlassiouk, I. V. Synthesis of Hexagonal Boron Nitride Monolayer: Control of Nucleation and Crystal Morphology. *Chem. Mater.* **2015**, *27*, 8041–8047.

[215] Tay, R. Y.; Griep, M. H.; Mallick, G.; Tsang, S. H.; Singh, R. S.; Tumlin, T.; Teo, E. H. T.; Karna, S. P. Growth of Large Single-Crystalline Two-Dimensional Boron Nitride Hexagons on Electropolished Copper. *Nano Lett.* **2014**, *14*, 839–846.

[216] Song, X.; Gao, J.; Nie, Y.; Gao, T.; Sun, J.; Ma, D.; Li, Q.; Chen, Y.; Jin, C.; Bachmatiuk, A.; Rümmeli, M. H.; Ding, F.; Zhang, Y.; Liu, Z. Chemical Vapor Deposition Growth of Large-Scale Hexagonal Boron Nitride with Controllable Orientation. *Nano Res.* **2015**, *8*, 3164–3176.

[217] Tay, R. Y.; Park, H. J.; Ryu, G. H.; Tan, D.; Tsang, S. H.; Li, H.; Liu, W.; Teo, E. H. T.; Lee, Z.; Lifshitz, Y.; Ruoff, R. S. Synthesis of Aligned Symmetrical Multifaceted Monolayer Hexagonal Boron Nitride Single Crystals on Resolidified Copper. *Nanoscale* **2016**, *8*, 2434–2444.

[218] Wang, L.; Wu, B.; Jiang, L.; Chen, J.; Li, Y.; Guo, W.; Hu, P.; Liu, Y. Growth and Etching of Monolayer Hexagonal Boron Nitride. *Adv. Mater.* **2015**, *27*, 4858–4864.

[219] Yin, J.; Yu, J.; Li, X.; Li, J.; Zhou, J.; Zhang, Z.; Guo, W. Large Single-Crystal Hexagonal Boron Nitride Monolayer Domains with Controlled Morphology and Straight Merging Boundaries. *Small* **2015**, *11*, 4497–4502.

[220] Ismach, A.; Chou, H.; Ferrer, D. A.; Wu, Y.; McDonnell, S.; Floresca, H. C.; Covacevich, A.; Pope, C.; Piner, R.; Kim, M. J.; Wallace, R. M.; Colombo, L.; Ruoff, R. S. Toward the Controlled Synthesis of Hexagonal Boron Nitride Films. *ACS Nano* **2012**, *6*, 6378–2385.

[221] Cho, H.; Park, S.; Won, D.-I.; Kang, S. O.; Pyo, S.-S.; Kim, D.-I.; Kim, S. M.; Kim, H. C.; Kim, M. J. Growth Kinetics of White Graphene (h-BN) on a Planarised Ni Foil Surface. *Sci. Rep.* **2015**, *5*, 11985.

[222] Gao, Y.; Ren, W.; Ma, T.; Liu, Z.; Zhang, Y.; Liu, W. Bin; Ma, L. P.; Ma, X.; Cheng, H. M. Repeated and Controlled Growth of Monolayer, Bilayer and Few-Layer Hexagonal Boron Nitride on Pt Foils. *ACS Nano* **2013**, *7*, 5199–5206.

[223] Kim, G.; Jang, A. R.; Jeong, H. Y.; Lee, Z.; Kang, D. J.; Shin, H. S. Growth of High-Crystalline, Single-Layer Hexagonal Boron Nitride on Recyclable Platinum Foil. *Nano Lett.* **2013**, *13*, 1834–1839.

[224] Zhang, Y.; Weng, X.; Li, H.; Li, H.; Wei, M.; Xiao, J.; Liu, Z.; Chen, M.; Fu, Q.; Bao, X. Hexagonal Boron Nitride Cover on Pt(111): A New Route to Tune Molecule-Metal Interaction and Metal-Catalyzed Reactions. *Nano Lett.* **2015**, *15*, 3616–3623.

[225] Caneva, S.; Weatherup, R. S.; Bayer, B. C.; Blume, R.; Cabrero-Vilatela, A.; Braeuninger-Weimer, P.; Martin, M. B.; Wang, R.; Baehtz, C.; Schloegl, R.; Meyer, J. C.; Hofmann, S. Controlling Catalyst Bulk Reservoir Effects for Monolayer Hexagonal Boron Nitride CVD. *Nano Lett.* **2016**, *16*, 1250–1261.

[226] Vinogradov, N. A.; Zakharov, A. A.; Ng, M. L.; Mikkelsen, A.; Lundgren, E.;

Mårtensson, N.; Preobrajenski, A. B. One-Dimensional Corrugation of the h-BN Monolayer on Fe(110). *Langmuir* **2012**, *28*, 1775–1781.

[227] Sutter, P.; Lahiri, J.; Albrecht, P.; Sutter, E. Chemical Vapor Deposition and Etching of High-Quality Monolayer Hexagonal Boron Nitride Films. *ACS Nano* **2011**, *5*, 7303–7309.

[228] Lu, G.; Wu, T.; Yuan, Q.; Wang, H.; Wang, H.; Ding, F.; Xie, X.; Jiang, M. Synthesis of Large Single-Crystal Hexagonal Boron Nitride Grains on Cu-Ni Alloy. *Nat. Commun.* **2015**, *6*, 6160.

[229] Caneva, S.; Weatherup, R. S.; Bayer, B. C.; Brennan, B.; Spencer, S. J.; Mingard, K.; Cabrero-Vilatela, A.; Baehtz, C.; Pollard, A. J.; Hofmann, S. Nucleation Control for Large, Single Crystalline Domains of Monolayer Hexagonal Boron Nitride via Si-Doped Fe Catalysts. *Nano Lett.* **2015**, *15*, 1867–1875.

[230] Chatterjee, S.; Luo, Z.; Acerce, M.; Yates, D. M.; Johnson, A. T. C.; Sneddon, L. G. Chemical Vapor Deposition of Boron Nitride Nanosheets on Metallic Substrates via Decaborane/Ammonia Reactions. *Chem. Mater.* **2011**, *23*, 4414–4416.

[231] Lee, Y.-H.; Liu, K.-K.; Lu, A.-Y.; Wu, C.-Y.; Lin, C.-T.; Zhang, W.; Su, C.-Y.; Hsu, C.-L.; Lin, T.-W.; Wei, K.-H.; Shi, Y.; Li, L.-J. Growth Selectivity of Hexagonal-Boron Nitride Layers on Ni with Various Crystal Orientations. *RSC Adv.* **2012**, *2*, 111–115.

[232] Park, J. H.; Park, J. C.; Yun, S. J.; Kim, H.; Luong, D. H.; Kim, S. M.; Choi, S. H.; Yang, W.; Kong, J.; Kim, K. K.; Lee, Y. H. Large-Area Monolayer Hexagonal Boron Nitride on Pt Foil. *ACS Nano* **2014**, *8*, 8520–8528.

[233] Spear, K. E., Thermochemical Modeling of Steady-State CVD Process. *Proc. 9th. Int. Conf. on CVD, Electrochem. Soc., Pennington, NJ 08534*, **1984**, 81–97.

[234] Pearson, H. Handbook of Chemical Vapor Deposition. Noyes, *Park Ridge, NJ*

Noyes Publications, **1992**.

[235] Preobrajenski, A. B.; Vinogradov, A. S.; Mårtensson, N. Monolayer of h-BN Chemisorbed on Cu(111) and Ni(111): The Role of the Transition Metal 3d States. *Surf. Sci.* **2005**, *582*, 21–30.

[236] Laskowski, R.; Blaha, P.; Schwarz, K. Bonding of Hexagonal BN to Transition Metal Surfaces: An Ab Initio Density-Functional Theory Study. *Phys. Rev. B.* **2008**, *78*, 045409.

[237] Bokdam, M.; Brocks, G.; Katsnelson, M. I.; Kelly, P. J. Schottky Barriers at Hexagonal Boron Nitride/metal Interfaces: A First-Principles Study. *Phys. Rev.* **2014**, *90*, 085415.

[238] Mattevi, C.; Kim, H.; Chhowalla, M. A Review of Chemical Vapour Deposition of Graphene on Copper. *J. Mater. Chem.* **2011**, *21*, 3324–3334.

[239] López, G. A.; Mittemeijer, E. J. The Solubility of C in Solid Cu. *Scr. Mater.* **2004**, *51*, 1–5.

[240] Muñoz, R.; Gómez-Aleixandre, C. Review of CVD Synthesis of Graphene. *Chem. Vap. Depos.* **2013,** *19*, 297–322.

[241] Kidambi, P. R.; Blume, R.; Kling, J.; Wagner, J. B.; Baehtz, C.; Weatherup, R. S.; Schloegl, R.; Bayer, B. C.; Hofmann, S. In Situ Observations during Chemical Vapor Deposition of Hexagonal Boron Nitride on Polycrystalline Copper. *Chem. Mater.* **2014**, *26*, 6380–6392.

[242] Luo Y. R. Comprehensive handbook of chemical bond energies. *CRC Press, Boca Raton,* **2007,** 1–1487.

[243] Suk, J. W.; Kitt, A.; Magnuson, C. W.; Hao, Y.; Ahmed, S.; An, J.; Swan, A. K.; Goldberg, B. B.; Ruoff, R. S. Transfer of CVD-Grown Monolayer Graphene onto Arbitrary Substrates. *ACS Nano* **2011**, *5*, 6916–6924.

[244] Liang, X.; Sperling, B. A.; Calizo, I.; Cheng, G.; Hacker, C. A.; Zhang, Q.; Obeng, Y.; Yan, K.; Peng, H.; Li, Q.; Zhu, X.; Yuan, Hui H.; Walker, A. R.; Liu, Z.; Peng, L. M.; Richter, C. A. Toward Clean and Crackless Transfer of Graphene. *ACS Nano* **2011**, *5*, 9144–9153.

[245] Lin, Y. C.; Jin, C.; Lee, J. C.; Jen, S. F.; Suenaga, K.; Chiu, P. W. Clean Transfer of Graphene for Isolation and Suspension. *ACS Nano* **2011**, *5*, 2362–2368.

[246] Lin, Y. C.; Lu, C. C.; Yeh, C. H.; Jin, C.; Suenaga, K.; Chiu, P. W. Graphene Annealing: How Clean Can It Be? *Nano Lett.* **2012**, *12*, 414–419.

[247] Kim, K. K.; Hsu, A.; Jia, X.; Kim, S. M.; Shi, Y.; Dresselhaus, M.; Kong, J. Synthesis and Characterization of Hexagonal Boron Nitride Film as a Dielectric Layer for Graphene Devices. *ACS Nano* **2012**, *6*, 8583–8590.

[248] Singh, R. S.; Tay, R. Y.; Chow, W. L.; Tsang, S. H.; Mallick, G.; Tong, E. H. Band Gap Effects of Hexagonal Boron Nitride Using Oxygen Plasma. *Appl. Phys. Lett.* **2014**, *104*, 163101.

[249] Wang, M.; Jang, S. K.; Jang, W. J.; Kim, M.; Park, S. Y.; Kim, S. W.; Kahng, S. J.; Choi, J. Y.; Ruoff, R. S.; Song, Y. J.; Lee, S. A Platform for Large-Scale Graphene Electronics - CVD Growth of Single-Layer Graphene on CVD-Grown Hexagonal Boron Nitride. *Adv. Mater.* **2013**, *25*, 2746–2752.

[250] Cherian, C. T.; Giustiniano, F.; Martin-Fernandez, I.; Andersen, H.; Balakrishnan, J.; Özyilmaz, B. Bubble-Free Electrochemical Delamination of CVD Graphene Films. *Small* **2015**, *11*, 189–194.

[251] Wang, Y.; Zheng, Y.; Xu, X.; Dubuisson, E.; Bao, Q.; Lu, J.; Loh, K. P. Electrochemical Delamination of CVD-Grown Graphene Film: Toward the Recyclable Use of Copper Catalyst. *ACS Nano* **2011**, *5*, 9927–9933.

[252] Regan, W.; Alem, N.; Alemán, B.; Geng, B.; Girit, Ç.; Maserati, L.; Wang, F.;

Crommie, M.; Zettl, A. Direct Transfer of Layer-Area Graphene. *Appl. Phys. Lett.* **2010**, *96*, 113102.

[253] Gibb, A.; Alem, N.; Zettl, A. Low Pressure Chemical Vapor Deposition Synthesis of Hexagonal Boron Nitride on Polycrystalline Metal Foils. *Phys. Status Solidi* **2013**, *250*, 2727–2731.

[254] Blake, P.; Hill, E. W.; Castro Neto, A. H.; Novoselov, K. S.; Jiang, D.; Yang, R.; Booth, T. J.; Geim, A. K. Making Graphene Visible. *Appl. Phys. Lett.* **2007**, *91*, 063124.

[255] Duong, D. L.; Han, G. H.; Lee, S. M.; Gunes, F.; Kim, E. S.; Kim, S. T.; Kim, H.; Ta, Q. H.; So, K. P.; Yoon, S. J.; Chae, S. J.; Jo, Y. W.; Park, M. H.; Chae, S. H.; Lim, S. C.; Choi, J. Y.; Lee, Y. H. Probing Graphene Grain Boundaries with Optical Microscopy. *Nature* **2012**, *490*, 235–239.

[256] Jia, C.; Jiang, J.; Gan, L.; Guo, X. Direct Optical Characterization of Graphene Growth and Domains on Growth Substrates. *Sci. Rep.* **2012**, *2*, 707.

[257] Lee, J.-Y.; Lee, J.-H.; Kim, M. J.; Dash, J. K.; Lee, C.-H.; Joshi, R.; Lee, S.; Hone, J.; Soon, A.; Lee, G.-H. Direct Observation of Grain Boundaries in Chemical Vapor Deposited Graphene. *Carbon* **2017**, *115*, 147–153.

[258] Ferrari, A. C.; Meyer, J. C.; Scardaci, V.; Casiraghi, C.; Lazzeri, M.; Mauri, F.; Piscanec, S.; Jiang, D.; Novoselov, K. S.; Roth, S.; Geim, A. K. Raman Spectrum of Graphene and Graphene Layers. *Phys. Rev. Lett.* **2006**, *97, 187401*.

[259] Ferrari, A. C. Raman Spectroscopy of Graphene and Graphite: Disorder, Electron-Phonon Coupling, Doping and Nonadiabatic Effects. *Solid State Commun.* **2007**, *143*, 47–57.

[260] Park, J. S.; Reina, A.; Saito, R.; Kong, J.; Dresselhaus, G.; Dresselhaus, M. S. G′band Raman Spectra of Single, Double and Triple Layer Graphene. *Carbon* **2009**,

47, 1303–1310.

[261] Reich, S.; Ferrari, A. C.; Arenal, R.; Loiseau, A.; Bello, I.; Robertson, J. Resonant Raman Scattering in Cubic and Hexagonal Boron Nitride. *Phys. Rev. B* **2005**, *71*, 205201.

[262] Guo, N.; Wei, J.; Fan, L.; Jia, Y.; Liang, D.; Zhu, H.; Wang, K.; Wu, D. Controllable Growth of Triangular Hexagonal Boron Nitride Domains on Copper Foils by an Improved Low-Pressure Chemical Vapor Deposition Method. *Nanotechnology* **2012**, *23*, 415605.

[263] Murdock, A. T.; Koos, A.; Britton, T. Ben; Houben, L.; Batten, T.; Zhang, T.; Wilkinson, A. J.; Dunin-Borkowski, R. E.; Lekka, C. E.; Grobert, N. Controlling the Orientation, Edge Geometry, and Thickness of Chemical Vapor Deposition Graphene. *ACS Nano* **2013**, *7*, 1351–1359.

[264] Li, X.; Hao, X.; Zhao, M.; Wu, Y.; Yang, J.; Tian, Y.; Qian, G. Exfoliation of Hexagonal Boron Nitride by Molten Hydroxides. *Adv. Mater.* **2013**, *25*, 2200–2204.

[265] Cui, Z.; Oyer, A. J.; Glover, A. J.; Schniepp, H. C.; Adamson, D. H. Large Scale Thermal Exfoliation and Functionalization of Boron Nitride. *Small* **2014**, *10*, 2352–2355.

[266] Yan, Z.; Lin, J.; Peng, Z.; Sun, Z.; Zhu, Y.; Li, L.; Xiang, C.; Loı, E.; Kittrell, C.; Tour, J. M. Toward the Synthesis of Wafer-Scale Single-Crystal Graphene on Copper Foils. *ACS Nano* **2012**, *6*, 9110–9117.

[267] Wu, W.; Jauregui, L. A.; Su, Z.; Liu, Z.; Bao, J.; Chen, Y. P.; Yu, Q. Growth of Single Crystal Graphene Arrays by Locally Controlling Nucleation on Polycrystalline Cu Using Chemical Vapor Deposition. *Adv. Mater.* **2011**, *23*, 4898–4903.

[268] Luo, B.; Chen, B.; Meng, L.; Geng, D.; Liu, H.; Xu, J.; Zhang, Z.; Zhang, H.; Peng,

L.; He, L.; Hu, W.; Liu, Y.; Yu, G. Layer-Stacking Growth and Electrical Transport of Hierarchical Graphene Architectures. *Adv. Mater.* **2014**, *26*, 3218–3224.

[269] Liu, W.; Kraemer, S.; Sarkar, D.; Li, H.; Ajayan, P. M.; Banerjee, K. Controllable and Rapid Synthesis of High-Quality and Large-Area Bernal Stacked Bilayer Graphene Using Chemical Vapor Deposition. *Chem. Mater.* **2014**, *26*, 907–915.

[270] Wofford, J. M.; Nie, S.; McCarty, K. F.; Bartelt, N. C.; Dubon, O. D. Graphene Islands on Cu Foils: The Interplay between Shape, Orientation, and Defects. *Nano Lett.* **2010**, *10*, 4890–4896.

[271] Bhaviripudi, S.; Jia, X.; Dresselhaus, M. S.; Kong, J. Role of Kinetic Factors in Chemical Vapor Deposition Synthesis of Uniform Large Area Graphene Using Copper Catalyst. *Nano Lett.* **2010**, *10*, 4128–4133.

[272] Jacobberger, R. M.; Levesque, P. L.; Xu, F.; Wu, M. Y.; Choubak, S.; Desjardins, P.; Martel, R.; Arnold, M. S. Tailoring the Growth Rate and Surface Facet for Synthesis of High-Quality Continuous Graphene Films from CH_4 at 750 ^{o}C via Chemical Vapor Deposition. *J. Phys. Chem. C* **2015**, *119*, 11516–11523.

[273] Qi, M.; Ren, Z.; Jiao, Y.; Zhou, Y.; Xu, X.; Li, W.; Li, J.; Zheng, X.; Bai, J. Hydrogen Kinetics on Scalable Graphene Growth by Atmospheric Pressure Chemical Vapor Deposition with Acetylene. *J. Phys. Chem. C* **2013**, *117*, 14348–14353.

[274] Frank, O.; Vejpravova, J.; Holy, V.; Kavan, L.; Kalbac, M. Interaction between Graphene and Copper Substrate: The Role of Lattice Orientation. *Carbon* **2014**, *68*, 440–451.

[275] Wood, J. D.; Schmucker, S. W.; Lyons, A. S.; Pop, E.; Lyding, J. W. Effects of Polycrystalline Cu Substrate on Graphene Growth by Chemical Vapor Deposition. *Nano Lett* **2011**, *11*, 4547–4554.

[276] Kim, S. J.; Kim, D. W.; Jung, H.-T. Key Growth Parameters Affecting the Domain Structure of Chemical Vapor Deposition (CVD)-Grown Graphene on Nickel. *RSC Adv.* **2013**, *3*, 22909–22913.

[277] Jin, Y.; Hu, B.; Wei, Z.; Luo, Z.; Wei, D.; Xi, Y.; Zhang, Y.; Liu, Y. Roles of H_2 in Annealing and Growth Times of Graphene CVD Synthesis over Copper Foil. *J. Mater. Chem. A* **2014**, *2*, 16208–16216.

[278] Ci, L.; Xu, Z. P.; Wang, L. L.; Gao, W.; Ding, F.; Kelly, K. F.; Yakobson, B. I.; Ajayan, P. M. Controlled Nanocutting of Graphene. *Nano Res.* **2008**, *1*, 116–122.

[279] Campos, L. C.; Manfrinato, V. R.; Sanchez-Yamagishi, J. D.; Kong, J.; Jarillo-Herrero, P. Anisotropic Etching and Nanoribbon Formation in Single-Layer Graphene. *Nano Lett.* **2009**, *9*, 2600–2604.

[280] Geng, D.; Wu, B.; Guo, Y.; Luo, B.; Xue, Y.; Chen, J.; Yu, G.; Liu, Y. Fractal Etching of Graphene. *J. Am. Chem. Soc.* **2013**, *135*, 6431−6434.

[281] Thangaraja, A.; Shinde, S. M.; Kalita, G.; Papon, R.; Sharma, S.; Vishwakarma, R.; Sharma, K. P.; Tanemura, M. Structure Dependent Hydrogen Induced Etching Features of Graphene Crystals. *Appl. Phys. Lett.* **2015**, *106*.

[282] Yang, B. R.; Zhang, L.; Wang, Y.; Shi, Z.; Shi, D.; Gao, H.; Wang, E.; Zhang, G. An Anisotropic Etching Effect in the Graphene Basal Plane. *Adv. Mater.* **2010**, *22*, 4014–4019.

[283] Ago, H.; Kayo, Y.; Solís-Fernández, P.; Yoshida, K.; Tsuji, M. Synthesis of High-Density Arrays of Graphene Nanoribbons by Anisotropic Metal-Assisted Etching. *Carbon* **2014**, *78*, 339–346.

[284] Nemes-Incze, P.; Magda, G.; Kamarás, K.; Biró, L. P. Crystallographically Selective Nanopatterning of Graphene on SiO_2. *Nano Res.* **2010**, *3*, 110–116.

[285] Datta, S. S.; Strachan, D. R.; Khamis, S. M.; Johnson, A. T. C. Crystallographic

Etching of Few-Layer Graphene. *Nano Lett.* **2008**, *8*, 1912–1915.

[286] Luo, D.; Yang, F.; Wang, X.; Sun, H.; Gao, D.; Li, R.; Yang, J.; Li, Y. Anisotropic Etching of Graphite Flakes with Water Vapor to Produce Armchair-Edged Graphene. *Small* **2014**, *10*, 2809–2814.

[287] Zhang, Y.; Li, Z.; Kim, P.; Zhang, L.; Zhou, C. Anisotropic Hydrogen Etching of Chemical Vapor Deposited Graphene. *ACS Nano* **2012**, *6*, 126–132.

[288] Choubak, S.; Biron, M.; Levesque, P. L.; Martel, R.; Desjardins, P. No Graphene Etching in Purified Hydrogen. *J. Phys. Chem. Lett.* **2013**, *4*, 1100–1103.

[289] Wang, B.; Zhang, Y.; Zhang, H.; Chen, Z.; Xie, X.; Sui, Y.; Li, X.; Yu, G.; Hu, L.; Jin, Z.; Liu, X. Wrinkle-Dependent Hydrogen Etching of Chemical Vapor Deposition-Grown Graphene Domains. *Carbon* **2014**, *70*, 75–80.

[290] Zhang, H.; Zhang, Y.; Zhang, Y.; Chen, Z.; Sui, Y.; Ge, X.; Yu, G.; Jin, Z.; Liu, X. Edge Morphology Evolution of Graphene Domains during Chemical Vapor Deposition Cooling Revealed through Hydrogen Etching. *Nanoscale* **2016**, *8*, 4145–4150.

[291] Jung, D. H.; Kang, C.; Nam, J. E.; Jeong, H.; Lee, J. S. Surface Diffusion Directed Growth of Anisotropic Graphene Domains on Different Copper Lattices. *Sci. Rep.* **2016**, *6*, 21136.

[292] Zhang, H.; Zhang, Y.; Wang, B.; Chen, Z.; Zhang, Y.; Sui, Y.; Yu, G.; Jin, Z.; Liu, X. Stripe Distributions of Graphene-Coated Cu Foils and Their Effects on the Reduction of Graphene Wrinkles. *RSC Adv.* **2015**, *5*, 96587–96592.

[293] Zhao, P.; Kumamoto, A.; Kim, S.; Chen, X.; Hou, B.; Chiashi, S.; Einarsson, E.; Ikuhara, Y.; Maruyama, S. Self-Limiting Chemical Vapor Deposition Growth of Monolayer Graphene from Ethanol. *J. Phys. Chem. C* **2013**, *117*, 10755−10763.

[294] Rasmussen, P. B.; Holmblad, P. M.; Christoffersen, H.; Taylor, P. A.; Chorkendorff,

I. Dissociative Adsorption of Hydrogen on Cu(100) at Low Temperatures. *Surf. Sci.* **1993**, *287–288*, 79–83.

[295] Mudiyanselage, K.; Yang, Y.; Hoffmann, F. M.; Furlong, O. J.; Hrbek, J.; White, M. G.; Liu, P.; Stacchiola, D. J. Adsorption of Hydrogen on the Surface and Sub-Surface of Cu(111). *J. Chem. Phys.* **2013**, *139*, 044712.

[296] Luo, M. F.; Hu, G. R.; Lee, M. H. Surface Structures of Atomic Hydrogen Adsorbed on Cu(111) Surface Studied by Density-Functional-Theory Calculations. *Surf. Sci.* **2007**, *601*, 1461–1466.

[297] Wu, T.; Zhang, X.; Yuan, Q.; Xue, J.; Lu, G.; Liu, Z.; Wang, H.; Wang, H.; Ding, F.; Yu, Q.; Xie, X.; Jiang, M. Fast Growth of Inch-Sized Single-Crystalline Graphene from a Controlled Single Nucleus on Cu–Ni Alloys. *Nat. Mater.* **2015**, *15*, 43–47.

[298] Wu, T.; Ding, G.; Shen, H.; Wang, H.; Sun, L.; Jiang, D.; Xie, X.; Jiang, M. Triggering the Continuous Growth of Graphene toward Millimeter-Sized Grains. *Adv. Funct. Mater.* **2013**, *23*, 198–203.

[299] Hu, B.; Ago, H.; Ito, Y.; Kawahara, K.; Tsuji, M.; Magome, E.; Sumitani, K.; Mizuta, N.; Ikeda, K. I.; Mizuno, S. Epitaxial Growth of Large-Area Single-Layer Graphene over Cu(111)/sapphire by Atmospheric Pressure CVD. *Carbon* **2012**, *50*, 57–65.

[300] Tan, L.; Zeng, M.; Zhang, T.; Fu, L. Design of Catalytic Substrates for Uniform Graphene Films: From Solid-Metal to Liquid-Metal. *Nanoscale* **2015**, *7*, 9105–9121.

[301] Li, Z.; Wu, P.; Wang, C.; Fan, X.; Zhang, W.; Zhai, X.; Zeng, C.; Li, Z.; Yang, J.; Hou, J. Low-Temperature Growth of Graphene by Chemical Vapor Deposition Using Solid and Liquid Carbon Sources. *ACS Nano* **2011**, *5*, 3385–3390.

[302] Sun, H.; Rosenthal, C.; Schmidt, L. D. Oxidative Pyrolysis of Polystyrene into

Styrene Monomers in an Autothermal Fixed-Bed Catalytic Reactor. *ChemSusChem* **2012**, *5*, 1883–1887.

[303] Sarker, M.; Rashid, M. M.; Rahman, M. S.; Molla, M. Polystyrene (PS) Waste Plastic Conversion into Aviation /kerosene Category of Fuel by Using Fractional Column Distillation Process. *Int. J. energy Environ.* **2012**, *3*, 871–880.

[304] Somekh, M.; Shawat, E.; Nessim, G. D. Fully Reproducible, Low-Temperature Synthesis of High-Quality, Few-Layer Graphene on Nickel via Preheating of Gas Precursors Using Atmospheric Pressure Chemical Vapor Deposition. *J. Mater. Chem. A* **2014**, *2*, 19750–19758.

[305] Gan, L.; Luo, Z. Turning off Hydrogen to Realize Seeded Growth of Subcentimeter Single-Crystal Graphene Grains on Copper. *ACS Nano* **2013**, *7*, 9480–9488.

[306] Robinson, Z. R.; Tyagi, P.; Murray, T. M.; Ventrice Jr, C. A.; Chen, S.; Munson, A.; Magnuson, C. W.; Ruoff, R. S. Substrate Grain Size and Orientation of Cu and Cu–Ni Foils Used for the Growth of Graphene Films. *J. Vac. Sci. Technol. S* **2012**, *30*, 011401.

[307] Zhang, Y.; Zhang, L.; Kim, P.; Ge, M.; Li, Z.; Zhou, C. Vapor Trapping Growth of Single-Crystalline Graphene Flowers: Synthesis, Morphology, and Electronic Properties. *Nano Lett.* **2012**, *12*, 2810–2816.

[308] Yan, Z.; Liu, Y.; Ju, L.; Peng, Z.; Lin, J.; Wang, G.; Zhou, H.; Xiang, C.; Samuel, E. L. G.; Kittrell, C.; *et al.* Large Hexagonal Bi- and Trilayer Graphene Single Crystals with Varied Interlayer Rotations. *Angew. Chemie - Int. Ed.* **2014**, *53*, 1565–1569.

[309] Shi, Y. G.; Wang, D.; Zhang, J. C.; Zhang, P.; Shi, X. F.; Hao, Y. Fabrication of Single-Crystal Few-Layer Graphene Domains on Copper by Modified Low-Pressure Chemical Vapor Deposition. *CrystEngComm* **2014**, *16*, 7558.

[310] Zhan, Y.; Liu, Z.; Najmaei, S.; Ajayan, P. M.; Lou, J. Large-Area Vapor-Phase

Growth and Characterization of MoS_2 Atomic Layers on a SiO_2 Substrate. *Small* **2012**, *8*, 966–971.

[311] Lee, Y.-H.; Zhang, X.-Q.; Zhang, W.; Chang, M.-T.; Lin, C.-T.; Chang, K.-D.; Yu, Y.-C.; Wang, J. T.-W.; Chang, C.-S.; Li, L.-J.; *et al.* Synthesis of Large-Area MoS_2 Atomic Layers with Chemical Vapor Deposition. *Adv. Mater.* **2012**, *24*, 2320–2325.

[312] Geng, D.; Wang, H.; Yu, G. Graphene Single Crystals: Size and Morphology Engineering. *Adv. Mater.* **2015**, *27*, 2821–2837.

[313] Chen, X.; Liu, S.; Liu, L.; Liu, X.; Liu, X.; Wang, L. Growth of Triangle-Shape Graphene on Cu(111) Surface. *Appl. Phys. Lett.* **2012**, *100*, 100–103.

[314] Kumar, K.; Yang, E. H. On the Growth Mode of Two-Lobed Curvilinear Graphene Domains at Atmospheric Pressure. *Sci. Rep.* **2013**, *3*, 1–7.

[315] Barone, V.; Peralta, J. E. Magnetic Boron Nitride Nanoribbons with Tunable Electronic Properties. *Nano Lett.* **2008**, *8*, 2210–2214.

[316] Mukherjee, R.; Bhowmick, S. Edge Stabilities of Hexagonal Boron Nitride Nanoribbons: A First-Principles Study. *J. Chem. Theory Comput.* **2011**, *7*, 720–724.

[317] Sharma S, Kalita G, Vishwakarma R, Zulkifli Z, T. M. Opening of Triangular Hole in Triangular-Shaped Chemical Vapor Deposited Hexagonal Boron Nitride Crystal. *Sci. Rep.* **2015**, *5*, 10426.

[318] Frueh, S.; Kellett, R.; Mallery, C.; Molter, T.; Willis, W. S.; King'Ondu, C.; Suib, S. L. Pyrolytic Decomposition of Ammonia Borane to Boron Nitride. *Inorg. Chem.* **2011**, *50*, 783–792.

[319] Vlassiouk, I.; Regmi, M.; Fulvio, P.; Dai, S.; Datskos, P.; Eres, G.; Smirnov, S. Role of Hydrogen in Chemical Vapor Deposition Growth of Large Single-Crystal Graphene. *ACS Nano* **2011**, *5*, 6069–6076.

[320] Liu, Y.; Bhowmick, S.; Yakobson, B. I. BN White Graphene With "colorful" edges:

The Energies and Morphology. *Nano Lett.* **2011**, *11*, 3113–3116.

[321] Sharma, K. P., Mahyavanshi, R. D., Kalita, G. & Tanemura, M. Influence of copper foil polycrystalline structure on graphene anisotropic etching. Appl. Surf. Sci. 393, 428–433 (2017).

[322] Witten, T. A.; Sander, I. M. Diffusion-Limited Aggregation, a Kinetic Critical Phenomenon. *Phys. Rev. Lett.* **1981**, *47*, 1400–1403.

[323] Wang, L.; Wu, B.; Chen, J.; Liu, H.; Hu, P.; Liu, Y. Monolayer Hexagonal Boron Nitride Films with Large Domain Size and Clean Interface for Enhancing the Mobility of Graphene-Based Field-Effect Transistors. *Adv. Mater.* **2014**, *26*, 1559–1564.

[324] Pease, R. S. Crystal Structure of Boron Nitride. *Nature* **1950**, *165*, 722–723.

[325] Zhang, Z.; Liu, Y.; Yang, Y.; Yakobson, B. I. Growth Mechanism and Morphology of Hexagonal Boron Nitride. *Nano Lett* **2016**, *16*, 1398–1403.

[326] Sun, L.; Lin, L.; Zhang, J.; Wang, H.; Peng, H.; Liu, Z. Visualizing Fast Growth of Large Single-Crystalline Graphene by Tunable Isotopic Carbon Source. *Nano Res.* **2016**, *1*, 1–9.

[327] L. Meng, Y. Su, D. C. Geng, G. Yu, Y. Q. Liu, R. F. Dou, J. C.Nie and L. He, Appl. Phys. Lett., 2013, 103, 251610.

[328] S. J. Yu, M. W. Kang, H. C. Chang, K. M. Chen and Y. C. Yu,J. Am. Chem. Soc., 2005, 127, 17604–17605.

[329] Ç. Ö. Girit, J. C. Meyer, R. Erni, M. D. Rossell, C. Kisielowski, L. Yang, C. H. Park, M. Crommie, M. L. Cohen and S. G. Louie, Science, 2009, 323, 1705–1708.